CENTRAL UNIVERSITY OF TECHNOLOGY, FREE STATE

Investigation of in-situ alloying grade 23 Titanium with Copper by Selective Laser Melting Process for biomedical applications

---

Eric Brian Newby

210013222
Dissertation Submitted
in fulfilment of the
requirements for the degree
MASTER of ENGINEERING: MECHANICAL ENGINEERING

Supervisor: Prof. Ihar Yadroitsau, Ph.D.
Co-supervisors: Dr. Ina Yadroitsava, Ph.D.
Mr. Allan Kinnear, M.Eng.

Bloemfontein
2018

Declaration of independent work

I, Eric Brian Newby, identity number and student number , do hereby declare that this research project submitted to the Central University of Technology, Free State (CUT, FS) for the Master of Engineering in Mechanical Engineering, is my own independent work; and complies with the code of Academic integrity, as well as other relevant policies, procedures, rules and regulations of the Central University of Technology, Free State; and has not been submitted previously to any institution by myself or any other person in fulfilment of the requirements for the attainment of any qualification.

SIGNATURE OF STUDENT.................................DATE....................................

Acknowledgements

Firstly, I want to thank Dr. Ina Yadroitsava for her guidance, time and motherly love throughout the duration of this thesis. For all the delicious homemade treats and always being friendly to everyone around her and imparting her immense knowledge. Prof. Ihar Yadroitsau (Igor Yadroitsev) for all his patience and sharing his vast knowledge and expertise. It was both a privilege and an honour to be your student and I am ever grateful for the opportunity.

I would like to thank CRPM for manufacturing all the samples. And PDTS, specifically Marinus Potgieter for granting me time off to work on my dissertation. Prof. Anton du Plessis for conducting CT scans on the final 3D objects. My dearest friend Dean Kouprianoff for assisting in all the experimental work and brotherly love. A special thanks to my lovely wife, Minette Newby, for all the love and support and assisting with late night lab work. I also want to acknowledge the help and support of various friends and family, Ian van Zyl, Allan Kinnear, George and Leoni Stroebel, Awie and Tersia Pretorius.

I would like to dedicate this work to my dearest father and mother, Brian and Carol Newby, for granting me every possible opportunity in life and teaching by example.

"Be not wise in thine own eyes: Fear the Lord, and depart from evil."

Proverbs 3:7

This work is based on the research supported by the South African Research Chairs Initiative of the Department of Science and Technology and National Research Foundation of South Africa (Grant №97994).

Abstract

The medical industry has successfully utilised additive manufacturing (AM) technologies, such as laser and electron beam powder bed fusion (LPBF and E-PBF), to manufacture complex shapes from biocompatible materials in order to produce implants using computer aided design (CAD) geometry based on medical Computer Tomography (CT) scan data. AM transforms the original design of the customised digital model directly to the physical device. Modern medicine utilises the benefits of LPBF to manufacture complex customised implants with biocompatible materials. Ti6Al4V alloy is the most used Titanium alloy that has the appropriate mechanical, corrosion and biocompatible properties.

Infection is the most common postoperative complication resulting in device failure after implantation. Copper is a proven antibacterial agent and in small amounts, is not toxic to the human body. Functionalisation of Ti6Al4V implants structure with Cu additions at the bone–implant interface, reduces the risk of bacterial infection.

LPBF combines the advantages of powder metallurgy with complete melting of powder mixtures and provides a unique opportunity for the design of new alloys utilising compositions impossible for conventional methods. Manufacturing of titanium alloys and copper materials from a mixture of elemental powders and *in-situ* mixing and alloying during manufacturing, is an example of such an approach. The formation of *in-situ* Ti6Al4V-*x* at.% Cu (1%, 3% and 5% Cu) alloy structures by LPBF for application in medical implants was investigated. Ti6Al4V Extra low interstitials (ELI) powder was mixed with pure copper powder of similar particle size distribution. Process parameters such as laser power, scanning speed, hatch distance and layer thickness directly affect the surface quality and part density. Optimal process parameters were established for *in-situ* alloying Ti6Al4V-*x*% Cu to form dense parts with suitable microstructural and surface quality. Firstly, single track formation was studied at different scanning speeds for 170 W and 340 W laser powers. The effect of laser power and scanning speed on the track width and shape was described. Secondly, the surface roughness and single layer morphology was considered. Dense non-porous *in-situ* alloyed 3D samples were produced and analysed. Future research on mechanical properties, antimicrobial activity and cytotoxicity is required to substantiate the functional properties of *in-situ* Ti6Al4V-*x* at.% Cu (1%, 3% and 5% Cu) alloys.

Table of Contents

Chapter 3: Materials and Methods 52

Chapter 4. Results and discussion 66

List of Figures

List of Tables

Glossary

AM	Additive manufacturing
ASTM	American Society for Testing and Materials
CAD	Computer aided design
CNC	Computer numerical control
CRPM	Centre for Rapid Prototyping and Manufacturing
CT	Computer tomography
DMLS	Direct metal laser sintering
EDS	Energy-dispersive X-ray spectroscopy
EDM	Electrical discharge machining
ELI	Extra low interstitials
E-PBF	Electron beam powder bed fusion
FCC	Face centred cubic
HAP	Hydroxyapatite
hMSC	Human mesenchymal stem cells
LPBF	Laser powder bed fusion
PBF	Powder bed fusion
ROS	Reactive oxygen species
SEM	Scanning electron microscope
SLM	Selective laser melting
Yb	Ytterbium
3D	Three dimensional

Publications and presentations

- Newby E.B., Yadroitsava I., Krakhmalev P. Kouprianoff D., Yadroitsev I. Investigation of *in-situ* alloying grade 23 Ti with 5at.% Cu by laser based powder bed fusion for biomedical applications. *In Proc. 19th International conference RAPDASA*, 6-7 November 2018, Johannesburg, South Africa.

- Newby E.B., Kouprianoff D., Yadroitsava I. *In-situ* alloying of Ti6Al4V-*x*% Cu Structures by Direct Metal Laser Sintering. *In Proc. 18th International conference RAPDASA*, 7-10 November 2017, Durban ICC, South Africa.

- Kouprianoff D., Luwes N., Yadroitsava I., Yadroitsev I., Newby E.B. On-line monitoring of laser powder bed fusion by acoustic emission. *In Proc. PRASA-RobMech International Conference incorporating the 28th Annual Symposium of the Pattern Recognition Association of South Africa and the 10th robotics and mechatronics conference of South Africa*, Bloemfontein, Central University of Technology, 29 November- 1 December, 2017.

- Newby E.B., Yadroitsava I., Krakhmalev P., Kouprianoff D., Yadroitsev I. Investigation of *in-situ* alloying grade 23 Ti with 3at.% and 5at.% Cu by laser based powder bed fusion for biomedical applications. *CAMS-2018:* Combined Australian Materials Society conference "*Advancing Materials and Manufacturing*", 27-29 November, 2018, Wollongong, Australia.

Chapter 1: Introduction

1.1. Background

Additive manufacturing (AM) is a fairly new technology developed during the 1980's and rapidly improved up to date. ASTM F2792-12 defines additive manufacturing as "*a process of joining materials to make objects from 3D model data, usually layer upon layer, as opposed to subtractive manufacturing methodologies. Synonyms: additive fabrication, additive processes, additive techniques, additive layer manufacturing, layer manufacturing and freeform manufacturing*." Powder bed fusion (PBF) is an AM process in which thermal energy selectively fuses regions of a pre-deposited powder layer. PBF produces parts by means of a layer-by-layer process where powder is spread in a thin layer by a recoating system. In Laser Powder Bed Fusion (LPBF) systems, the laser beam selectively scans a powder layer, fusing the material. After which the recoater spreads a new layer of powder over the fused layer. The laser then scans over again and it forms a multilayer 3D object as illustrated in Figure 1.

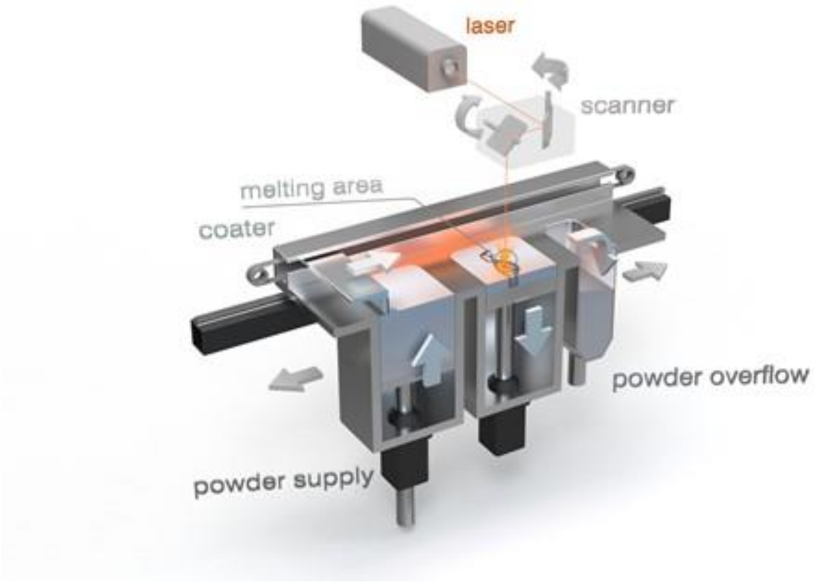

Figure 1. Schematics of the LPBF process (Concept Laser, 2018)

AM technologies, such as LPBF, opened a whole new world to the manufacturing industry; previously impossible designs and manufacturing concepts are now made possible with LPBF. Complex shapes and objects were manufactured by utilising LPBF (Figure 2).

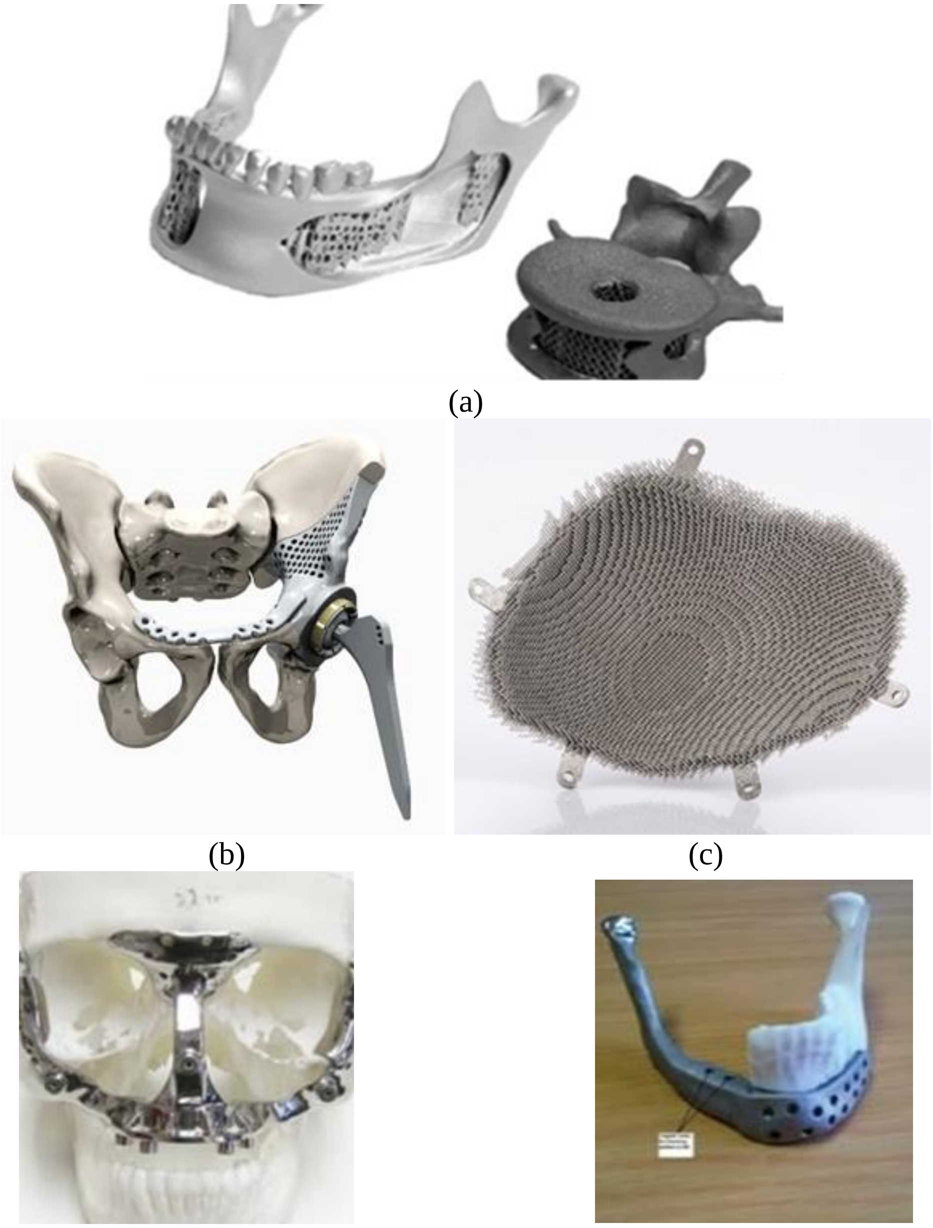

(a)

(b) (c)

(d) (d)

Figure 2. From models to applications: (a) LPBF models of Ti6Al4V implants (Wehmöller et al., 2005), (b) artificial hip together with the integrated joint replaces all of the bone affected by cancer, (c) implant made of a biocompatible titanium alloy that was placed in the skull of a patient in Argentina who required it after a stroke-related incident (EOS, 2018), (d) maxilla and (e) mandible implants produced in CRPM at Central University of Technology, Free State

Laser Powder Bed Fusion (LPBF), Selective Laser Melting (SLM) and Direct Metal Laser Sintering (DMLS) are synonyms. Different suppliers of LPBF systems use their own terms. EOS, producer of systems for the additive manufacturing of components in metal and polymers, uses the term “DMLS”, metal additive manufacturing or even “3D printing” (EOS, 2018). Renishaw indicates that they apply “metal powder bed fusion technology”, also referred to as “layer melting, metal additive manufacturing, metal 3D printing, laser sintering and metal AM”. SLM Solutions and Realizer call this technology “SLM” and Concept Laser calls it “LaserCusing”.

With additive manufacturing, the process chain for implants starts with a diagnosis and use imaging and scanning, which is produced through various scanning procedures such as Computer tomography (CT), to convert data into a 3D digital form (Figure 3). AM transforms the original design of the customised implant to the physical model. The medical industry has successfully utilised the layer-by-layer LPBF technology to manufacture complex shapes from biocompatible powder materials to produce implants using computer aided design (CAD) geometry based on CT scan data. After building the implant, post processing such as stress relieving, heat treatment and surface finish is required to comply with the mechanical and fatigue properties of bones (Javaid and Haleem, 2017).

To avoid problems in LPBF, careful selection of process parameters and manufacturing strategies for employed powders by different LPBF systems should be used to avoid porosity from incorrect processing parameters or build conditions, surface roughness and cracks, and reduce high residual stresses and deformation during processing. Due to these challenges, especially for high value and critical parts, such as those for aerospace or medical applications, process qualification is required and part quality must be validated. This is discussed in a general review of additive manufacturing and a review of the use of micro computed tomography to overcome these issues (du Plessis *et al.*, 2018; DebRoy, 2018)

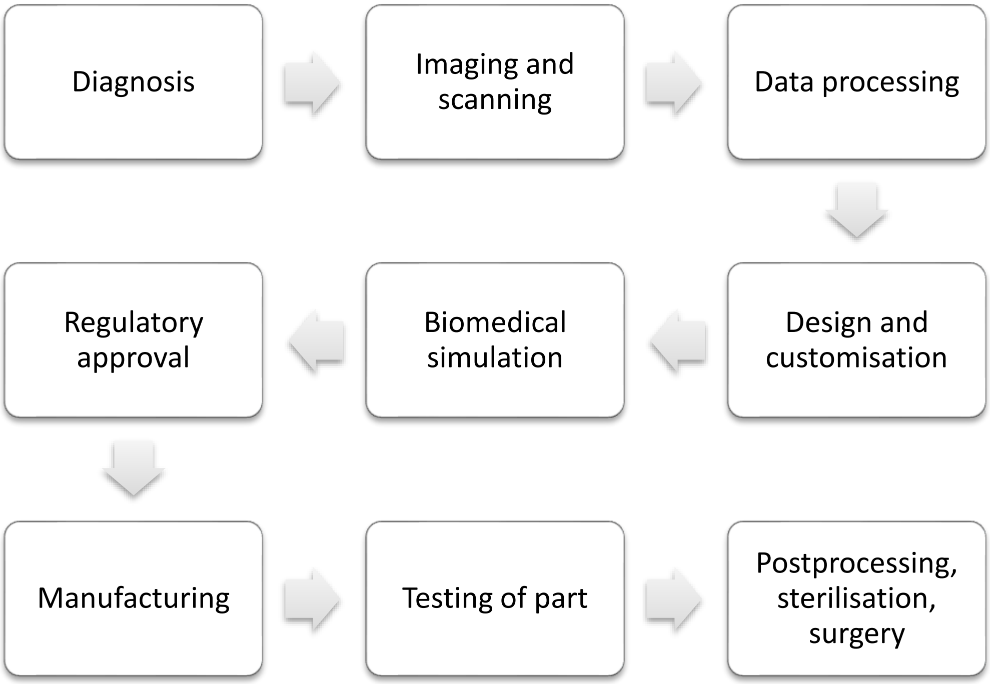

Figure 3. Process chain development in medical application of Additive Manufacturing (modified from Javaid and Haleem, 2017)

Modern medicine utilises the benefits of LPBF to manufacture complex customised implants with high grade biocompatible materials. Titanium alloys have been widely used in the biomedical field, and particularly applied for load-bearing orthopaedic implants and dentistry (Wang, 1996). Ti6Al4V (ELI) (Extra Low Interstitials) alloy is commonly used for implants because of its suitable mechanical, corrosion and biocompatible properties (Donachie, 2000).

Infection is the most common postoperative complication resulting in implant failure. It has been reported that more than 65% of human nosocomial infections (*i.e.* originating in a hospital) were caused by bacterial bio-films (Montanaro *et al*., 2011). Tsai and Caterson (2014) indicated that 1.7 million healthcare-associated infections occur per year in USA. Surgical site infections alone account for 290,000 cases and approximately 8,000 deaths. Approximately half of all nosocomial infections are associated with indwelling devices (Darouiche, 2004).

Titanium biomaterials are less susceptible to bacterial adhesion than stainless steel (Gad *et al.*, 2012), but commercially available titanium alloys do not exhibit antibacterial capability after implantation, as it is a kind of bio-inert material, bacterial infections associated with implants occur occasionally (Guo *et al.*, 2017). Coating the bone-implant interface with materials that possess antibacterial properties (Ag, Zn and Cu) is a promising approach to infection prevention. Copper is a proven antibacterial agent and in small amounts is not toxic to the human body (Liu *et al.*, 2014, 2016). Implants can be constructed to have a biocompatible Ti6Al4V structure with copper additions at the bone–implant interface to reduce the risk of bacterial infection and implant failure.

In orthopaedic surgeries, *Staphylococcus aureus* (*S.aureus*) and *Escherichia coli* (*E.coli*) are the main pathogenic microbes responsible for the implant-related infections (Campoccia *et al*., 2006). It was shown that the *in-situ* alloyed LPBF Ti6Al4V-at.1 % Cu was capable of inhibiting the growth of *E. coli* and *S. aureus* (Krakhmalev *et al*., 2017).

The advantage of laser powder bed fusion is that complex shapes can be produced which enables production of custom once-off components; for example, bio-medical implants shaped to fit the patient and the exact requirements for bone replacement, but the part quality depends on the manufacturing parameters used.

Manufacturing of titanium alloys and copper materials from a mixture of elemental powders, *in-situ* mixing and alloying during manufacturing is an example of such an approach. As mentioned above, the LPBF process is a laser beam scanning over the surface of a thin powder layer. The laser beam melts material along a row of powder particles, forming a molten pool and finally a single track. Regular single tracks formed from a stable molten pool is the most basic building block in the LPBF process. Optimal formation of the molten pool and single tracks play a major role in the quality and mechanical properties of manufactured 3D objects. Single track formation is directly influenced by these process parameters. With optimal process parameters, LPBF single tracks are continuous and have stable geometrical characteristics with optimal penetration depth. Choosing an appropriate hatch distance and scanning strategy is the next step for LPBF optimisation. Surface roughness and morphology of the single layers, at different hatch distances and scanning strategies differ. Surface quality influences the building process, since a single layer is the substrate for the next delivered powder layer. Additionally, for the *in-situ* alloying approach, molten metals should have a low viscosity, and the molten pool should exist long enough to guarantee sufficient mixing of the components. Thus, optimal process parameters and appropriate scanning and building strategies have to be determined for *in-situ* alloying by LPBF (Yadroitsev *et al*., 2015).

1.2. Aim of the Project

The main purpose of this study is to investigate the relationship between the process parameters and properties of sintered objects by LPBF with *in-situ* alloying of blended Ti6Al4V(ELI) (grade 23 Titanium alloy) and 1, 3, and 5 at.% Cu powders for biomedical applications.

1.3. Scope of the Project

This study is concerned with the properties of *in-situ* alloyed LPBF Ti6Al4V-*x*Cu for biomedical applications.

1.4. Research Methodology

Following the above goals and objectives, the research methodology was designed (Figure 4). A literature review of the LPBF process and an analysis of *in-situ* alloying by LPBF was done. Titanium alloys and their properties, features of powder handling and characterisation, the EOSINT M280 machine, metallographic methods and microscopy have been studied. An analysis of powder layering and surface roughness of the substrate, for accurate delivery of a single layer with the prescribed layer thickness, was done. Optimal process parameters and scanning strategy, on employed powders, were estimated by analysis of the morphology of the single tracks and layers by conducting studies of cross-sections and X-ray CT scans.

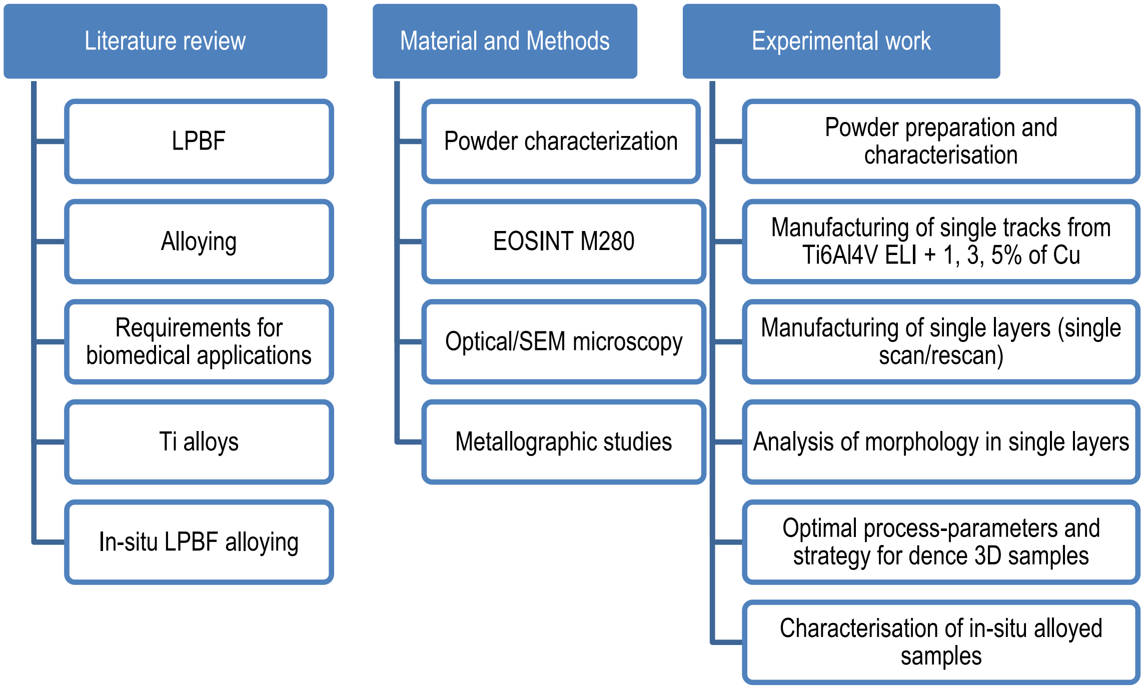

Figure 4. Flow chart for research methodology

Scanning electron microscope (SEM) and optical microscopes were used for the analysis of the porosity and distribution of copper in single tracks, layers and 3D objects with different process parameters. The final step of the study analysed the microstructure and mechanical properties of Ti6Al4V ELI–Cu specimens. Conclusions concerning the possibility of LPBF manufacturing of non-porous, solid, homogeneous 3D LPBF samples from blended Ti6Al4V ELI (grade 23 Titanium alloy) and 1,3, and 5 at.% Cu powders were drawn.

1.5. An overview of the dissertation

This dissertation comprises of five chapters, the introduction being the first chapter.

- Chapter 1 presents the background, objectives and research methodology.
- Chapter 2 presents the literature review relating to the study. The basic knowledge on different topics related to this study is presented. The topics covered are: principles of LPBF; key process parameters in LPBF; physical phenomena; microstructure and mechanical properties of Ti6Al4V with different process parameters are also reviewed.

- In Chapter 3, the materials used and the experimental methodology are presented. The equipment used for material characterisation, single track formation, sample preparation and examination are fully described in this chapter. Powder properties are also described.
- Chapter 4 presents the results obtained and a discussion on the characterisation of the single tracks at 1-5 at.% Cu addition to Ti6Al4V powder. The effects of process parameters on the surface morphology and melt pool profile are analysed and discussed. The main effects are also presented with graphs.
- Chapter 5 summarizes the results, and draws conclusions. Recommendations for future work are also suggested in this chapter.

1.6. Expected contributions

This study validates the optimal process parameters of Ti6Al4V-1, 3, 5 at.% Cu implants.

Chapter 2. Literature Review

2.1. Laser Powder Bed Fusion

2.1.1. State of the art review on LPBF

Laser Powder Bed Fusion (LPBF) dates back to 1979, where a private inventor R.F Housholder patented the process without it being commercialised. During the 1980’s, an undergraduate named Carl Deckard from the University of Texas saw that there would be a big market for an automated method for creating casting patterns out of CAD models. Deckard spent two and a half years developing such a method. By the end of 1984, Deckard had come up with the idea of using a direct energy beam (such as a laser or electron beam) to melt particles of powder together to produce a three-dimensional object. The first machine Deckard built, called “Betsy”, used a 100 W YAG (synthetic crystal yttrium aluminium garnet) laser.. Deckard filled a small box with powder by hand using a device similar to a salt shaker while a computer ran the scanner on the table (Figure 5).

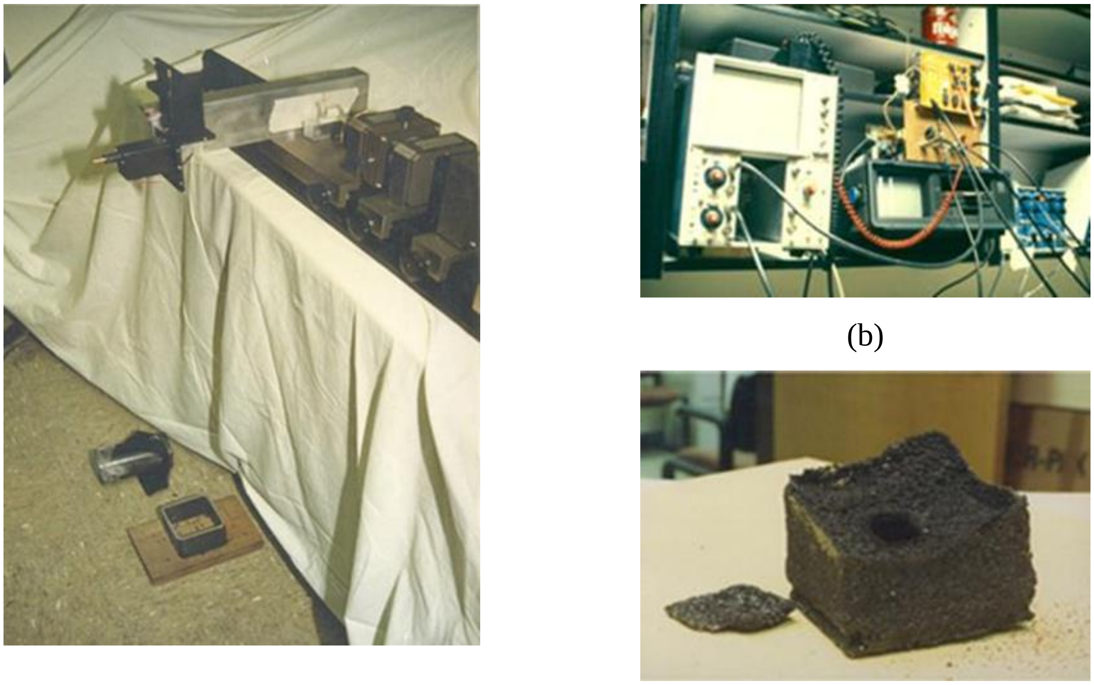

(b)

(a)

(c)

Figure 5. “Betsy” machine (a), instrumentation for the “Betsy”(b), one of the first plastic parts Deckard created with “Betsy” (c) (The University of Texas, 2017)

Since "Betsy", additive manufacturing technology has developed significantly. In 2013 the American Society for Testing and Materials (ASTM) defined LPBF as "*a powder bed fusion process used to make metal parts directly from metal powders. Powder bed fusion is described as an additive manufacturing process in which thermal energy selectively fuses regions of a powder bed*" (ASTM International, 2013).

Laser Powder Bed Fusion (LPBF) has opened a whole new world to the manufacturing industry; previously impossible designs and manufacturing concepts are now made possible with LPBF. Complex shapes and objects could be manufactured by utilising the layer-by-layer scanning process of LPBF.

Currently much research and development is in progress to ensure optimal process parameters for a number of metal powders. LPBF is widely used in the medical field as well as in aerospace and other engineering applications. The new and innovative manufacturing technique of AM has seen massive sales growth in the past years (Figure 6). According to the 2015 Wohler's Report, the AM industry has experienced significant growth, during the last 5 years "the market has nearly quadrupled".

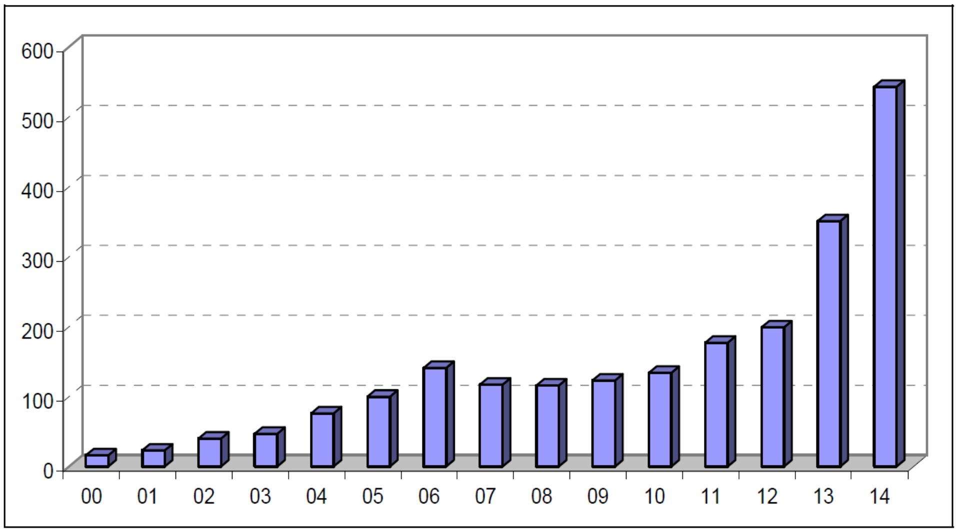

Source: Wohlers Associates, Inc.

Figure 6. Growth in the market of AM systems in metal part (Wohler's Report, 2015)

Electro Optical Systems (EOS), SLM solutions, 3D systems, Renishaw, Concept Laser, *etc.* produce commercial LPBF machines. The new generation of LPBF machines are more accessible to the manufacturing and prototyping industry than ever before with a wide range of machines available.

The EOSINT M280 has a 200 W or optional 400 W Yb-fiber laser and a build platform volume of 250 x 250 x 325 mm. EOS also produces the M290 that comes standard with a 400 W fibre laser. Their large industrial machine, the M400, has a 400 x 400 x 400 mm build platform volume. Productivity is increased with a 1000 W fibre laser and a dual recoating system. Dual recoating refers to powder deposition from both sides of the powder delivery platform, reducing non-productive machine time (EOS GmbH, 2018).

The ability to respond immediately, precisely and relatively inexpensively draws LPBF to the forefront of mainstream low volume production. Advances in this sector have the capability to bridge the gap between prototype and production scenarios. LPBF has more to offer than just complex geometries and prototyping, but offers the market a new way of producing components otherwise impossible, that meet the exact market need (Bertol *et al.*, 2010).

2.1.2. LPBF Process

At the core of the LPBF process is a laser beam scanning over the surface of a thin powder layer. As the laser beam melts material along a row of powder particles, it forms a molten pool. Each layer of the part is sequentially filled with elongated tracks of melted powder lines referred to as single tracks (Figure 7a). Single tracks or the continuous formation of the molten pool, is the most basic building block in the LPBF process. The previously re-melted layer or the substrate, forms the platform for the new layer of powder to be deposited and the process repeats. Layers are formed by applying multiple single tracks next to one another or also known as track-by-track formation of the molten pool boundaries (Figure 7c). Objects are formed by placing multiple single tracks layer by layer upon one another (Figure 7b). Thus the optimisation of the molten pool and single track formation plays a major role in the quality and properties of the produced 3D object.

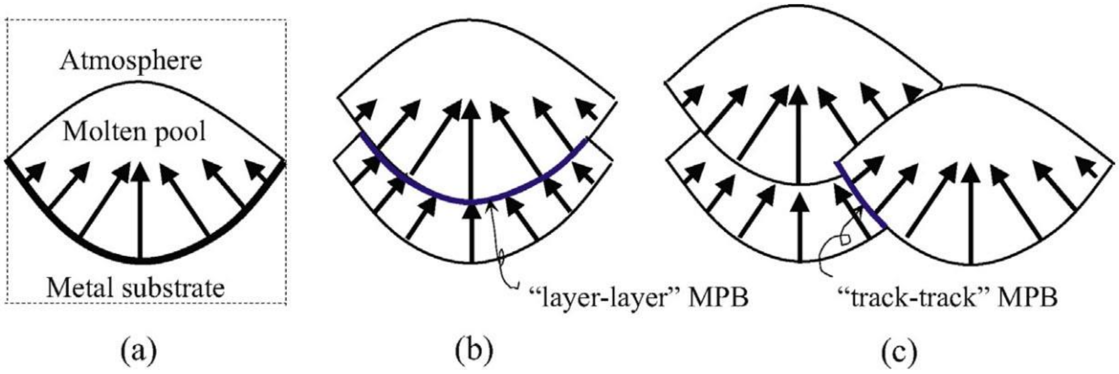

Figure 7. Schematic diagram of the molten pool configuration during the LPBF process: (a) Single molten pool (b) layer-layer showing the molten pool boundary c) track-track MPB (Shifeng et al., 2014)

2.1.2.1 Single tracks

During single track formation, a laser beam melts powder along a path predetermined by a software interface, whereby a molten track is created in the powder particle bed (Figure 8). This track can break up into individual spheres (drops) also known as the "balling" effect (Tolochko *et al.*, 2004). If the surface diffusion controls the break-up process, a high surface tension will enhance the kinetics of the molten cylinder (Yadroitsev, 2009). The instability of the molten pool appears both at the lower and upper bounds of scan speed intervals.

A single track is formed not only from powder placed directly under the laser spot. Adjacent particles are involved in the process due to scattering of radiation, conduction through the substrate and neighbouring particles, capillary phenomena, etc. The denudation zone, *i.e.* area without powder after laser scanning, can be twice as large as the width of the track. Figure 9 shows the corresponding height map for the optical micrograph for a single track produced at 0.5 – 220 Torr. At 5 and 220 Torr, the edge of the powder layer appears near the nominal thickness of ~60 µm, whereas from 2.2 to 0.5 Torr the powder thickness at the denudation zone edge is two times higher, suggesting that material has been pushed away from the track centre (Matthews *et al.*, 2016). Low pressure promotes a more stable track, thus varying the process parameters can optimise the stability of the track and ultimately the morphology of layers (Figure 10).

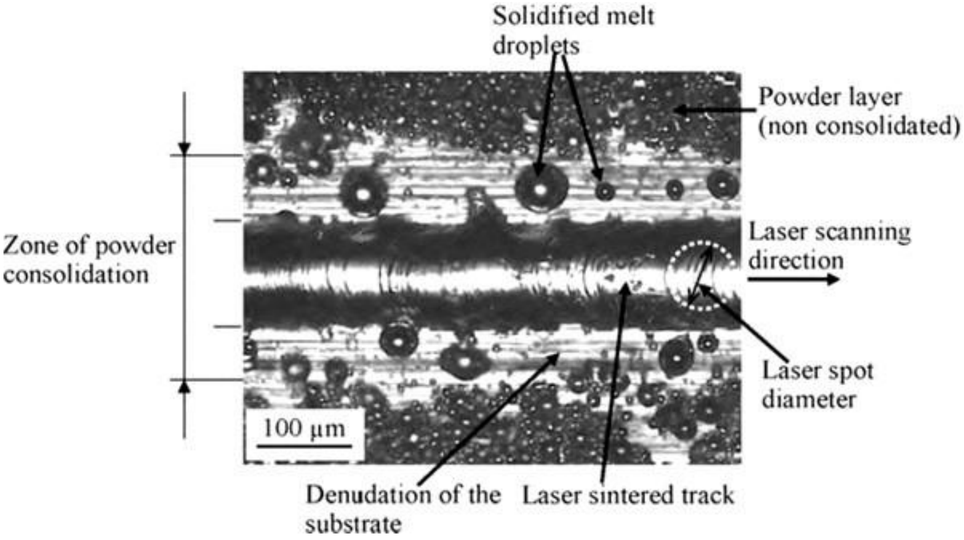

Figure 8. Single track formation (Yadroitsev, 2009)

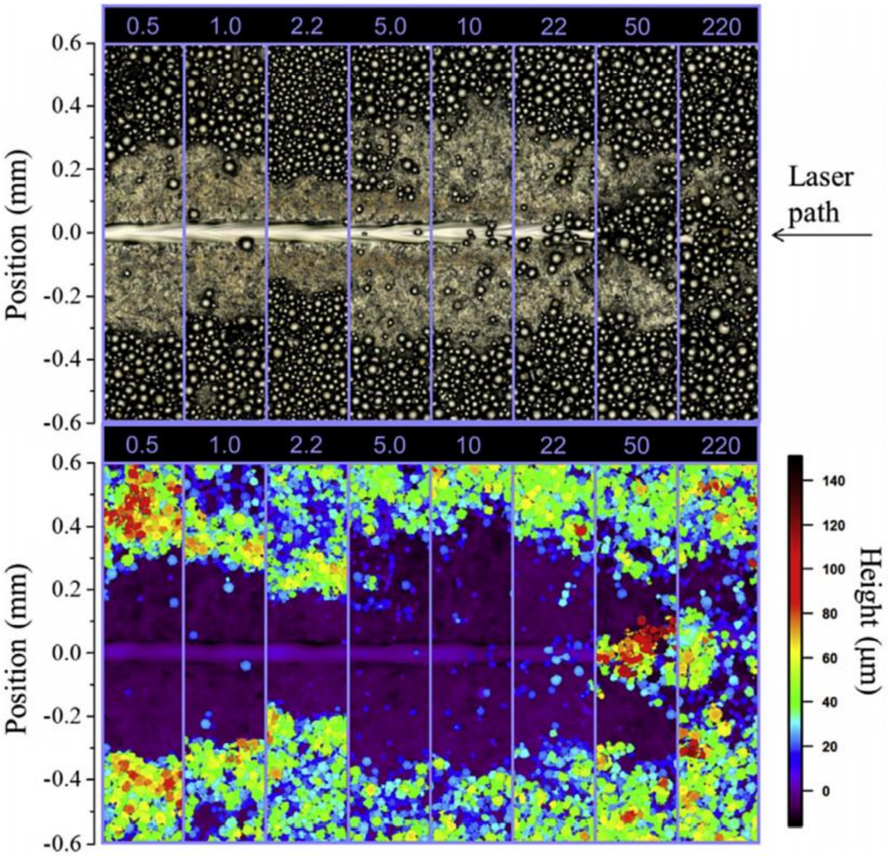

Figure 9. Montage of mm optical micrographs (top) and height maps (bottom) of the solidified melt track within a powder layer following scanning laser exposure at 225 W and 1.4 m/s as a function of ambient Ar pressure (shown above image slices in Torr). Three distinct regions can be identified near the laser path centre, namely track accumulation zone, the denuded zone (DZ), and the background powder zone (Matthews et al., 2016)

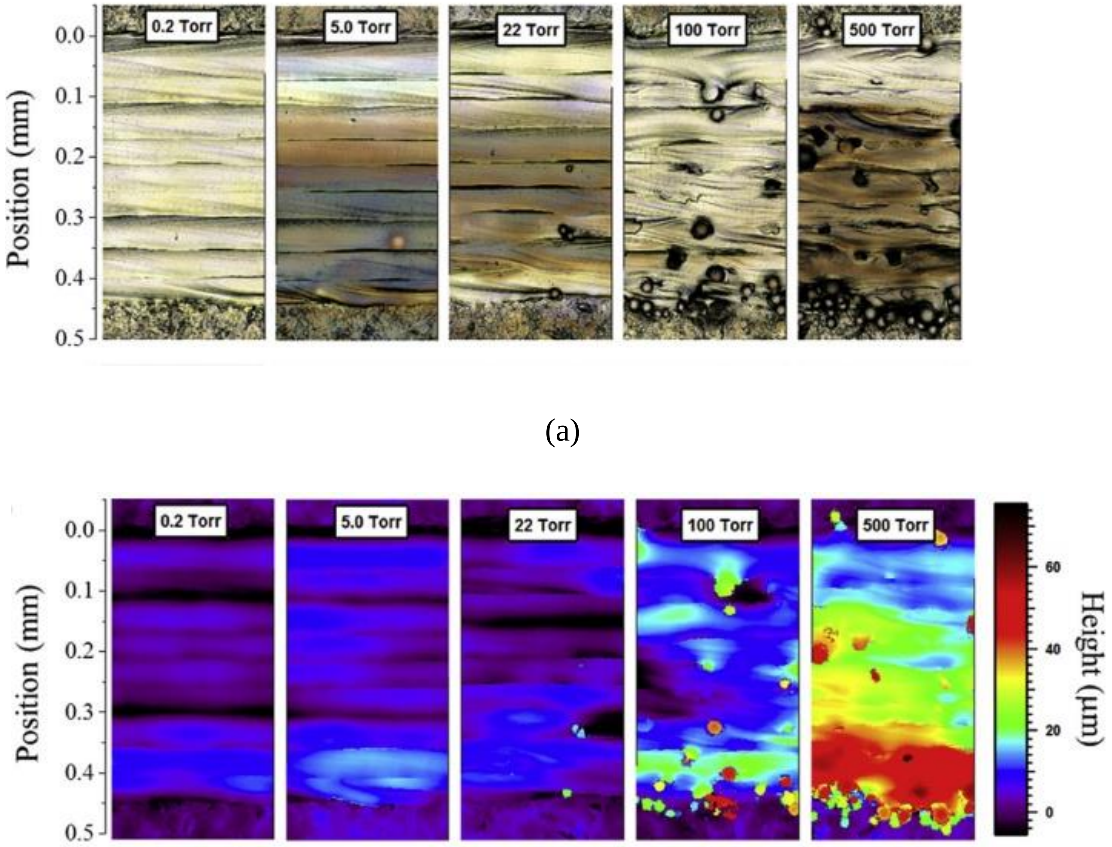

(a)

(b)

Figure 10. Montage of micrographs (a) and confocal height maps (b) of 9 overlapping laser tracks as a function of ambient pressure (Matthews et al., 2016)

Capillary instability of the melt pool explains track failure for higher scanning speeds at high length-to-width ratios when it fragments with reducing surface energy. For example, for 904L steel powder, the contact zone between the remelted powder and the substrate tends to vanish at $V > 0.2$ m/s for a laser power of 50 W. When scanning speed decreases, the length of the molten pool decreases and its width increases. A more stable behaviour is expected from molten pools with a greater circumference-to-length ratio (Figure 11). Therefore, the upper stability limit of the scanning speed can be related to the loss of contact between the molten powder and the substrate (Yadroitsev *et al*., 2010).

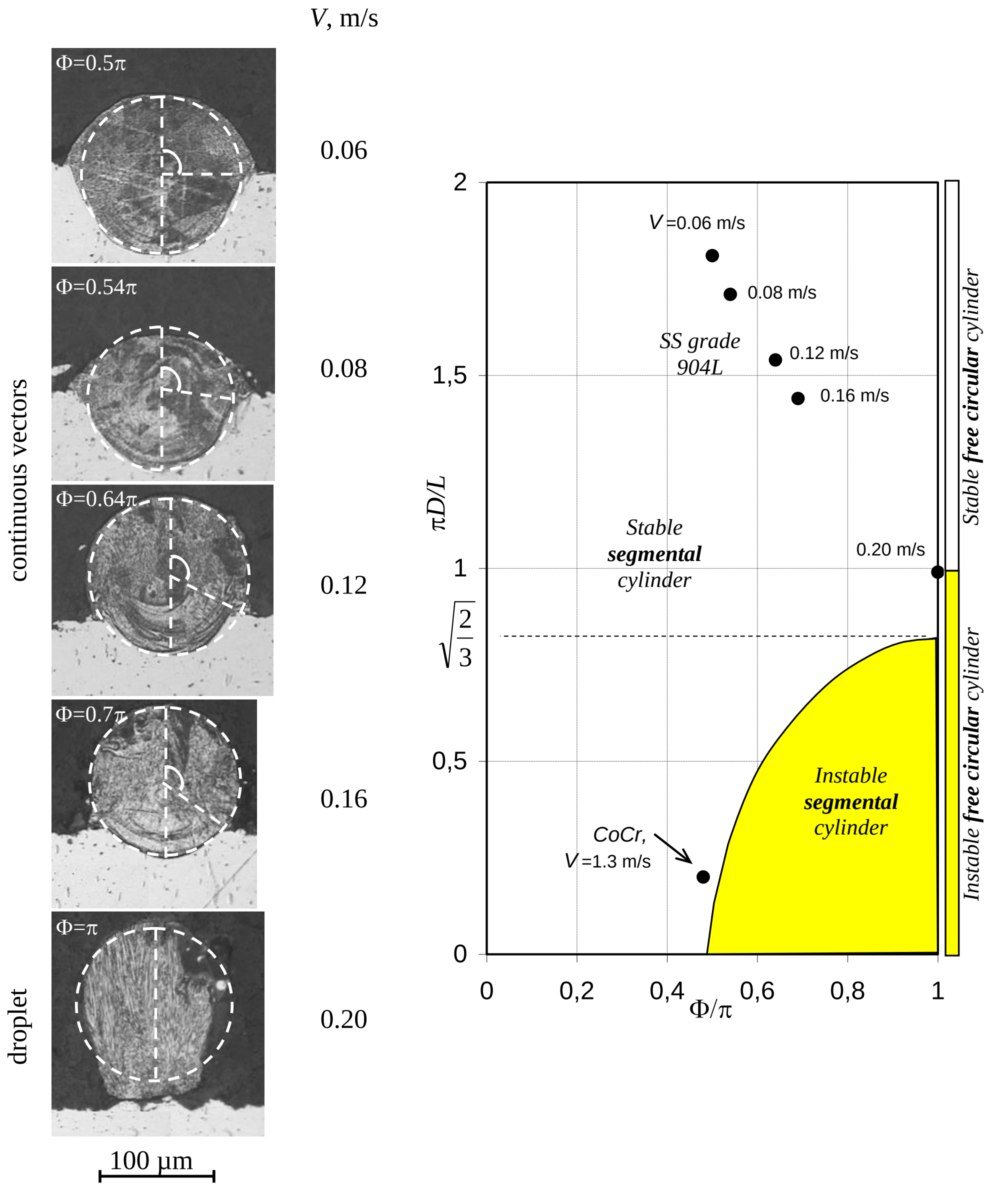

(a) (b)

Figure 11.Cross-sections of laser sintered tracks from SS grade 904L powder on steel substrate (a) and (b) stability map for segmental and free circular cylinders. Φ is the angle. (Yadroitsev et al., 2010)

With increased energy input per unit length (*P/V*), at a comparatively high laser power and lower scanning speed, the LPBF process is accompanied by an increase of the melt volume and a decrease of the melt velocity. The melt hydrodynamics, driven by the Marangony effect, becomes increasingly important and irregular sintered tracks appear (Digilov, 2003). At slower scanning speeds and lower laser power, energy to melt the substrate becomes insufficient and the stabilising effect of the contact zone (penetration into the substrate) reduces. If the energy is enough to maintain boiling and evaporation of the molten powder, the vapour recoil pressure causes distortion of the sintered tracks (Figure 12a). With further reduction of laser power, the tracks become a series of droplets (Figure 12b).

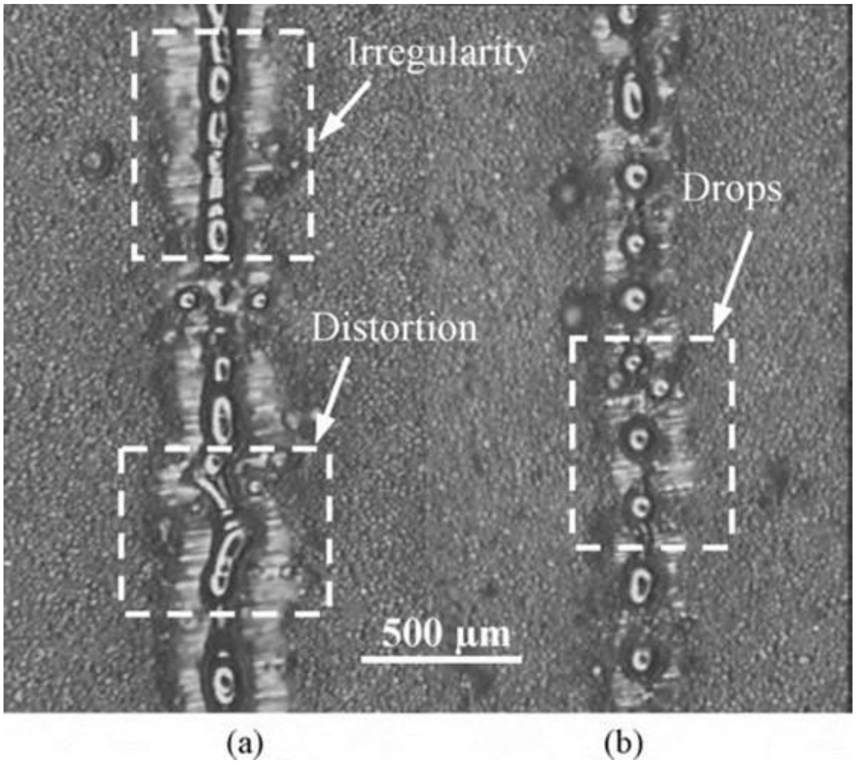

Figure 12. Instability of laser sintered tracks from SS grade 316L on steel substrate. Thickness of the deposited powder layer is 50m, scanning speed V = 0.02 m/s: (a) P=25 W, (b) P = 12.5 W (Yadroitsev et al., 2010)

When looking at the other extreme, higher laser power results in too deep penetration into the previous layer or substrate. Penetration like a keyhole is unacceptable in LPBF because it can promote pores in the final 3D object due to the collapse of the molten pool and gas bubbles trapped in the material (Thijs *et al*., 2013). From an energy and resource efficiency point of view, a penetration much deeper than the layer thickness is also unsuitable. With non-optimal process parameters, the tracks have irregularities, balling effect and distortions (Yadroitsava *et al*., 2015a). These effects may be associated with the thermo-physical properties of materials, granulomorphometric characteristics of the powder and inhomogeneity in the powder layer thickness; energy input parameters such as spot size, scanning speed, laser power and melt hydrodynamics (Yadroitsev *et al.*, 2010).

Process parameters, utilised by LPBF, directly influence single track formation of the material. Single track formation is the first step in forming the final 3D object. When the optimum process parameters are employed, single tracks are continuous and the metallurgical bond with the substrate or previously melted layer is consistent.

2.1.2.2 Single layers

A single layer is a series of single LPBF tracks next to each other. The surface morphology of a single layer is influenced by factors such as geometrical characteristics of single tracks, scanning strategy and hatch distance. The hatch distance is the distance between scan line centres. Non-uniform powder layer thickness, of the next deposited layer, could be critical because a defective porous structure will be produced. Single layer morphology after follow-up scanning (also known as one-zone scanning) is complex. If the hatch distance is more than the width of a single track, the powder is melted in a sequence of individual tracks (Figure 13). Non-optimal hatch distance can result in formation of gaps between tracks in a single layer, which causes a sequence of cavities in the final LPBF object (Yadroitsev *et al.*, 2015). Figure 16 illustrates the influence of hatch distance on layer morphology. The variation of hatch distance from 60, 120 and 240 µm shows that as the hatch spacing increases, less powder is sintered. At 240 µm hatch distance, the majority of powder is not sintered. Therefore, optimal hatch distance must be selected to avoid pore formation in 3D objects.

Scanning strategies or laser scan paths, are the patterns formed by the tracks of each layer; in Figure 14 a variety of such paths are seen. To ensure a sound metallurgical bond between tracks, the hatch distance is of critical importance. With a two-zone strategy (rescanning), each layer is scanned twice with the laser; at first the laser beam melts the powder layer with a specific hatch distance, thereafter the laser beam passes between the previously sintered tracks and re-melts the two neighbouring tracks (Figure 15). Rescanning significantly improves the surface quality of single layers; it causes the disappearance of droplets and the reduction of surface roughness of the sintered layer, with the disadvantage of increased build time (Yadroitsev, 2009).

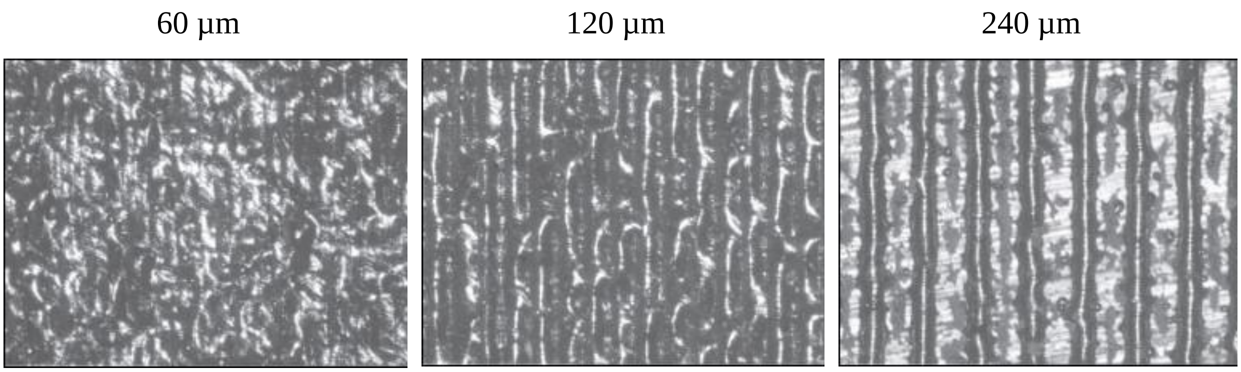

Figure 13. Surfaces of the first layer from SS grade 904L powder obtained at different hatch distances (60, 120 and 240 µm). Powder layer thickness on steel substrate is 50 µm, laser power is 50 W, and scanning speed is 0.14 m/s (Yadroitsev, 2009)

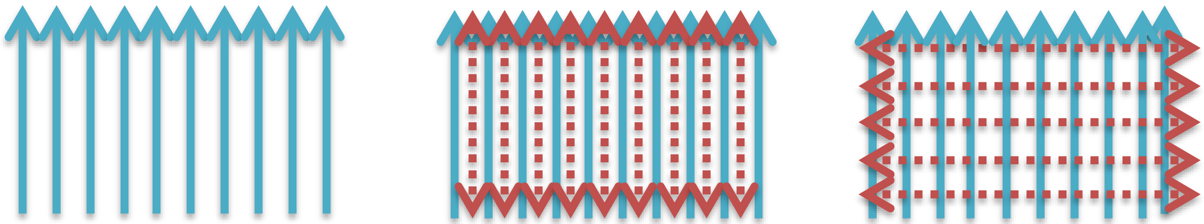

one-direction   two-zone (rescanning)   two-zone cross-hatching

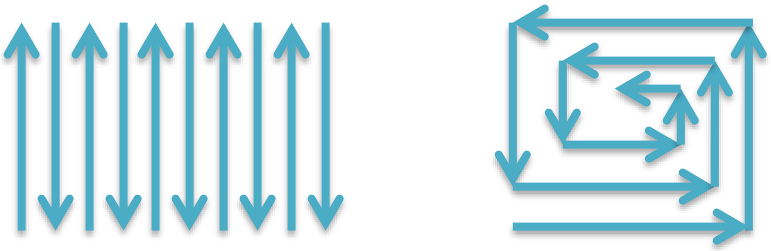

back and forth (zig-zag)   spiral

Figure 14. Different scanning strategies of a single layer

Figure 15. Top view of single layer produced by one-zone (a) and two-zone strategy (b) of laser scanning. Laser power P = 50 W; layer thickness h = 50 µm; scanning speed V = 0.12 m/s; hatch distance s = 120 µm (Yadroitsev et al., 2015)

Optimal parameters will consequently lead to homogenous layers with constant thickness and bonding between tracks. As mentioned previously, it is clear that LPBF is a parameter sensitive process. Another important factor is powder layer thickness. LPBF thin walls have specific surface morphology and is sensitive to powder layer thickness (Figure 16).

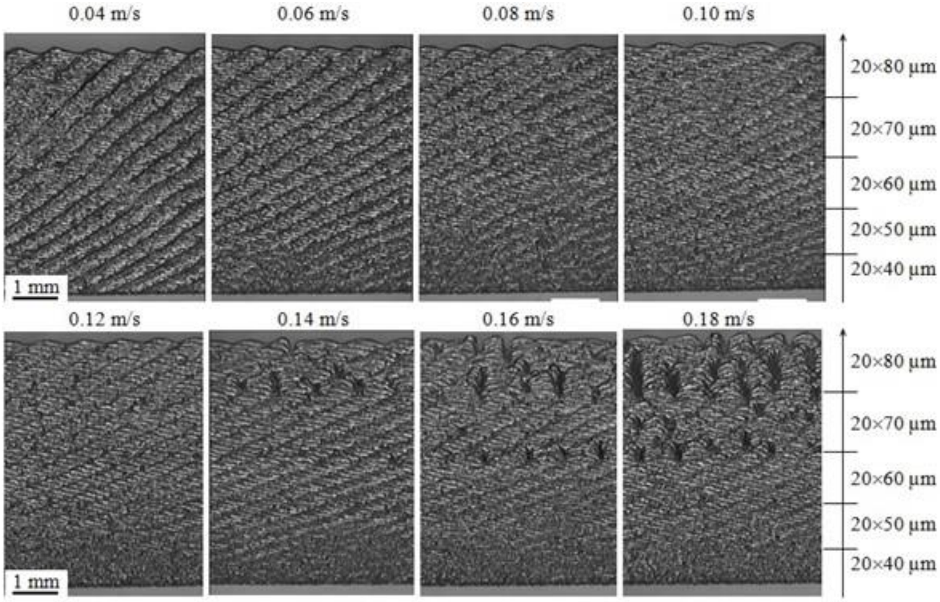

Figure 16. Laser sintered thin walls from SS grade 316L powder. Thickness of powder layers varied from 40 to 80 µm with a step of 10 µm, 20 layers for each thickness, V=0.04–0.18 m/s, P=50 W (Yadroitsev, 2009)

Scanning patterns may be the same throughout multiple layers, in either the *x* or *y* directions, or the scanning direction can be rotated around the *z*-axis from layer to layer (Figure 17). As previously stated, hatch distance is one of the defining parameters to produce fully dense parts.

Porosity will increase if the hatch distance is too wide, which will weaken the final mechanical and structural properties of the part. Whereas with a too narrow hatch distance, production time and cost will increase.

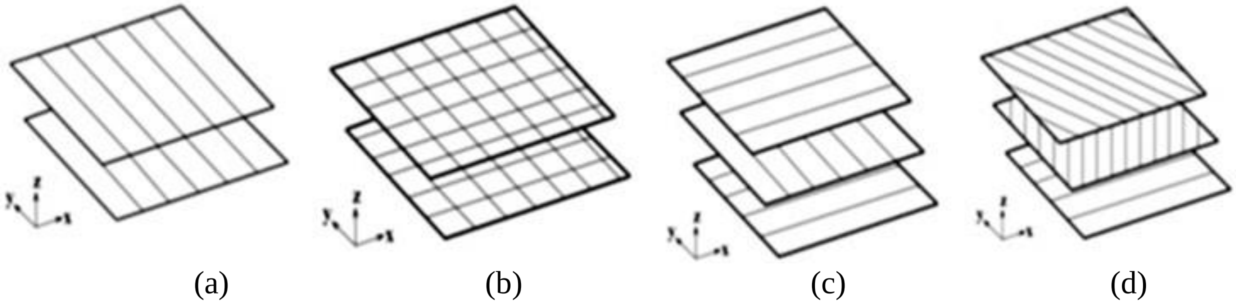

Figure 17. Different scan patterns for consistent layers: (a) one direction (b) double scanning each layer (c) alternating scanning (d) the direction of scanning rotated of certain angle between consecutive layers (Manfredi et al., 2014)

Scanning strategies vary from different AM manufacturers. For example, the “island style” strategy, with islands that range from 1 mm x 1 mm up to 10 mm x 10 mm is used by Concept Laser. These islands are not always scanned coincident with each other, but rather stochastically (Concept Laser, 2018). The combination of all of these islands form a single layer.

2.1.3.3 LPBF 3D objects

Laser energy has a fundamental impact on the quality of final 3D objects. The energy input has a direct influence on the characteristics of the molten pool formation when the powder changes to a liquid state. Meier and Haberland (2008) studied how laser power influences part density. It was found that a decrease in power leads to greater porosity within created parts (as shown in Figure 18). The greater laser power shows better interlayer penetration. The higher power input obviously created a more homogenous melt pool, allowing sufficient heat energy for the material to fuse. However, excessively high laser power density causes keyholes at low scanning speeds or instability of long shallow molten pools at high scanning speeds (Yadroitsev *et al.*, 2010; Thjis *et al.*, 2013). A number of publications were dedicated to the analysis of laser scanning strategies and related defects in 3D objects (Yasa *et al.*, 2011; Wang *et al.*, 2013; Casalino *et al.*, 2015). It has been shown that different scanning strategies resulted in different defects and caused anisotropy of mechanical properties of LPBF samples.

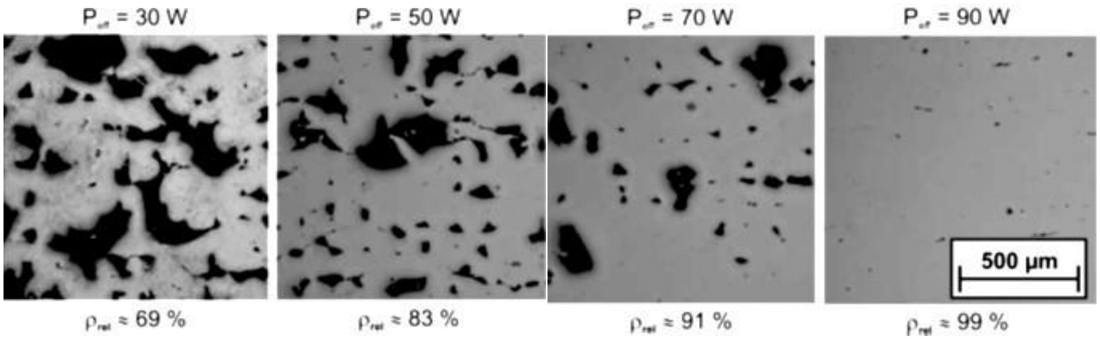

Figure 18. Difference in density at different laser power for al 316L Stainless Steel (Meier and Haberland, 2008)

When manufacturing complex shaped objects with overhanging elements, the geometrical characteristics of its tracks depend on local geometry of the LPBF object (Wang *et al.*, 2013). Specific scanning strategies and process parameters can be used for different sections of such complicated objects. Final porosity has also been discussed and correlated to process parameters in Ti6Al4V (Sun *et al.*, 2013), 18Ni Maraging 300 steel (Casalino *et al.*, 2015) and AlSi10Mg (Thjis *et al.*, 2013) alloys. It was suggested that porosity is related to the energy input into the powder layer and scanning strategy.

To produce continuous and stable single tracks, optimum laser power, laser spot size and scanning speed for different powder layer thicknesses must be used. The initial powder layer thickness could be chosen in respect of the particle size of the employed powder. The geometric characteristics of the tracks affect the choice of subsequent scanning strategies and hatch distances. Choosing a scanning strategy defines the layer’s morphology which in turn affects the subsequent layer thickness, regularity and continuity. The high quality of the synthesized single layer should guarantee that the thickness of the next deposited powder layer does not vary greatly, preventing further irregularity and balling effect. Thus, the feedback is established between energy input parameters and selected layer thickness for powders with a specific particle size distribution (Yadroitsev *et al.*, 2015).

The aforementioned strongly indicates that process parameters of LPBF is critical for the production of successful 3D objects with suitable properties for different materials and application; a schematic of the selection process is shown in Figure 19 and illustrates the necessary areas of focus when evaluating or developing a set of parameters for successful manufacturing of 3D objects by LPBF for different materials.

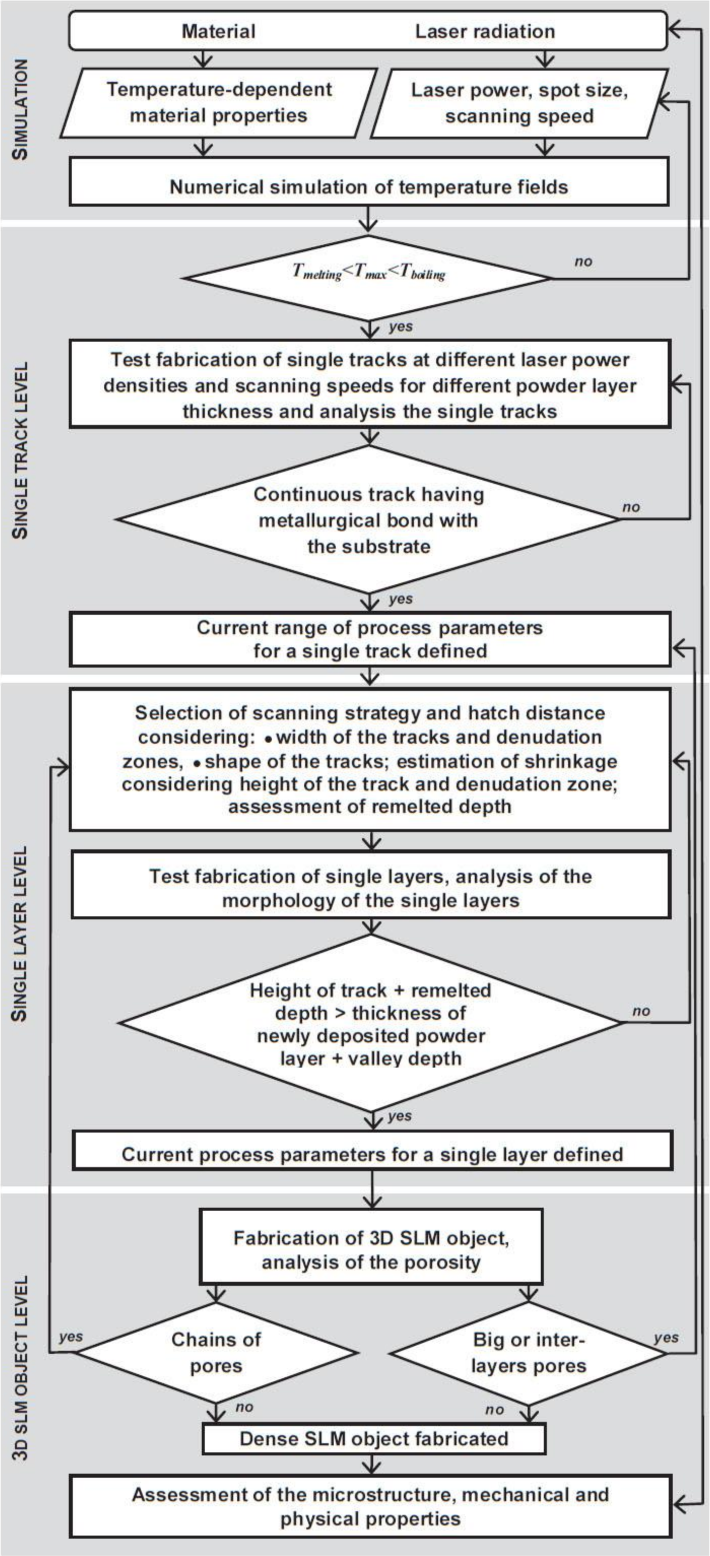

Figure 19. Algorithm for optimal LPBF process parameters (Yadroitsev et al., 2015)

2.1.3.4. Residual stress

The macro-residual stress present in parts produced by LPBF is known as thermal residual stress; solidification during rapid thermal change induce and lock-in these stresses within a component (Vrancken *et al.*, 2013, 2014; Yadroitsava *et al.*, 2015b, Yadroitsev *et al.*, 2015). High thermal gradients result in high residual stress in the LPBF samples. When the laser beam fuses material, the temperature of the surrounding solid material near the molten bath, that is the heat affected zone (HAZ), increases. Thermal conductivity defines the heat dissipation and temperature-equalisation in solid material. Since the thermal expansion coefficient has a tendency to increase with the temperature, during LPBF, the peak value of the compressive stress appears in the interface between the molten pool and HAZ area. When the laser beam leaves the irradiated zone, the molten pool begins to solidify, cool down and shrink. Various layers of material cool down at different rates; therefore, the contraction occurs at different speeds, causing the plastic flow (Figure 20). Laser processing of new tracks and layers will cause stresses and deformations near the molten pool, creating a complex superposition of strains and stresses (Yadroitsev & Yadroitsava, 2015).

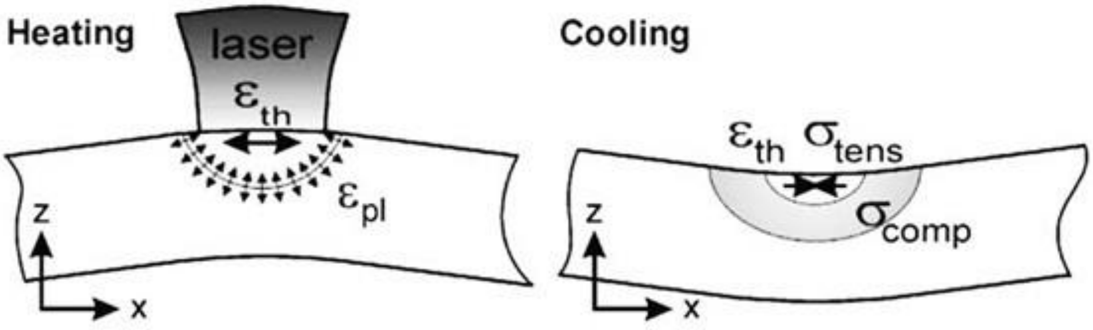

Figure 20. Heating and Cooling phenomena of laser passes (Mercelis and Kruth, 2006)

Plastic deformations in the surrounding material and in the solidifying track occur as a result of lowered yield strength at the elevated temperature. Thus, non-uniform deformation of the material results in residual stress being present in the LPBF parts (Yadroitsev & Yadroitsava, 2015). The residual stress observed with LPBF deteriorates the parts performance dramatically and induces distortion (Figure 21).

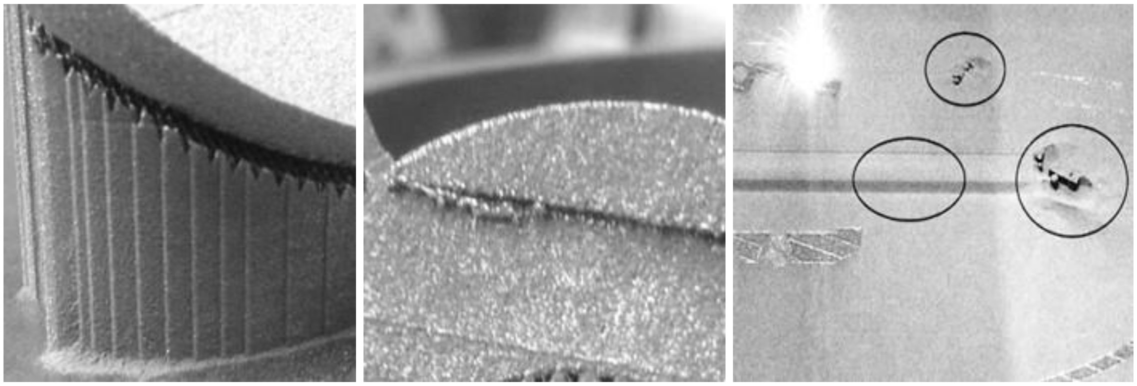

(a) (b) (c)

Figure 21. Delamination from the support structures (a); deformation of the part during manufacturing (b); and (c) redistribution of non-sintered powder due to vibration caused by direct contact of the blade with deformed fine parts of the objects during manufacturing (van Zyl et al., 2016)

LPBF involves rapid thermal changes during production. As the laser beam fuses the powder together it keeps moving, allowing atmospheric cooling of the newly fused layer. This thermal gradient induces residual stress within the as-built part from the LPBF process. This is not the only influence on the part, the physical phenomena of the material changing from one phase to another (as it melts and combines) affects the residual stress (Type II), especially in alloys where the phase change adversely affects the amount of stress induced between the lattice structures (Elmer *et al.*, 2005). The solidification theory states that materials with small thermal diffusivity are more likely to result in greater thermal residual stress. Materials with low diffusivity retain greater heat due to a higher specific heat capacity; these materials are also unable to dismiss the heat due to low thermal conductivity. These specific properties lead to greater thermal gradients within components produced by LPBF and consequently large residual stress. For LPBF, the magnitude of tensile residual stress depends on process parameters and the ratio of thermal strain during cooling, to the yield strain in the material.

2.1.2. Advantages and disadvantages of LPBF

When using correct alloys and process parameters, specific material properties could be achieved to solve specific problems (Yadroitsev *et al.*, 2015). "*After melting and subsequent rapid solidification followed by numerous cycles of heating and cooling, the microstructural and* *mechanical properties of the LPBF parts are different from those produced by conventional wrought or cast methods. Post-processing of SLM parts includes polishing, surface hardening and reduction of stresses.*” – (ASTM F2792-12a).

With LPBF technology, it is possible to produce fully dense parts. The advantage is that a complex geometric topology can be produced which enables production of custom once-off components, for example bio-medical implants. LPBF can produce parts within hours and no extra tooling is required; these parts are also high in detail and quality depending on the parameters used. LPBF holds some benefits with respect to other AM and traditional manufacturing technologies namely: low material wastage, wide possibilities in production inputs and virtually net shaped manufacturing of complex functioning parts as seen with the implants in Figure 2.

Despite the huge progress made in recent years in this technology, and its increasing adoption, some production issues remain. Problems in LPBF include careful selection of process parameters and manufacturing strategies for employed powders by different LPBF systems to avoid porosity from incorrect processing parameters or build conditions, surface roughness and cracks, high residual stresses and deformation for processing. Due to these challenges, especially high value and critical parts (such as those for aerospace or medical applications) require process qualification and all parts must be carefully tested.

2.2. Alloying

2.2.1. Introduction into alloying

Metals are rarely used in their pure (unalloyed) form in commercial applications. One or more chemical elements are usually alloyed with a base metal to alter its characteristics in order to meet the desired properties for a specific application. In order to generally improve the properties of materials, and titanium alloys in particular, there are essentially two ways to proceed: alloying and processing (Leyens and Peters, 2003). Although there are many forms of alloying such as plating, cladding, nitriding, ion implantation, carburising and hot dip galvanising (that changes the chemical composition of the surface of a part), in this study the only focus is on the alloying processes that affect the bulk of the material. Table 1 shows some of the characteristics that are affected by alloying (or inoculating).

Table 1. Metal characteristics affected by alloying (Davis, 2001)

Mechanical properties	Processing properties
Room-temperature strength	Castability
Hardenability	Weldability, brazeability and solderability
Fatigue resistance	Formability
Creep resistance	Machinability
Service properties	Physical properties
Heat resistance	Elastic modulus
Toughness and cold resistance	Density
Corrosion/oxidation resistance	Magnetic properties
Hardness and wear resistance	Electrical properties
	Thermal expansion properties
	Colour

The most common reason for alloying is to improve room-temperature strength (Davis, 2001). The strength of a material may be defined as its resistance to permanent deformation (plastic) when loaded beyond its elastic limit. Plastic deformation occurs by the mechanism of slip along the crystallographic planes in the grains of the metal. The objective behind alloying to improve strength is to increase the resistance to crystallographic slip (Figure 22).

The atoms from which a metal part consists are arranged into many individual crystals or grains. The configuration of the crystal lattice and the distance between atoms in the crystal, are the result of the lowest energy state for the atoms in the crystal and are unique to each different metallic element and temperature being considered.

In a metal part, the crystal planes are orientated in many different directions, many of which are not aligned with the direction of the external load. Increasing the resistance to slip in a metal part due to an external force is based on increasing the interference to the slip process, which include: grain refining, cold work, solid-solution hardening, age hardening, dispersion hardening, phase transformation, and duplex-structure strengthening.

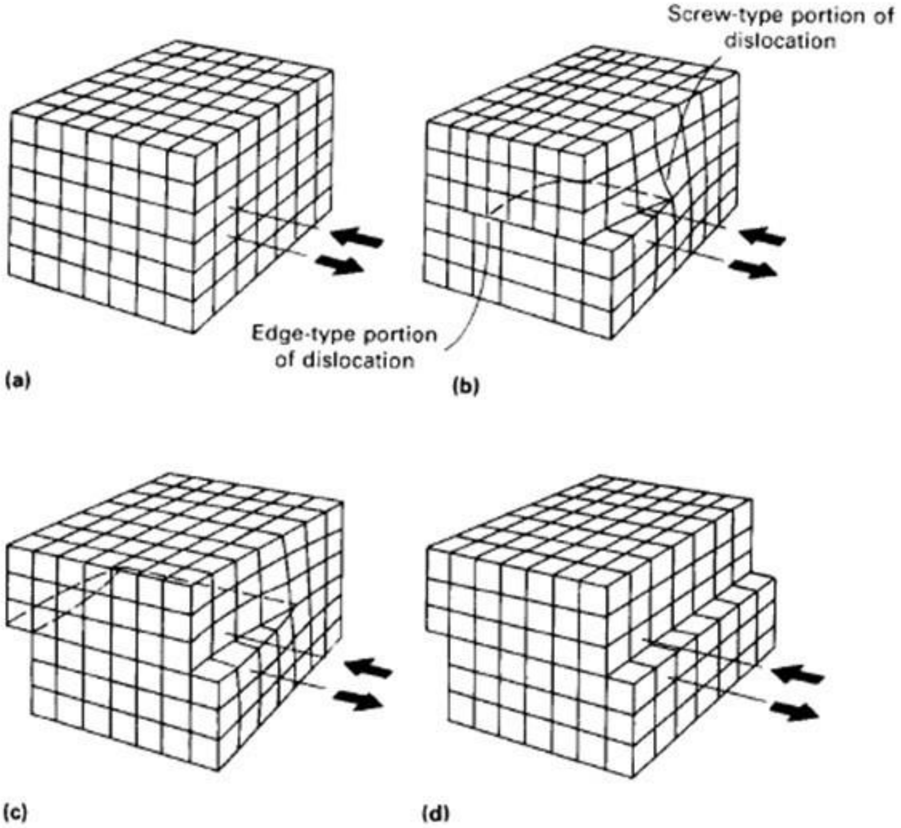

Figure 22. Illustration of the four stages of slip. (a) Crystal before displacement. (b) Crystal after displacement. (c) Complete displacement across part of the crystal. (d) Complete displacement across the entire crystal (Davis, 2001)

Vanadium, aluminium, tungsten, and nitrogen are excellent examples of grain refiners in steel, while vanadium, aluminium, titanium and zirconium additions to low-alloy steels and carbon inhibit grain growth. When a metal is in a molten state and starts to solidify, crystal nuclei first form and then grow together to create grains. The last material to solidify forms the boundaries between the grains. When the amount of added alloying atoms exceeds the limit of solid solubility, the excess atoms of the alloying element become trapped in the grain boundaries. As the temperature is further decreased, the excess atoms attempt to bond with atoms of the base metal to form small regions of intermetallic compound.

Numerous melting and casting techniques have been developed to overcome problems caused by the base metal and the inoculate material having dissimilar properties. When alloying metals with a low melting temperature, such as aluminium and magnesium, elements such as zinc, lead, bismuth and tin are directly stirred into the melted region. Metals with a higher melting temperature, such as manganese, iron, titanium and chromium, are introduced as rich (master) alloys or hardeners, because of their relative delayed melting.

2.2.2. *In-situ* LPBF alloying

Directly manufacturing 3D objects from new alloy materials, using powder mixtures, is one of the additional benefits of LPBF technology. It is a new potential direction in material processing and introduces a wide field for study in LPBF *in-situ* alloying. Influence of process parameters on the microstructure, homogeneity, and properties of Ti6Al4V-10% Mo was studied by Vrancken *et al.* (2014a). LPBF Ti6Al4V-10% Mo alloy was sintered *in-situ* to stabilize the β-phase in the LPBF alloy; a combination of excellent ductility and high strength in this alloy was reported. *In-situ* alloying of TiMo 15wt. % was investigated by Dzogbewu (2017). Sistiaga *et al.*, (2016) mechanically mixed Si powder and Al7075 alloy powder and produced dense crack-free parts by LPBF.

Vora *et al.* demonstrated successful LPBF AlSi12 *in-situ* alloy formation from elemental Al and Si powders. It was noted that the *in-situ* LPBF alloying method could be potentially cost and time effective in developing new materials.

2.3. Titanium alloys

Titanium is a low-density element with high strength possibilities when alloyed with certain elements. Titanium is also nonmagnetic and has good heat-transfer properties. Titanium has the ability to passivate and therefore exhibit a high degree of resistance to attack by most mineral acids and chlorides. Titanium is also non-toxic and generally compatible with biological applications. High strength, stiffness, toughness, low density, and a good corrosion resistance provided by various titanium alloys at low to elevated temperatures, allow for weight saving in aerospace structures and other high-performance applications (Donachie, 2000).

Pure titanium crystallizes at low temperatures in a modified ideally hexagonal close packed structure, called α titanium. At high temperatures the body-centred cubic structure is stable and is referred to as β titanium (Figure 23). The β-transus temperature for pure titanium is 882 ^{0}C ±2.

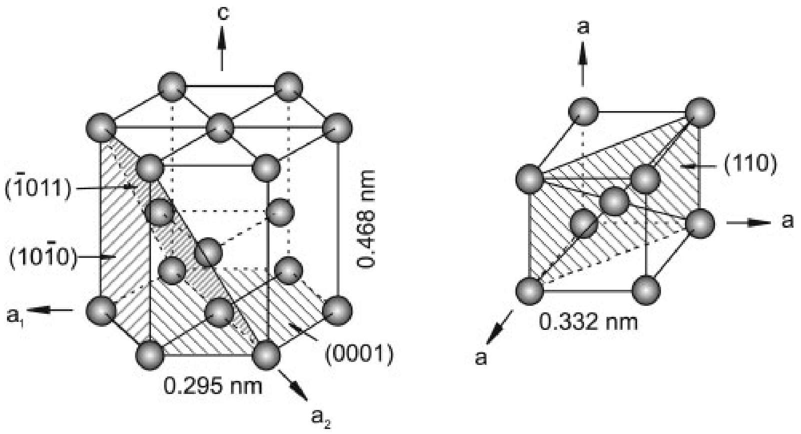

Figure 23. Crystal structure of hcp α and bcc β phase (Leyens and Peters, 2003)

Ways to modify the properties of titanium alloys are indicated in Figure 24.

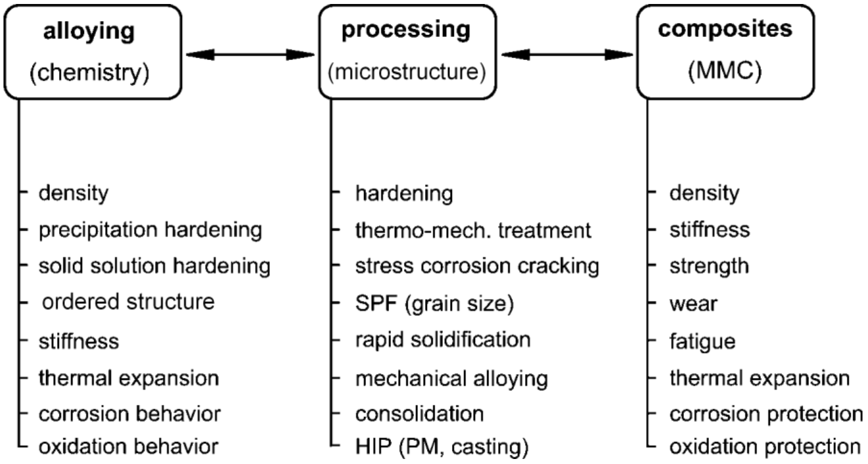

Figure 24. Ways to modify the properties of titanium alloys (Leyens and Peters, 2003)

Titanium alloying elements may be generally classified as alpha stabilizers or beta stabilizers. Materials such as aluminium, oxygen and nitrogen are alpha stabilizers that increase the temperature at which the alpha phase is stable. Beta stabilizers on the other hand, such as vanadium and molybdenum, result in stability of beta phase at lower temperatures (Figure 25). The transformation temperature from alpha-plus-beta or alpha to all beta is recognized as the β-transus temperature. The β-transus temperature is defined as the lowest equilibrium temperature at which the material is 100% beta. The β-transus temperature is critical in deformation processing as well as during heat treatment (Figure 26).

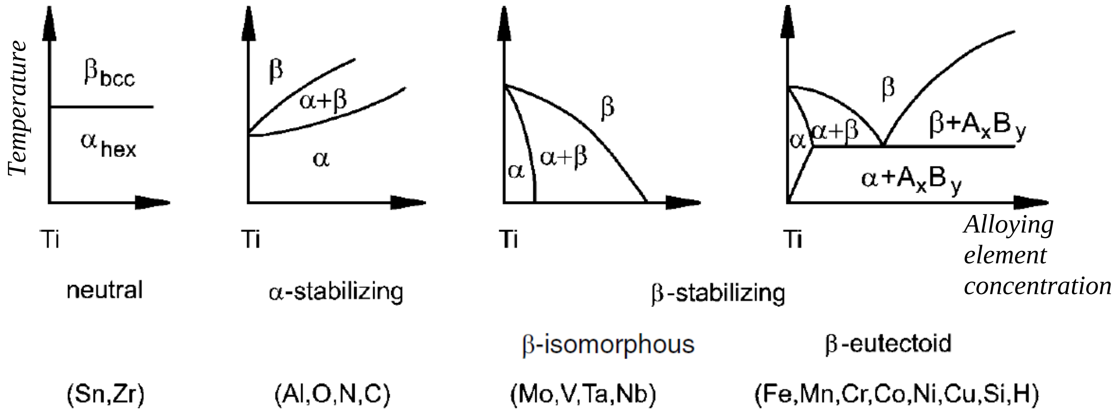

Figure 25. Schematic illustration of the influence of alloying elements on phase diagrams of Ti alloys (Leyens and Peters, 2003)

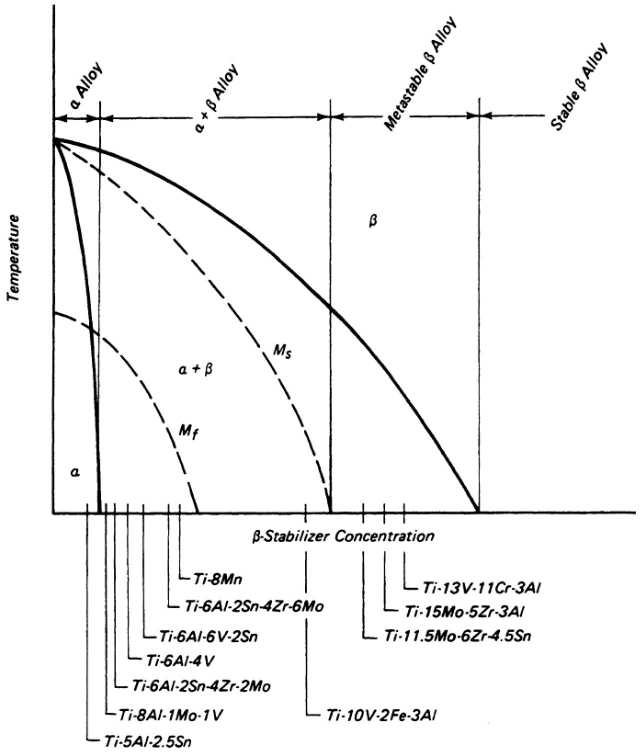

Figure 26. Some U.S. alloy compositions relative to a pseudobinary titanium phase diagram (Donachie, 2000)

The ability of titanium to have two types of crystal structures – body-centred cubic (β-phase) and hexagonal close-packed structure (α-phase) – is the basis for the development of a wide range of titanium alloys with specific characteristics. The chemical composition is modified through alloying additions, heat treatment and processing history to allow for the desired mechanical properties.

Elements with similar atomic radii to that of titanium have the ability to form very good alloys with titanium. All elements which are within the range 0.85–1.15 of the atomic radius of titanium alloy, bonds or combines substitutionally and also have a significant solubility in titanium (Figure 27). Elements with an atomic radius less than 0.59 that of Titanium occupy interstitial sites and also have substantial solubility (e.g. H, N, O, C). The ease with which solutes dissolve in titanium makes it difficult to design precipitation-hardened alloys. Boron has a similar but larger radius than C, O, N and H; it is therefore possible to induce titanium boride precipitation. Copper precipitation is also possible in appropriate alloys (Bhadeshia, 2017).

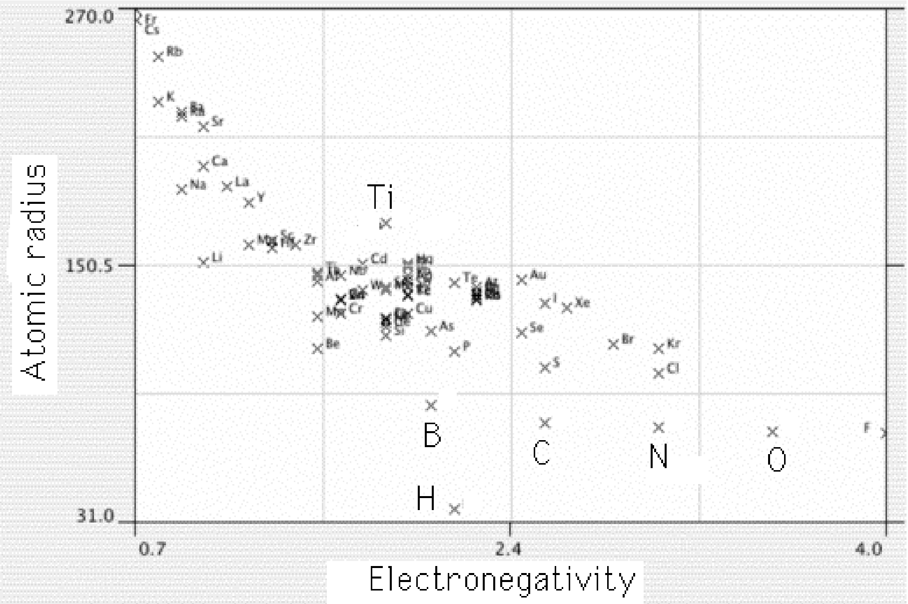

Figure 27. Atomic radius versus Pauling electronegativity for elements (Bhadeshia, 2017)

Currently there are more than 100 titanium alloys, however only 20 to 30 have reached commercial status. Titanium is available in several different grades. Most grades are of alloyed type with various additions of Al, V, Ni, Mo, Cr or Zr. These elements are added to change the mechanical characteristics, heat resistance, conductivity, microstructure, creep, ductility and corrosion resistance properties of pure titanium. Ti6Al4V alloy was developed in the early 1950's for aerospace applications and now it covers more than 50% of usage, pure titanium has application in 20–30% of cases, as indicated by Leyens and Peters (2003).

2.3.1. Conventional Ti6Al4V alloy

Ti6Al4V is one of the most widely used titanium alloys. It is an alpha-beta alloy containing 6 wt% Al and 4 wt% V. Ti6Al4V has a good combination of strength and toughness while exhibiting excellent corrosion resistance properties. The properties of this alloy originate from the refinement of the grains upon cooling and subsequent low-temperature aging to decompose martensite structures formed upon quenching (Donachie, 2000). Ti6Al4V has numerous applications in the aerospace, automotive and marine industries because of its mechanical and corrosive resistant properties. While its superior biocompatibility makes it an excellent biomaterial. Ti6Al4V ELI (Grade 23) is very similar to Ti6Al4V (Grade 5), except that Ti6Al4V ELI contains reduced levels of oxygen, nitrogen, carbon and iron. These lower interstitials improve ductility and increase fracture toughness of the Ti6Al4V ELI material. The improved mechanical properties of extra-low-interstitial grades compared to standard grades of titanium alloys, are mainly the result of reduced oxygen levels (Donachie, 2000).

Generally, Ti6Al4V is used in applications up to 400 °C. It has a density of roughly 4420 kg/m^3, an ultimate tensile strength of about 1 GPa and elastic modulus of 114 GPa (Table 2). By comparison, annealed type 316 stainless steel has a density of 8000 kg/m^3, elastic modulus of 193 GPa, and a tensile strength of only 570 MPa (ASM Aerospace, 2015). Ti6Al4V is an α/β alloy possessing a unique combination of toughness, strength and corrosion resistance, low specific weight and biocompatibility. The mechanical properties, heat treatments, and processing of conventional Ti6Al4V are well documented in standards for biomedical applications (ASTM F1108-14, F1472-08, F136-13, F620-11, ISO20160:2006), Figure 28.

*Table 2. Typical physical and mechanical properties for wrought Titanium Ti6Al4V ELI (Grade 23), annealed at 700-785ºC (Matweb, 2018, Paradis et al., 2006, Lütjering, 2007)**

Property	Typical Value
Density	4420-4430 kg/m^3
Melting Range	1649±15°C
Solidus	1604 °C
Liquidus	1660 °C
Beta transus	999±15°C
Specific heat capacity	526.3 J/kg.°C
Thermal conductivity W/m.K	6.7-7.2
Tensile strength, ultimate	860 MPa
Tensile strength, yield	790 MPa
0.2% Proof. Stress	910 MPa
Elongation at break	15%
Reduction in area	36%
Elastic modulus	114 GPa
Hardness, Vickers	341
Compressive yield strength	860 MPa
Notched tensile strength (Kt, stress concentration factor = 3.5)	1170 MPa
Ultimate bearing strength (e/D=2)	1740 MPa
Bearing yield strength (e/D=2)	1430 MPa
Poisson's ratio	0.342
Charpy impact	24.0 J
Fatigue strength, # of Cycles 1.00e+7, Kt, stress concentration factor= 3.1	140 MPa
Fatigue strength, unnotched, # of Cycles 1.00e+7	300 MPa
Fracture toughness	75 MPa-m½
Shear modulus	44 GPa
Shear Strength	550 MPa
Viscosity in liquid state, 1750-2050 K	4.42 mPa×s
Mean coefficient of thermal expansion, linear, at temperatures	
20.0 - 100 °C	8.60 µm/m-°C
20.0 - 315 °C	9.20 µm/m-°C
20.0 - 650 °C	9.70 µm/m-°C

* Mechanical properties vary with heat treatment

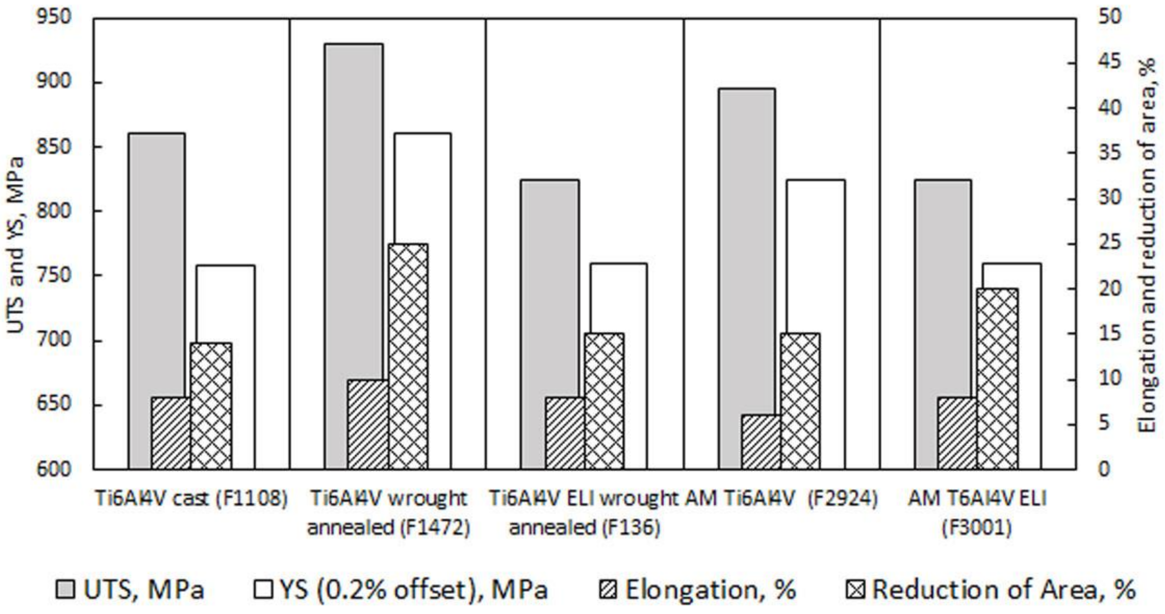

Figure 28. Minimum tensile properties for grade 5 (Ti6Al4V) and grade 23 (Ti6Al4V ELI) alloys in cast, wrought annealed states for surgical implants and material produced LPBF (Yadroitsev et al., 2018)

2.3.2. LPBF Ti6Al4V alloy

The chemical composition requirements for additively manufactured (AM) alloys coincide with those for conventional materials. For wide application in the medical industry, it is crucial that LPBF Ti6Al4V implants comply with international standards regarding their microstructure and mechanical properties. Microstructure plays a vital role in the mechanical properties of an alloy, such as strength, ductility, creep resistance, fracture toughness and crack propagation resistance. As-built LPBF Ti6Al4V samples had a fine α’ martensitic microstructure. High cooling rates at LPBF result in the formation of the acicular/lamellar α’ hexagonal martensitic phase in Ti6Al4V. At cross-sections along the building direction, columnar structures are clearly visible, whilst in the transverse direction, bundles of columnar grains can be seen (Figure 29).

Strongly-textured structures can lead to significant anisotropic mechanical properties, causing different mechanical responses to external loading along different sample orientations. For LPBF Ti6Al4V produced by powder bed fusion, ASTM standards F2924 and F3001-14 assume quite a variable elongation of 6-10%; minimum tensile properties for Ti6Al4V ELI alloy are similar to wrought annealed material for surgical implants (Figure 28). The mechanical properties of samples depend primarily on the chemical composition, processing history and thermal treatment procedures employed (Table 3).

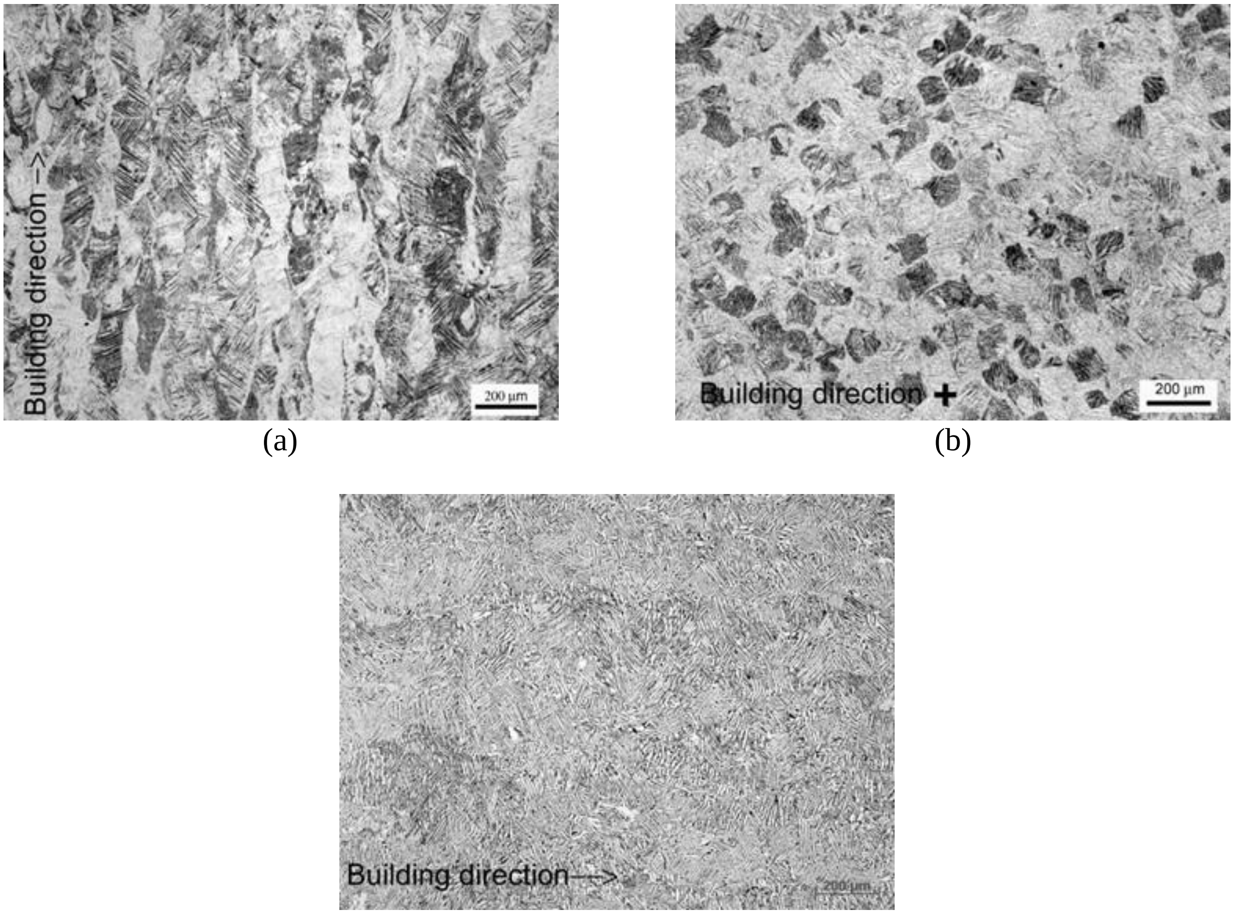

(a) (b)

(c)

Figure 29. Microstructure of horizontal as-built (a) and vertical samples stress relieved at 650℃ (b) annealed at 950℃ (c) (Yadroitsev et al., 2018)

Table 3. Tensile properties of as-built and annealed DMLS horizontal Ti6Al4V samples (Moletsane et al., 2016)

Machine/Process parameters (if indicated)	**UTS, MPa**	**YS, MPa**	**Elastic modulus, GPa**	**Elongation at break, %**	**Density**	**Microstructure**	**Source**
Ti6Al4V alloy							
Experimental machine built at ILT	1140±10	1040±10		8.2±0.3	99.7 ±0.1	acicular α’	Facchini *et al.*, 2010
EOSINT M270 Laser power, 195 W Scanning speed, 0.225 m/s	1095±10	990±5	110±5	8.1±0.3			
EOSINT M270	1248	1043	112	8.5			Frey *et al., 2009*
EOSINT M270	1269±9	1195±19		5±0.5		α’ martensitic laths	Rafi *et al.*, 2013
EOSINT M270	1407	1333		4.54		α’ plates	Murr et al., 2009
EOSINT M280 Standard process parameters for 30 µm powder layer thickness	1155±20			4.1±2	99.79 ±0.2	fine acicular α’ martensite	Becker *et al.*, 2015
After stress-relief heat treatment	1230±20			7.0±2			
MTT SLM 250 Laser power, 175 W, 2 mm FOD Scanning speed, 0.71 m/s Layer thickness, 30 µm Hatch distance, 120 µm	1321±6	1166±6	112	2±0.7	>99.5	α’, no β-phase	Mertens *et al.*, 2014
Annealed 640 °C for 4 hrs	1225±4	1104+8		7.4±1.6		no significant micro-structural change	
Ti6Al4V (ELI)							
Laser power, 250 W Spot size, 52 µm Scanning speed, 1.6 m/s Layer thickness, 30 µm Hatch distance, 60 µm	1267±5	1110±9	109.2±3.1	7.28±1.12	fully dense	acicular α’ martensitic	Vrancken *et al.*, 2012
Heat treatment 3 h at 705 °C, air cooling	1082±34	1026±35	114.6±2.2	9.04± 2.03			
Trumpf LF250 Laser power, 200 W Spot size, 220 µm Scanning speed, 0.5 m/s Layer thickness, 30 µm Hatch distance, 200 µm Preheating 500°C	1206±8	1137±20	105±5	7.6±2		acicular α’ martensitic	Vilaro *et al.*, 2011
Annealing at 730 °C for 2 hrs, air cooling	1046±6	965±16	101±4	9.5±1		needle α’ phase embedded in α+β	
Annealed wrought Ti6Al4V (ELI) ASTM F136-13	Min 825	Min 760		Min 8	Area reduction: Min 14-15%		

Yadroitsev *et al., (*2018) concluded that for EOS recommended process parameters and strategy, Ti6Al4V (ELI) samples measured by micro-CT scans had a density of more than 99.99%. The typical pore size was in the range of 30-200 µm. Micro-CT scans and cross-sectioning microscopic analysis showed that the larger pores were predominantly elongated in shape and can be considered as interlayer pores. LPBF manufacturing led to high residual stress in as-built objects and unique microstructure (van Zyl *et al.*, 2016). Ti6Al4V (ELI) as-built microstructure consists of hexagonal α’ martensitic needles. No beta precipitations were found, in as-built samples neither after heat treatment (stress relief) at 650 ^{0}C for 3 hours. Annealing at 950 ^{0}C for 2 hours decomposed α’ martensite and transformed microstructure to α+β phases mixture with few α phase equiaxial small grains randomly distributed in the volume (Yadroitsev *et al.*, 2018).

As-built samples fabricated in vertical and horizontal directions showed high strength and relatively low ductility (about 10%) caused by the presence of residual stresses and very fine martensitic structure. After stress relief heat treatment, UTS decreased by 6–8% and YTS was unaffected. Annealing led to significant improvement in ductility: elongation of break was increased up to 20%. The modulus of elasticity varied insignificantly and it was in the range of 110-119 GPa (Krakhmalev *et al.*, 2016, Yadroitsev *et al.*, 2018). Vickers microhardness was measured on the as-built and stress-relieved specimens by Moletsane *et al.* (2016). The microhardness for different cross-sections was similar, and the values did not show any statistically significant difference (t-test, $p<0.001$) with reference to the building direction. The HV_{300} average value was 389±14.8 for the as-built samples, and the microhardness was slightly lower (374±17) for the stress-relieved samples. Results of these studies clearly show that if the LPBF process parameters are properly selected, the properties of LPBF parts from Ti6Al4V (ELI) fully meet the requirements for implants.

2.3.3. Copper-bearing titanium alloys

Casting of titanium alloys is complex due to titanium having a high melting point, high reactivity with the mould, affinity with interstitial elements that require melting under controlled atmosphere. Composition and cooling rates are also important in determining the final microstructure. Copper as beta-stabilizing element decrease the melting point. Copper has a Face Centred Cubic (FCC) lattice structure. Typical physical and mechanical properties of pure copper are shown in Table 4.

Pure copper is characterized by a high ductility and electrical and thermal conductivity. It has a wide range of applications in the construction, power generation and transmission, automotive, marine and mold industry, *etc*. The antibacterial properties of copper have made it a metal of choice for frequently touched food and utensil surfaces. Copper occurs in different grades and the amount of impurities present in each type of grade differs however in its purest form it contains $\geq$ 99.3% copper (Harrer, 2016).

Table 4: Typical physical and mechanical properties of pure annealed Cu (Matweb, 2018; Everhart et al., 1975)

Property	
Density, kgm^{-3}	8930
Melting point, ^{o}C	1083
Solidus, ^{o}C	1065
Liquidus, ^{o}C	1086
Specific heat, J·kg^{-1}K^{-1}	385
Thermal conductivity, Wm^{-1}K^{-1}	398
Ultimate tensile strength, MPa	210
Yield strength, MPa	33.3
Elasticity modulus, GPa	110
Shear modulus, GPa	46
Elongation at break, %	60%
Hardness, Vickers	50
Poisson’s ratio	0.343
Mean coefficient of thermal expansion, linear, at temperatures 20.0 - 100 °C 20.0 - 250 °C 20.0 - 500 °C 20.0-925°C	16.4 µm/m-°C 18.5 µm/m-°C 20.2 µm/m-°C 24.8 µm/m-°C

Based on the Ti-Cu phase diagram (Figure 30), eutectoid transformation is close to 7.1% copper and titanium accordingly. Samples processed under low cooling rates would produce microstructures formed by a mixture of Ti$_2$Cu and α-titanium, the volume fraction of each phase depending on composition (Andrade *et al*., 2005). For Ti-Cu alloys, an increase in strength resulted further in additions of copper content, however resulting in a reduction in plasticity, which could lead to an unfavourable workability as well as poor performance in applications (Ma *et al*., 2018).

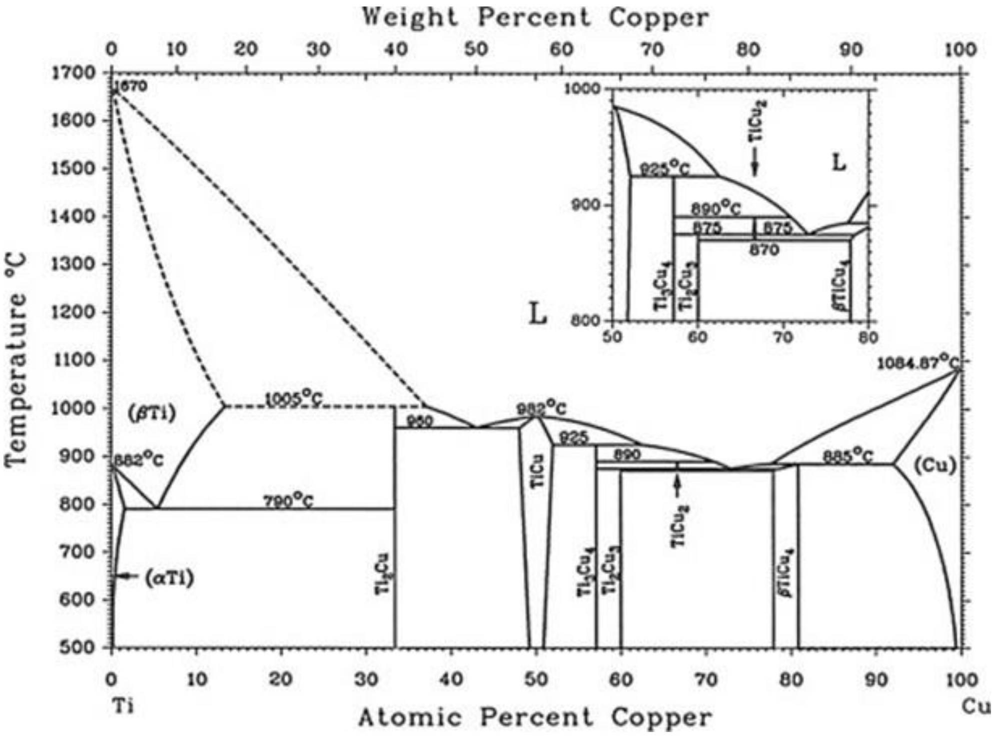

Figure 30. Ti-Cu phase diagrams (Yao et al., 2009; Andrade et al., 2005)

Andrade *et al*. (2005) found that Ti-5.0 % Cu hypoeutectoid sample cast in a copper mould had a cooling rate that was high enough to promote martensitic transformation and suppress Ti_2Cu formation (Figure 31).

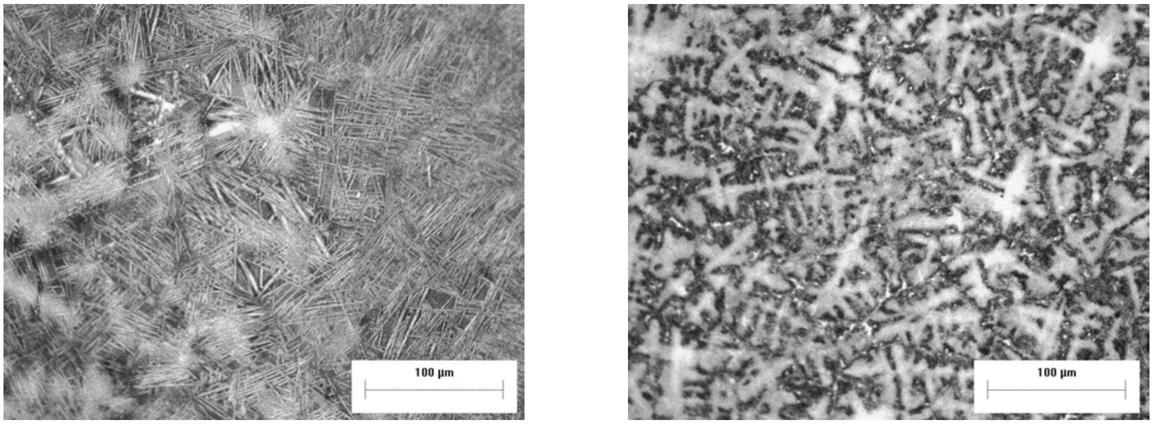

(a) (b)

Figure 31. Optical micrograph of 5% Cu sample showing a martensite structure and (b) 15% Cu sample showing dendritic structure in a martensitic matrix (Andrade et al., 2005)

As the copper content was raised to 15 % (hypereutectoid composition) it was expected to form Ti_2Cu and α phase, but a metastable α′ martensite was formed during the rapid cooling, as can be seen in Figure 31b. The eutectoid structure of the 15% copper sample shows dendritic morphology while Ti_2Cu was precipitated in the interdendritic regions. Vickers hardness in Ti-5% Cu samples was 294±25 and enhanced hardness 384±34 was found for Ti-15% Cu samples by forming intermetallic Ti_2Cu phase (Figure 32).

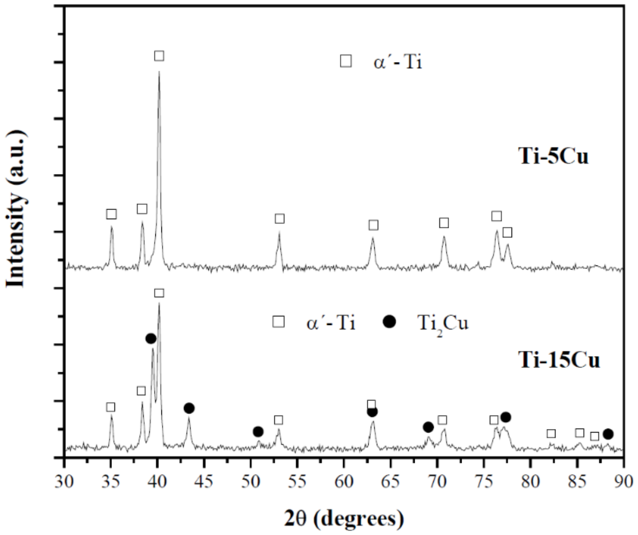

Figure 32. X-Ray diffraction of the Ti-Cu alloys (Andrade et al., 2005)

Erinosho *et al*. (2017) studied laser metal deposition of 3-5% Cu on Ti6Al4V, Ti6Al4V increased hardness to 547±16, and 519±54 respectively against 444±49 of Ti6Al4V powder. Widmanstätten structures were observed in most of the microstructures and their textures are dependent on the process parameters used.

Guo *et al.* (2017) studied properties of LPBF water quenched Ti6Al4V-*x*Cu (x=0, 2, 4, 6wt%) alloys that were prepared from commercial Ti6Al4V and commercial pure copper powders on a SLM machine (Mlab-R, CONCEPTLAER, Germany). Ti_2Cu phase was found at 2% copper added samples. It must be noted that relative diffraction intensity of Ti2Cu phase gradually increased with copper contents and no metallic copper was detected in all *in-situ* alloyed samples, which indicated that copper had melted into the Ti6Al4V alloy for processing (Figure 33). A relatively large degree porosity was observed in the 6% Cu sample (Figure 34). Micropores of 10-20 µm were observed scattered randomly on the matrix of Ti6Al4V-xCu alloys. By EDS (Energy-dispersive X-ray spectroscopy), higher content of copper was detected in β phase than that in α phase.

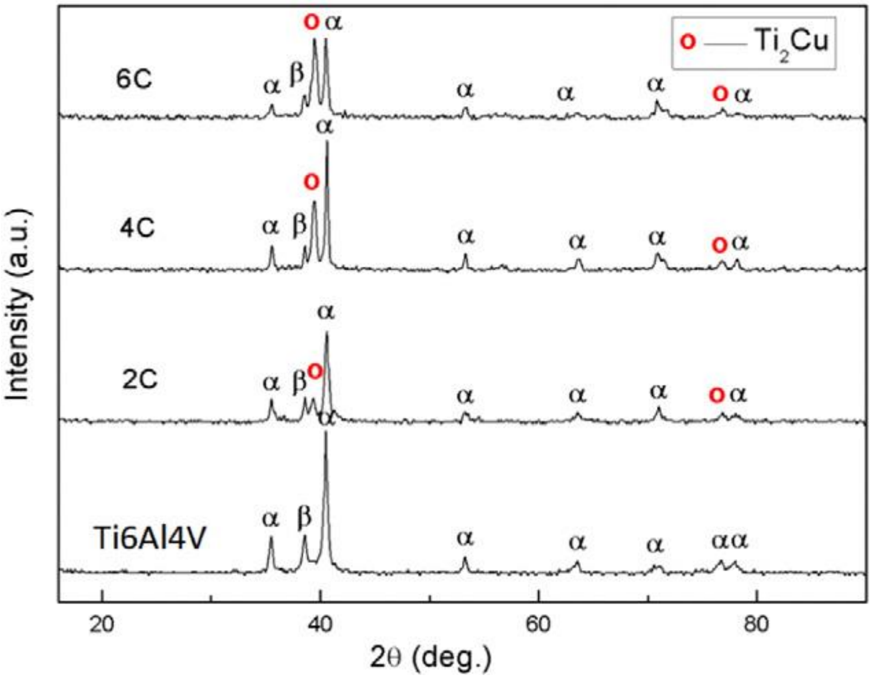

Figure 33. XRD patterns of LPBF Ti6Al4V-xCu alloys (Guo et al., 2017)

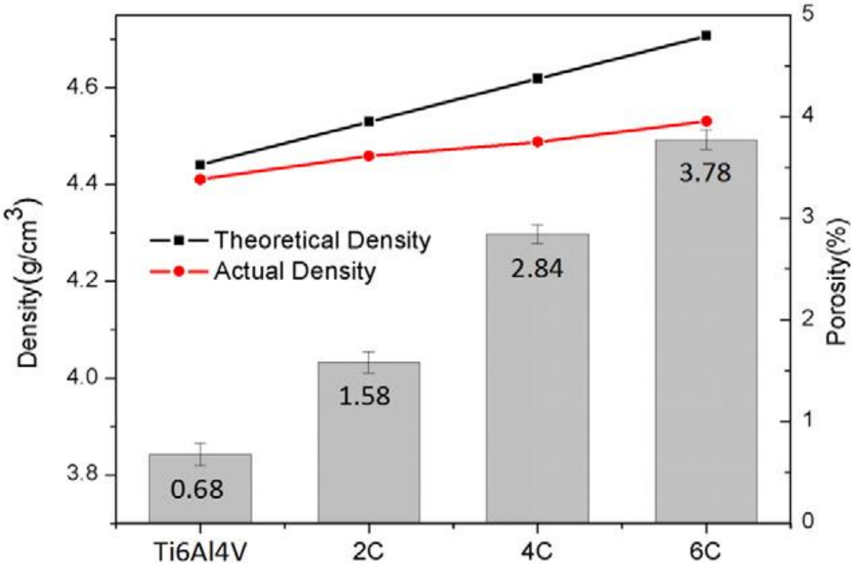

Figure 34. Resulted density of LPBF Ti6Al4V-xCu alloys (Guo et al., 2017)

2.4. Materials for biomedical applications

2.4.1. Bone replacement materials

Failure of medical implants can cause great pain and discomfort to patients, is very expensive to repair and has a poor chance of full recovery. According to Kurtz *et al.* (2009), the total number of hip repair surgeries is expected to increase by 137% and knee repair surgeries by 607% between the years 2005 and 2030. This is determined by the life expectancy of medical implants and by the four main causes of implant failure. These four causes of failure are: infection, loosening of implant, fracture due to external loading or fatigue as well as wear of the interface material which can have toxic effects on the surrounding tissue (Figure 35).

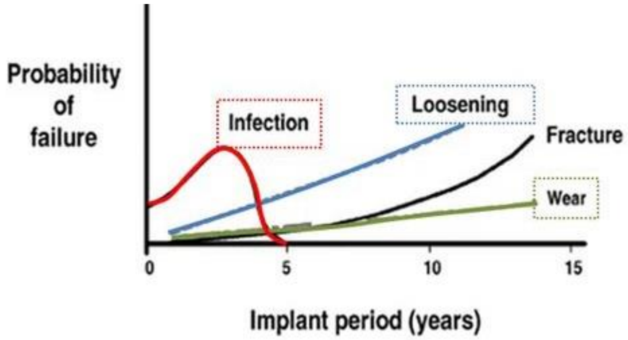

Figure 35. Timeline of implant probable failure (Dumbleton, 1977)

Materials used for orthopaedic implants (especially for load bearing applications) should have excellent biocompatibility, superior corrosion resistance in body environment, a combination of high strength but low modulus mechanical properties, high fatigue and wear resistance, high ductility and should not be toxic to the surrounding tissue. Failure of implants can be reduced by selecting property specific bio-materials. Research continues to improve bio-materials to reduce failure.

Using multiple biocompatible materials on a single medical implant has the opportunity to greatly increase the quality of medical implants. Implants can be constructed to have different mechanical, chemical and physical properties in desired areas of the implant. For example, a bone where the middle section is made from a material with a higher Young's modules and the outer parts from a material with less hardness to improve the functionality of the implant and reduce stress shielding on the bone (Figure 36). Screw connections or weld joints can be avoided when considering the joint connections of different material in current implants.

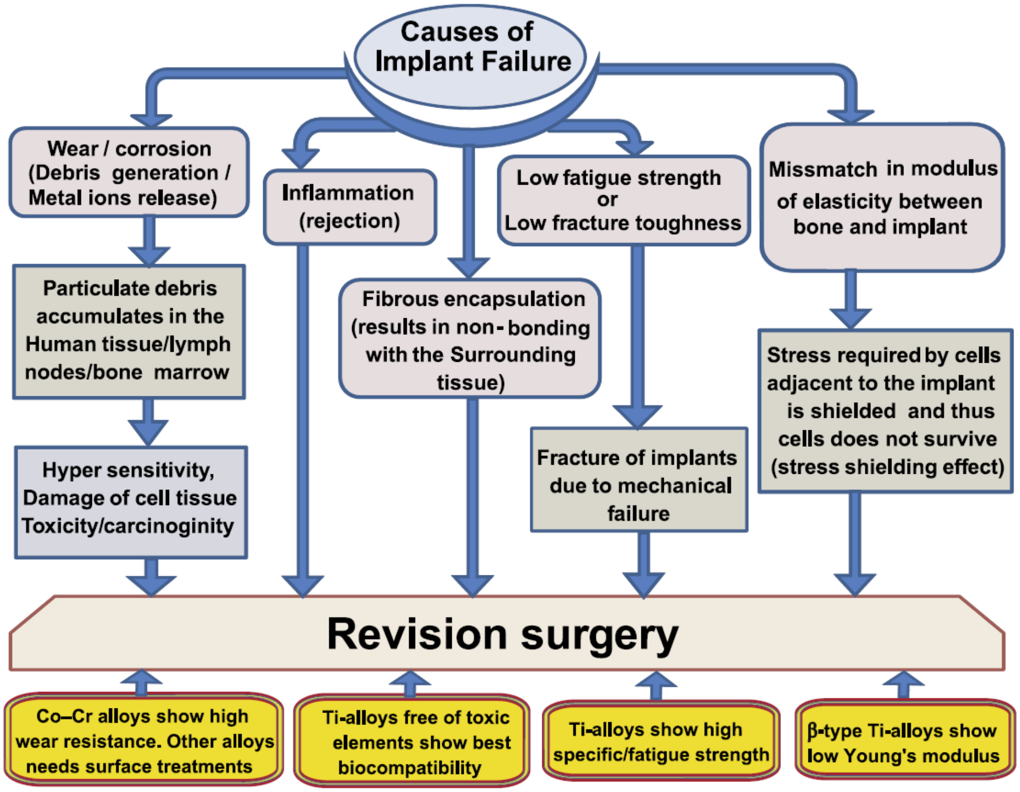

Figure 36. Various causes for failure of implants that leads to revision surgery, footed with a proposed system for better performance (Gepreel and Niiomi, 2013)

Biomedical materials are defined by the National Institutes of Health Consensus Development Conference Statement (1982) as "*any substance or combination of substances, other than drugs, synthetic or natural in origin, which can be used for any period of time, which augments or replaces partially or totally any tissue, organ or function of the body, in order to maintain or improve the quality of life of the individual*". There are three main types of biomaterial namely bio-tolerant materials, bio-active materials and bio-inert materials (Table 5). Bio-tolerant materials refer to a material where the interface between the bone tissue and implant is separated by a fibrous layer of tissue. In other words, surrounding bone forms directly onto the interface surface of the implant. However, bio-inert materials have direct contact with the surrounding bone tissue but there are no chemical reactions between the implant and the tissue (Bergmann & Stumpf, 2013).

Bio-active materials refer to materials where chemical bonds with bone tissue are established, these are materials that stimulate a biological response from the body (Fernandes *et al.*, 2015).

Table 5. Biocompatibility of various biomaterials judged by patterns of osteogenesis (Niinomi, 2003)

Pattern of osteogenesis	Biomaterials	Type
Intervene osteogenesis	Stainless steel, Co–Cr alloy, PMMA	Biotolerant materials
Contact osteogenesis	Pure titanium, titanium alloys, carbon, alumina, zirconia, titania, TiN, Si3N4	Bioinert materials
Bonding osteogenesis	Bioglass, ceravital, tricalcium phosphate, hydroxyapatite, A–W glass ceramic	Bioactive materials

2.4.2. Functionalisation of materials for implants

There are various materials available for the production of biocompatible medical implants. Lodererova *et al.* (2009) produced multi material samples of Ti6A14V and CoCr. Experiments conducted on the mechanical properties and the biocompatibility of the two materials concluded that the materials could be used in medical implants due to their biocompatibility, corrosive and abrasive resistance properties. Habijan *et al.* (2013) conducted experiments with both dense and porous Ni–Ti shape memory alloys (NiTi-SMA) coated with human mesenchymal stem cells (hMSC). NiTi has an elastic modulus (28 GPa) similar to bone (0.3–20 GPa). The study showed that NiTi reduces the stress difference between the bone and the implant decreasing the chance of the implant loosening.

Typical examples of multi-material biomedical implants are dental implants. Implants composing of titanium and hydroxyapatite (HAP) satisfy both the mechanical and biocompatible property requirements of dental implants. Watari *et al.* (1997) studied implants composing of titanium and HAP that were implanted into Wister strain rats. The implant consisted of higher percentages of titanium for the upper part where biting force is directly applied and more HAP for the lower part which is implanted inside the jaw bone to improve biocompatibility and reduce stress shielding (Figure 37). Results showed superior biocompatibility with new bone formation and no inflammation was observed throughout the implantation period. By combining different materials, property specific regions can be formed. The introduction of multi material implants will improve the quality, functionality and life span of biomedical implants.

Loosening of the implant is caused by a mismatch of module of elasticity which leads to stress shielding. Infection at the implant interface, is one of the main reasons for implant failure directly after surgery. Though current use of medication mitigates this, by utilising better biocompatible material and materials having antibacterial properties the chances of rejection can be dramatically lowered. Material selection has a major effect on the life span of the medical implant (Gepreel and Niiomi, 2013).

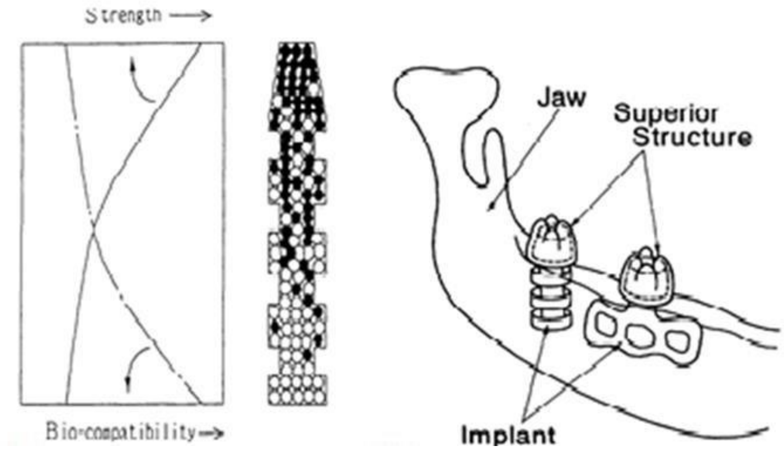

(a) (b)

Figure 37. Dental implants: (a) functionally graded implant properties; (b) dental implant in jaw (Watari et al., 1997)

Metal materials with antibacterial properties, will be beneficial for use as implants to avoid or effectively reduce bacterial infection in the biomedical field. (Ren and Yang, 2017). Surface modification is widely used for various metal implants such as plasma-spray, magnetron sputtering and ion implantation. These modifications are feasible in principle, due to the large difference in properties between the coating (mostly ceramics and polymers) and the metal matrix. However, there are some shortcomings for surface modifications that largely limit their clinical applications, such as loose particles, insufficient antibacterial performance and difficulty in further processing and forming (Ren *et al*., 2011, 2016, 2017).

LPBF technology could join required mechanical properties close to bone and antibacterial performance by introducing lattice structures and antibacterial elements into processed alloys.

2.4.3. Copper-bearing bioactive materials

All living organisms require a complement of essential metal ions, which act as co-factors that enable enzymes to catalyse a wider range of chemical transformations that would not be achievable using solely organic catalysts. Precise metal requirements of organisms vary between individuals, environmental niches, metabolic states and circadian rhythms, and have varied over evolutionary timescales due to changes in geological, marine and atmospheric chemical conditions.

Among the most common essential metals such as: magnesium, manganese, calcium, iron, copper and zinc, copper is one of the least abundant in biology and yet is of crucial importance. Copper plays a central role in two of the most fundamental metabolic pathways on earth; as a co-factor in the electron transfer protein plastocyanin in oxygenic photosynthesis, and in the terminal aerobic respiratory oxidases such as cytochrome *c* oxidase. Copper is used almost exclusively by oxidoreductase enzymes (Andereini *et al*., 2008). The majority of organisms do possess one or more copper efflux protein, suggesting that copper toxicity is a near-universal selection pressure, especially among organisms that live an aerobic lifestyle (Ridge *et al*., 2008).

The antibacterial effect of copper for stainless steel implants was described by Chai *et al.* (2011). Ren *et al.* (2011) and Zhao *et al.* (2017) studied precipitation in 304 and 316 copper-bearing austenitic antibacterial stainless steels. It was found that 316L-Cu SS 316L-Cu stainless steel inhibited formation of bacterial biofilm due to the release of Cu^{2+} ions and highlighted prominent superiority against encrustation in the presence of microorganisms. Xi *et al.* (2017) indicated that generally, the higher the corrosion resistance is, the lower the antibacterial property becomes, and *vice versa*. It was found that higher copper content and aging were two compulsory processes to exert good antibacterial performance of 316L-Cu alloy. The aging enhanced the copper enrichment in a passive film, which could effectively stimulate the copper ions release from the film.

The effect of copper on the antibacterial performance of a solution-annealed steel was shown by Bahmani-Oskooee *et al.* (2017). The formation of a passive oxide film on the surface of solution-annealed steel, prohibited effective copper ions release to the biological environment. Aging treatment disturbs the oxide film and stimulates the release of copper ions. The accumulation of destroyed bacterial matter on the copper surface has an effect on the rate of copper ions release; copper ions incorporates into a bacterium cell, perforates the cell wall and cause the leakage of intracellular materials leading to bacterium death (Figure 38). Metal nanoparticles with a size range of 1–100 nm have shown strong copper ion release and antibacterial properties.

Li *et al.* (2015) reported the performance of an innovative type 304 Cu-bearing stainless steel (304CuSS) against microbes in tap water. The results showed 304CuSS could effectively kill most of the planktonic bacteria (max 95.9% antibacterial rate), and consequently inhibit bacterial biofilms formation on the surface, contributing to the reduction of pathogenic risk to the surrounding environments. A schematic process of adherence of bacteria on samples with/without copper is shown in Figure 39. It was found that copper ions released from the 304CuSS surface produced the antibacterial function and inhibited the growth of the biofilms.

As mentioned above, one of the main postoperative complications is medical device or implant material-associated bacterial infections. Implant-associated infections are closely related to bacterial biofilm formation (Ren and Yang, 2017).

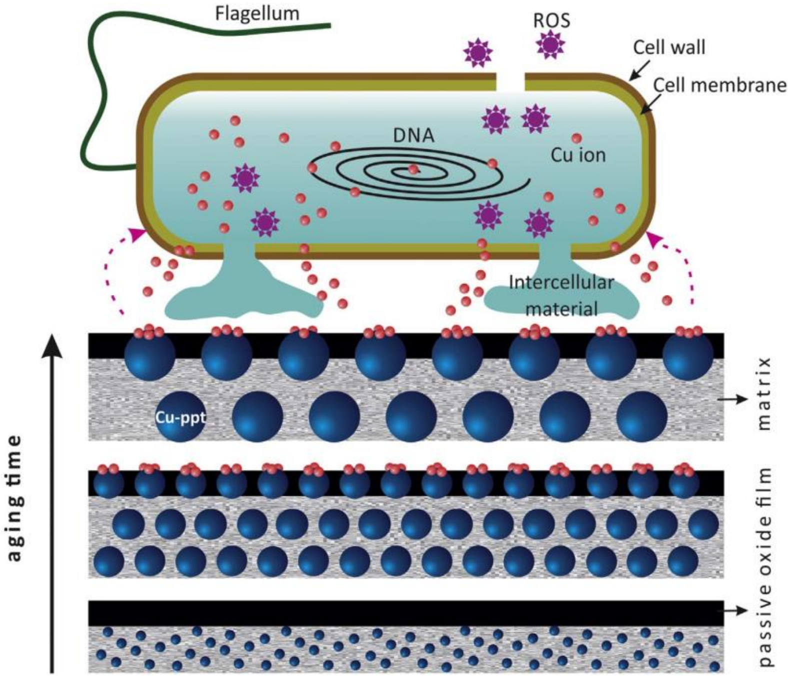

Figure 38. A mechanism adopted for antibacterial performance of the studied, Cu-bearing stainless steels (Bahmani-Oskooee et al., 2017)

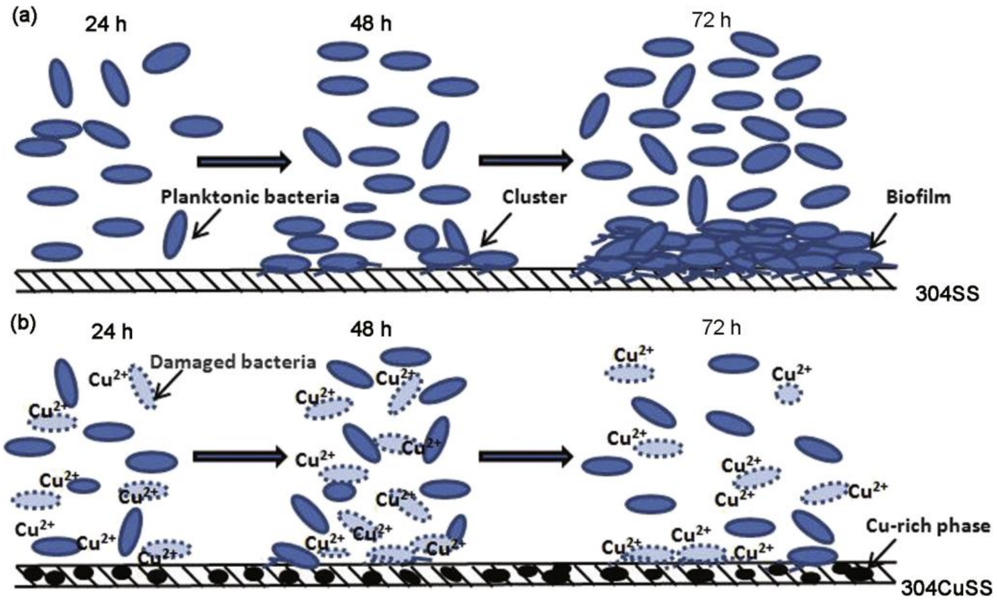

Figure 39. Schematic process of adherence of bacteria on samples: (a) 304SS; (b) 304CuSS (Li et al., 2015)

A study on the antibacterial performance of a copper-bearing medical cobalt-based CoCrWNi alloy was conducted by Wang *et al.* (2014). It was shown that the copper-bearing alloy inhibited the formation of bacterial biofilms on its surface, which is a key factor to reduce the infection. Copper additions slightly increased the corrosion resistance of the investigated alloy, improving antibacterial performance.

Ren *et al.* (2016) fabricated alloyed CoCr-2.8wt.% Cu material for biomedical applications. It was found that this alloy is bactericidal and inhibits biofilm formation. The microstructure, mechanical properties, corrosion resistance and biocompatibility were similar to those of LPBF CoCr alloys.

In titanium alloys, galvanic corrosion between copper-rich phase and titanium matrix, releases copper ions (Liu *et al.*, 2014). Li *et al.* (2016) supposed that released copper ions accumulate in the cell membrane affecting membrane permeability; it disrupts activity of the respiratory chain; Copper ions enter bacterial cells to generate reactive oxygen species (ROS) and disturb the gene replication of *S.aureus* (Figure 40). The antibacterial effect of copper-bearing titanium alloy (Ti-Cu) against *Streptococcus mutans* and *Porphyromonas gingivalis* was studied by Liu *et al.* (2016). The effect may result in enhanced permeability of the membrane allowing entry of copper ions into the cell (Figure 41). The subsequent leakage of intracellular material due to membrane disruption may then cause shrinkage of the cell membrane, ultimately leading to cellular lysis.

Copper disrupts the ROS generation and the respiration of bacteria, and cause genetic toxicity by interfering with the replication genes.

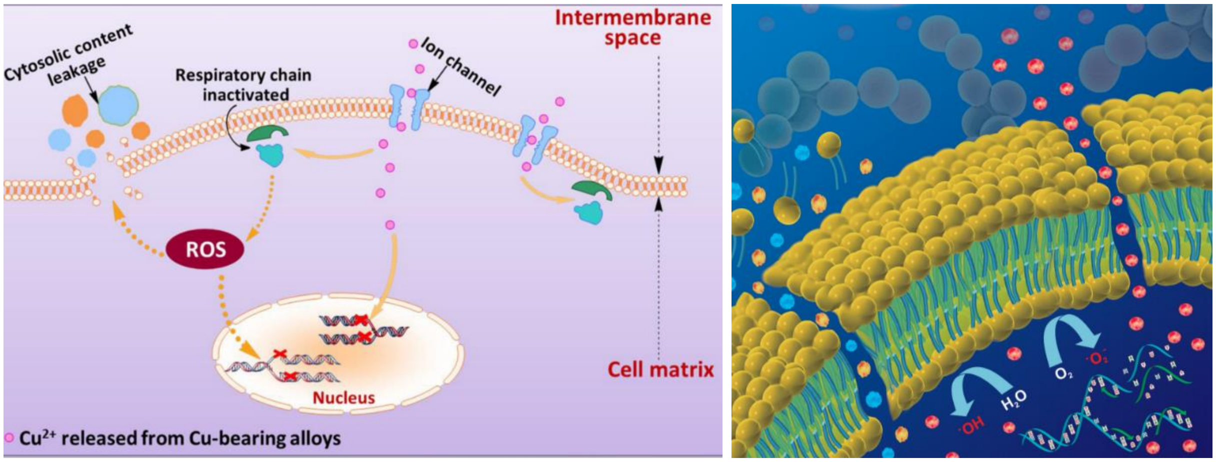

Figure 40. Schematic illustration of possible anti-bacterial mechanisms on the surface of Ti6Al4V5Cu implants (Li et al., 2016)

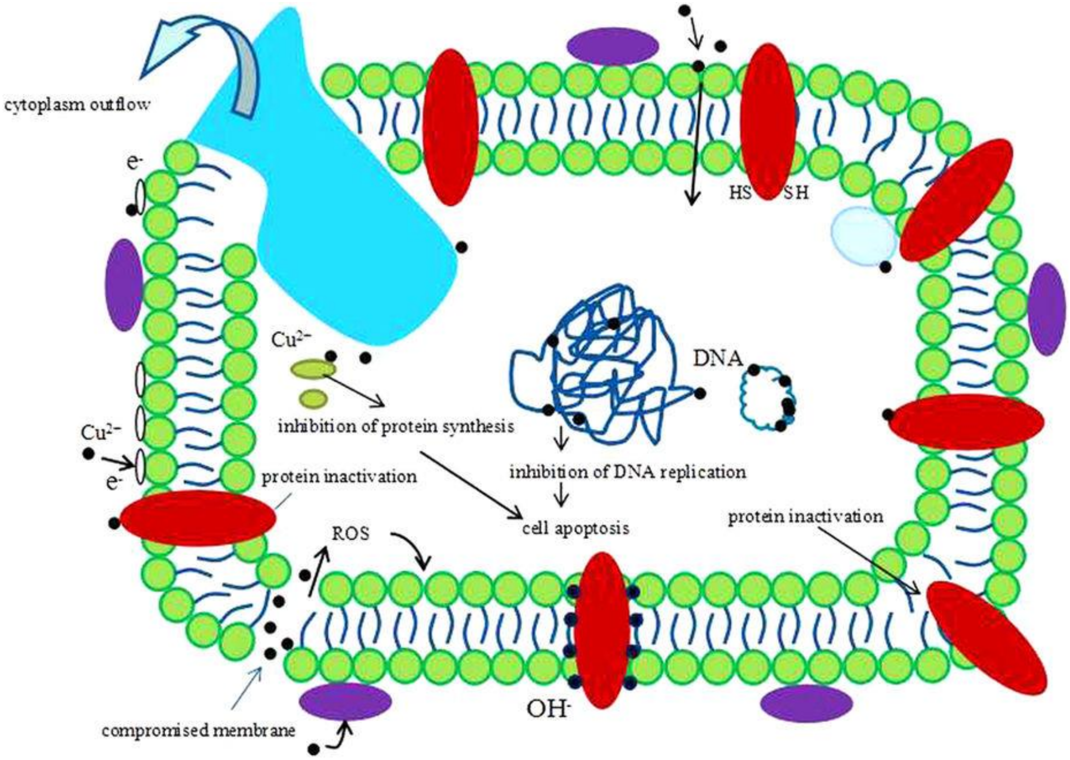

Figure 41. Schematic representation of the hypothetical scenario for the antibacterial mechanism of Cu2+ from Ti-Cu alloy (Liu et al., 2016)

Liu *et al.* (2014) studied Ti–Cu alloys and its antibacterial properties against *E. coli* and *S. aureus*. It was found that the crucial copper content in Ti–Cu alloys should be at least 5 wt.% in order to obtain stable and strong antibacterial activity against these bacteria. Ma *et al.* (2015, 2018), Li *et al.* (2016) presented Ti-645 alloy such as Ti-6.06Al-3.75V-4.85Cu (in wt%) to enhance bactericidal ability of Ti6Al4V alloy.

Guo *et al.* (2017) studied alloyed water quenched LPBF Ti6Al4V-*x*Cu samples and found that LPBF Ti6Al4V alloys with 2, 4, 6 wt.% Cu addition had a much stronger corrosion resistance compared with the Ti6Al4V, especially 4% Cu alloy. Ti6Al4V-*x*Cu alloys also showed good cytocompatibility. Alloys with a higher copper content showed better antibacterial property. Guo *et al.* (2017) found that a copper addition of up to 6 wt% in LPBF Ti6Al4V alloys showed excellent antibacterial property and additionally promoted osteoblast proliferation, differentiation and exhibited a good biocompatibility. Ti6Al4V-*x*Cu alloy can be used also to stimulate osteogenesis. The average daily release amount of Cu^{2+} ions from the Ti-5 wt.% Cu alloy was measured to be $1.584 \times 10-4$ µg/ml (Liu *et al.*, 2016). High Cu dose can cause cytotoxicity according to ISO 10993–5 standard, thus the size of the implant and amount of Cu^{2+} ions has to be taken into account.

2.5. Summary

This chapter presented the literature review on different topics such as the physical phenomena in LPBF process, state of the art review for this technology, advantages and disadvantages and key process parameters in LPBF. Metallurgical background information on traditional alloys and *in-situ* LPBF alloying was presented. It was shown that understanding the physical phenomena in the LPBF process and the materials used is crucial since the final properties of the manufactured LPBF part greatly depend on them.

Titanium alloys have high strength, stiffness, toughness, low density, and good corrosion resistance at low to elevated temperatures. These alloys are commonly used in aircraft applications, biomedicine, power and automotive industry.

With regard to titanium alloying elements, they can be classified as alpha stabilizers or beta stabilizers. Pure titanium and alpha-beta Ti6Al4V alloy are mostly used in biological applications. The microstructure of traditional Ti6Al4V is different to the one obtained in the LPBF as-built condition because of highly localised heat inputs and very short interaction times and local heat transfer conditions for the LPBF process. The original microstructure and mechanical properties of LPBF Ti6Al4V were described in as-built, stress-relieved and annealed conditions. Conventional and LPBF titanium-copper alloys were presented its properties on based on the Ti-Cu phase diagram were done.

Review on materials for biomedical applications, especially for bone replacements and various causes for failure of implants showed that anti-bacterial functionalisation of materials for implants can be done by copper addition since copper in small amounts have no toxic effect on the human body. The antibacterial effect of copper for stainless steels, Co-Cr and titanium alloys was reported in many studies and the mechanism adopted for antibacterial performance of copper-bearing alloys was shown.

Chapter 3: Materials and Methods

This chapter gives a detailed description of the LPBF machine and procedures for manufacturing samples, measuring equipment used during the experimental work, powder materials and the design of experiments for this research.

3.1. Experimental setup

3.1.1. EOSINT M280 system

Samples were manufactured with an EOSINT M280 machine situated and operated at the Centre for Rapid Prototyping and Manufacturing (CRPM) at the Central University of Technology, Free State (Figure 42). The machine comprises of a process chamber with recoating system, elevating system and optical system with laser, a process gas management system, a process computer with process control software, and a set of standard accessories. The machine components are integrated into a robust machine frame. During operation the process chamber is secured with an interlock (EOS, 2018).

Figure 42. EOSINT M 280 machine installed at CRPM, CUT

The optical system creates and positions the laser beam to fuse the powder material. The Ytterbium (Yb) fibre laser emits a beam (1060 - 1100 nm) which is guided by an optical fibre. A laser beam is focused on the base plate with a spot size of about 80 µm and a maximum generated laser power of 400 W. The laser beam is positioned by a scanner. The scanner is a high-speed unit comprising of precision galvanometer scanners with temperature compensation, actively cooled ultra-high reflection mirrors, integrated servo- and interface electronics, digital data transfer from the system's control computer and digital signal processing. The maximum scanning speed is 7 m/s and exposed area is 250 mm x 250 mm. To use small amounts of powder, EOS developed a volume reduction unit or "Small powder volume adaptor kit" where small samples can be produced (Figure 43). A powder layer is deposited with a ceramic blade from the powder platform to the build platform. A laser selectively melts the desired regions of powder on the build platform. By solidifying layers onto each other a 3D part is formed.

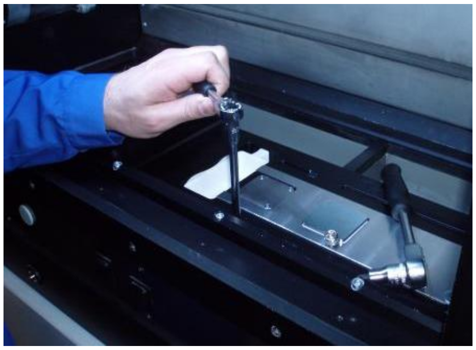

Figure 43. Volume reduction unit installation (Installation_Manual_SPVA.doc, EOS, 2008)

All experiments were conducted on Ti6Al4V 3-mm thick substrates in an argon atmosphere under controlled levels of oxygen (<0.12%).

Preparing the M280 System for manufacturing:

- Clean Ti6Al4V substrate with ethanol
- Install substrate via counter sunk bolts into the M280 build chamber
- Level the platform and substrate using the M280 interface and a feeler gauge
- Ensure recoater blade is damage free
- Deploy powder into hopper (Utilising PPE at all times)
- Compaction of powder
- Level powder
- Ensure recoater arm path over the substrate is collision free (clearance 0.03 mm)
- Install duct in front of building chamber
- Flood chamber with Argon until oxygen content is below 0.01%
- The LPBF process then starts automatically via the EOS interface.

The specimens that were produced were removed from the EOSINT M280 system as one part on the substrate (as-built), the substrate was then cleaned in an ultra-sonic water bath.

3.1.2. Substrate preparation

PROTH Precision surface grinding machine was used for Ti6Al4V substrate preparation (Figure 44).

Figure 44. PROTH grinding machine

Preparing the substrate surface by grinding machine:

- Wipe the machine's magnetic surface with a paper towel
- Clean substrate from any loose particles
- Attach substrate to metal base
- Align substrate on magnetic surface
- Set grinder end-stops to appropriate positions
- Insert appropriate grinding wheel (Andor Hardened, product nr: 11A46J8V86)
- Start grinding wheel
- Start coolant system
- Lower grinding wheel *z*-height to touch substrate
- Activate automatic *x*-movement
- Lower *z*-height in increments of 0.05 mm until substrate has a level surface.

3.1.3. Separating part from substrate

Wire cutting machine by Jiangsu Fangzheng computer numerical control (CNC) Machine Tool Co., Ltd. (Figure 45) was used for templates and separation of parts from the substrate. This process is also known as electrical discharge machining (EDM). Material is removed from the work piece by a series of rapidly recurring current discharges between two electrodes, separated by a dielectric liquid and subject to an electric voltage. One of the electrodes is the tool-electrode, while the other is the workpiece-electrode. The process depends upon the tool and work piece not making actual contact. Separating the samples from the substrate steps:

- Align substrate in EDM machine
- Load desired program
- Move wire to cut start position
- Set machine parameters
- Start cut between substrate and samples

Figure 45. Electrical discharge machine

3.1.4. Powder preparation

The elemental Ti6Al4V and copper powders were sieved using a 45 µm sieve on a vibrating bed (Figure 46) for 5 minutes or until all powder had been sieved.

Figure 46. Sieving system for powders

To produce the Ti6Al4V-1, 3 and 5 at.% Cu powder mixture, the elemental copper and Ti6Al4V(ELI) powders were mixed for 1 hour. Before laser processing, the powder mixture was dried at 80°C for 2 hours without a protective atmosphere, to increase powder flowability. The powder mixture was also kept in a metal container, to reduce static charge build-up between powder particles.

3.2. Analytical equipment

3.2.1. SmartZoom 5 and Axiovision microscopes

Top view images and cross-sectional analysis of sintered tracks, layers and 3D samples were done using an Axiovision optical and SmartZoom 5 microscopes (Figure 47). 3D reconstructions of single tracks and surfaces were carried out using the SmartZoom 5 digital microscope.

(a) (b)

Figure 47. SmartZoom 5 (a) and Axiovision (b) microscopes

For each set of process parameters, three tracks were analysed from the top view. Twelve track width measurements were recorded for each process parameter. Then the plate with tracks was cross-sectioned and 9 cross-sections for each set of process parameters were studied, *i.e.* average width of the tracks had 21 values, and for penetration depth 9 values had been taken into account. The measured depth was divided by half of the track width to find critical values for the keyhole mode (Eagar and Tsai, 1983, Yang *et al.*, 2016). For analysis of the track and surface texture, 3D reconstruction was then done with a digital Smartzoom microscope.

3.2.2. Surface roughness testing

The surface roughness of the LPBF layers was measured with a Surftest SJ-210 portable surface roughness tester from Mitutoyo Corp. (Figure 48a) perpendicular to laser scanning direction. ISO 1997 was used. Rz that is the ten-point height was used for roughness characterisaion. *Rz* is the average absolute value of the five highest peaks and the five lowest valleys over the evaluation length (Figure 48). Cut-off filter (evaluation length) was λc = 0.8 mm, optical length was 3 mm for surface roughness measurements. *Rz* was used for roughness analysis which is the average absolute value of the five highest peaks and the five lowest valleys over the evaluation length (Zygo, 2018).

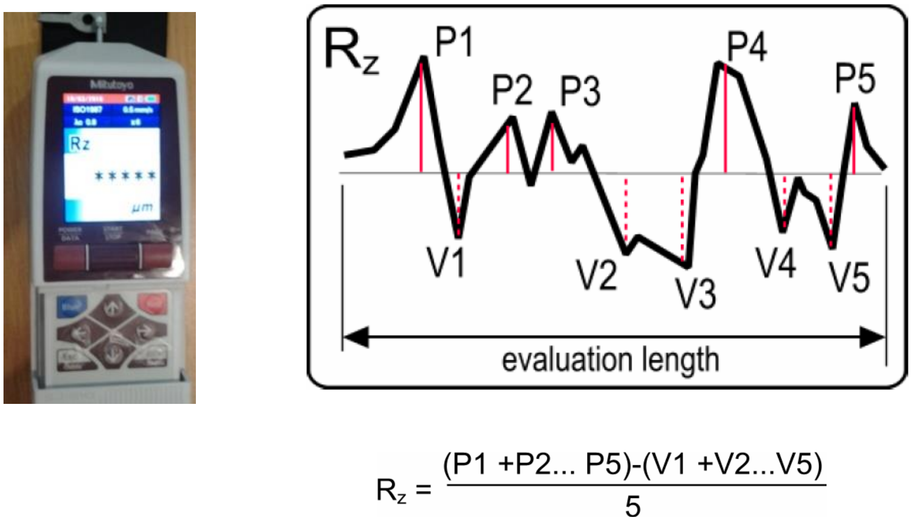

(a) (b)

Figure 48. Surface roughness measuring tester SJ-210 (a) Rz for the profile data (b) (Zygo, 2018)

3.2.3. Metallographic and microstructure analysis

Samples were cut to fit into the compaction machine by the EDM machine for cross-sectional and microstructure analysis. The small templates were incorporated into MultiFast, ClaroFast or Polyfast resins by a CitoPress (Figure 49a). Samples were polished with Tegramine-25 system (Figure 49b) as recommended by Taylor & Weidmann (2016) and etched by Kroll’s reagent consisting of 100 ml water, 1 ml hydrofluoric acid and 2 ml nitric acid.

The porosity and microstructure of cross-sections was studied by optical and scanning electron microscopes (SEM). SEM analysis was carried out at Karlstad University (Sweden) with LEO 1350 FEG operated at 20 kV and at CUT with Phenom Pharos Desktop system operated at 15 kV.

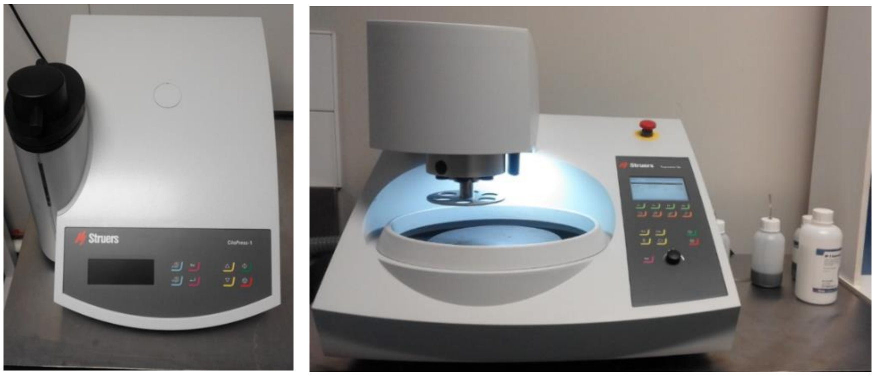
(a) (b)

Figure 49. CitoPress-1 (a) and polishing Tegramin-25 (b) machines

3.2.4. Micro computed tomography

X-ray micro computed tomography (microCT) was used in this study to analyze porosity in 3D samples. The phoenix v|tome| xL240 is a micro-CT scanner manufactured by General Electric (Wunstorff, Germany). It contains two X-ray tubes; one with a reflection-type target and the other with transmission-type target, with a diamond window which increases X-ray emission.

X-ray microCT is a quantitative analysis tool very applicable to additive manufactured parts (du Plessis *et al.*, 2018a). The method allows accurate measurement of porosity in 3D metal coupon samples: as shown in a recent round robin study this can assist in identifying various process parameter errors (du Plessis and le Roux, 2018). In this study, coupon samples of 10 x 10 x 4 mm were used. MicroCT was performed at the Stellenbosch CT facility (du Plessis *et al.*, 2016) using settings as reported in the standard method for 10 mm cubes of Ti6Al4V (du Plessis *et al.*, 2018b), with slight modification. Due to the higher density of Cu-alloyed Ti6Al4V compared to Ti6Al4V, some beam hardening artefacts were present around the edges of images, which required cropping of the middle of each sample rather than analysis of the whole sample – in this case a central region of 6 x 6 x 2 mm was used in each sample and the porosity analysis reported for this section.

3.3. Employed Powders

For LPBF, powder material pre-deposited on the base plate is sintered (fused) by scanning laser beam. The quality of parts strongly depends on homogeneity of the powder layer in terms of chemical and levelled characteristics. The powder properties such as size, morphology, surface area, porosity and impurity content can have a direct effect on the manufacturing process and final properties of LPBF parts (Yadroitsev, 2009; Sun, 2013). Benson & Snyders (2015) indicated that the major powder parameters that should be taken into consideration when characterizing a metallic powder for AM are particle size distribution and shapes, porosity and density, packing density and rheological properties, chemical composition, *etc*.

Argon atomized Ti6Al4V (ELI) and copper powders, spherical in shape were used. The chemical composition for Ti6Al4V (ELI) being 89.26 wt% of Ti, 6.31 wt% of Al, 4.09 wt% of V, 0.12% of O, and copper powder 99.9 % purity. The 10th, 50th and 90th percentiles of equivalent diameter (weighted by volume) were respectively 12.6 µm, 22.9 µm, 37.0 µm for Ti6Al4V (ELI) powder and 9.45 µm, 21.9 µm and 37.5 µm for copper powder (Figure 50).

Table 6: Chemical composition of Ti6Al4V (ELI) powder (in weight %)

Ti		Al	V	O	N	H	Fe	C
	ASTM standard for Ti6Al4V (ELI) alloy, grade 23							
88.1 - 91		5.5-6.5	3.5-4.5	≤0.13	≤0.030	≤0.0125	≤0.25	≤0.080
	Employed powder							
89.263		6.31	4.09	0.12	0.009	0.003	0.20	0.005

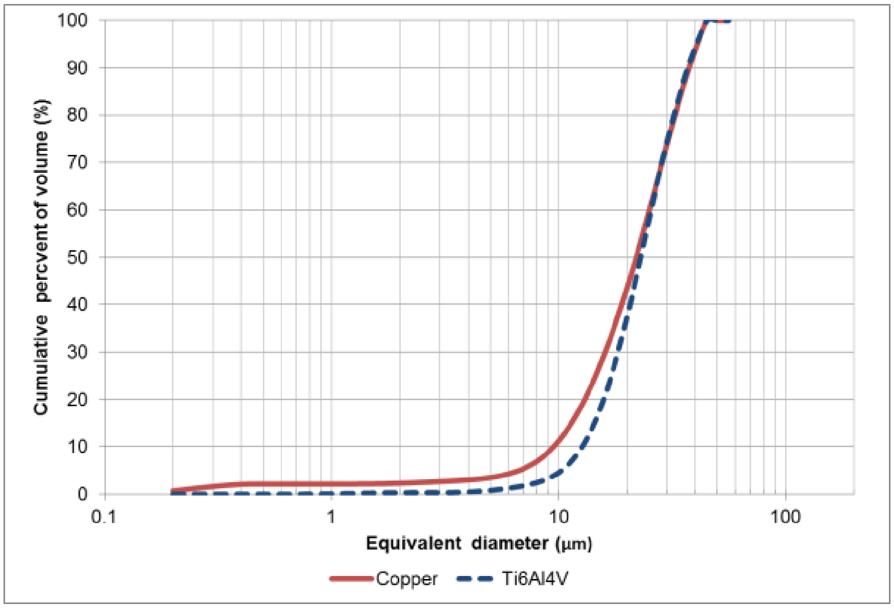

Figure 50. Particle size distributions for employed Ti6Al4V ELI and Cu powders

The employed Ti6Al4V (ELI) powder fulfils the ASTM F1472 requirement of the maximum concentration of impurities (Table 6). The morphology of the gas atomized Ti6Al4V is represented in Figure 51a. The copper powder was spherical in shape (Figure 51b). It must be noted that the two powders (Ti6Al4V ELI and pure copper) were almost similar in particle size distribution (Figure 50).

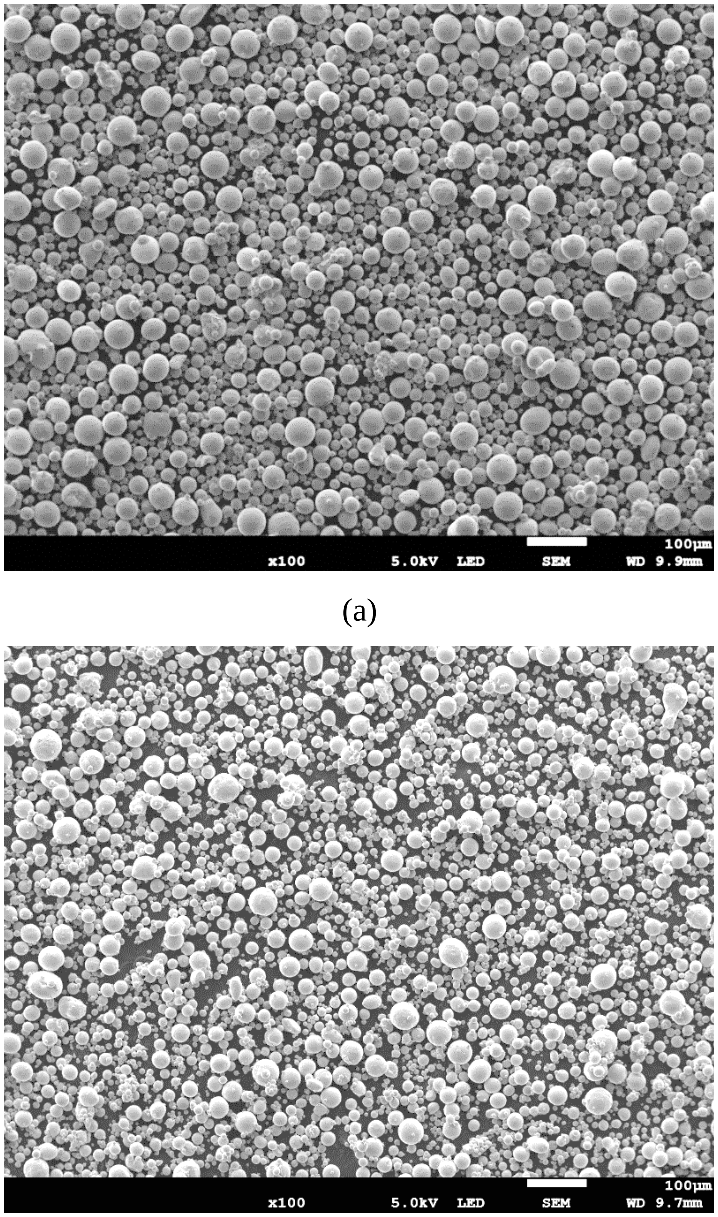

(a)

(b)

Figure 51. SEM micrograph of the employed Ti6Al4V (a) and pure Cu (b) powders

To produce the Ti6Al4V-1, 3 and 5 at.% Cu powder mixture, the elemental copper and Ti6Al4V(ELI) powders were mixed and analysed (Figure 52). Kinnear (2016) showed that these powders have good/excellent flowability and are suitable for the LPBF process.

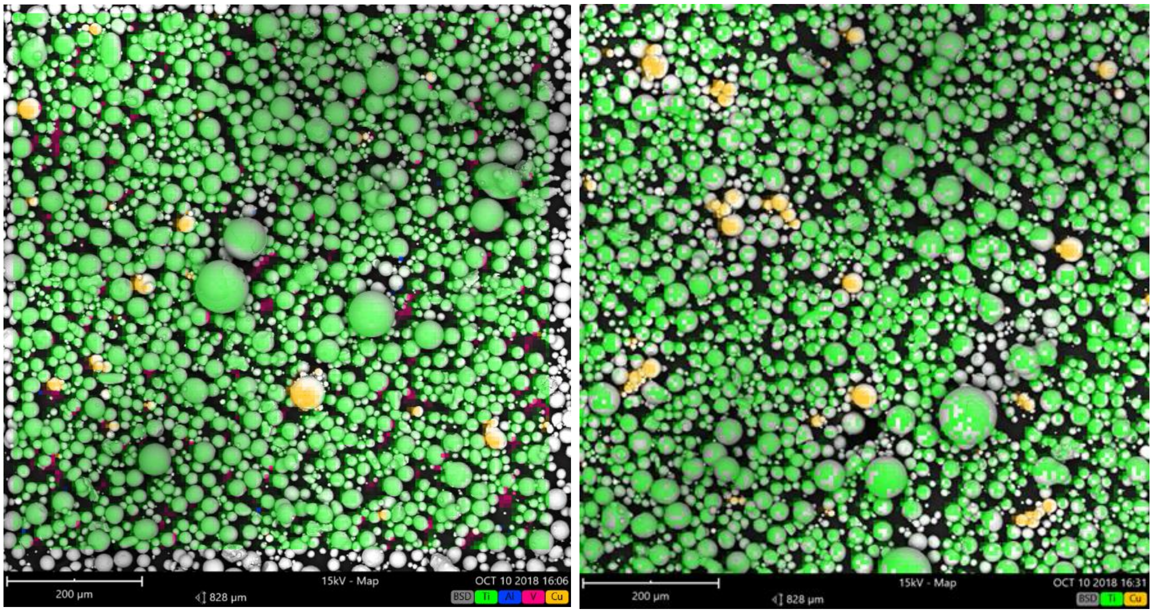

(a)

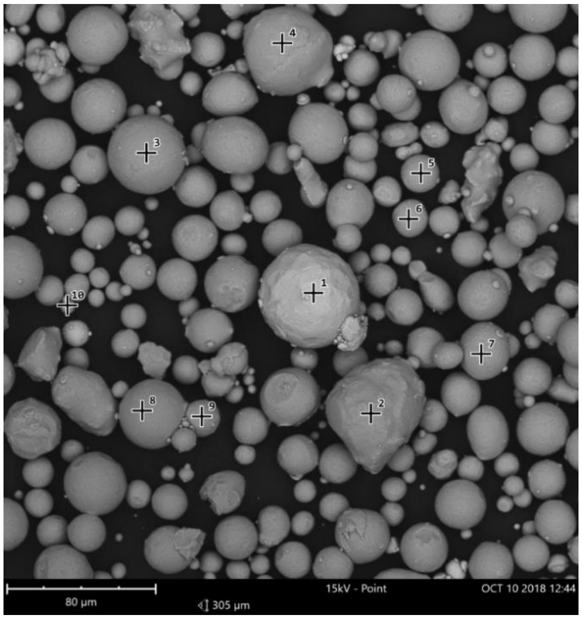

#	Cu	Ti	Al	V
1	95.42	3.55	0.82	0.2
2	-	86.99	9.11	3.91
3	-	85.58	10.28	4.14
4	0.15	90.68	4.23	4.95
5	-	88.86	7.82	3.32
6	-	91.93	5.4	2.67
7		87.5	8.72	3.79
8	-	83.41	12.93	3.66
9	-	83.56	12.48	3.95
10	0.32	88.19	10.47	1.02

(b)

Figure 52. SEM elemental map of the employed Ti6Al4V- 3 at.% Cu (a) mixture where Cu particles are yellow and (b) spectrum of powder mixture (at. %)

3.4. Design of experiments

3.4.1. Experiments with Ti6Al4V–1 at.% Cu

Preliminary experiments with single tracks from powder mixture Ti6Al4V ELI–1 at.% Cu were manufactured. Each set of scanning speeds (0.4–1.8 m/s) consisted of 3 tracks 20 mm in length and 1mm between the tracks (Figure 53). The top view and cross-sections were analysed to estimate optimal parameters for single layer and non-porous 3D samples. The influence of single scanning/rescanning strategies on surface morphology was analysed at scanning speeds of 0.4–0.6–0.7–1.0–1.3 m/s and hatch distance 80 µm. Rectangular samples 5 x 10 mm were produced and analysed.

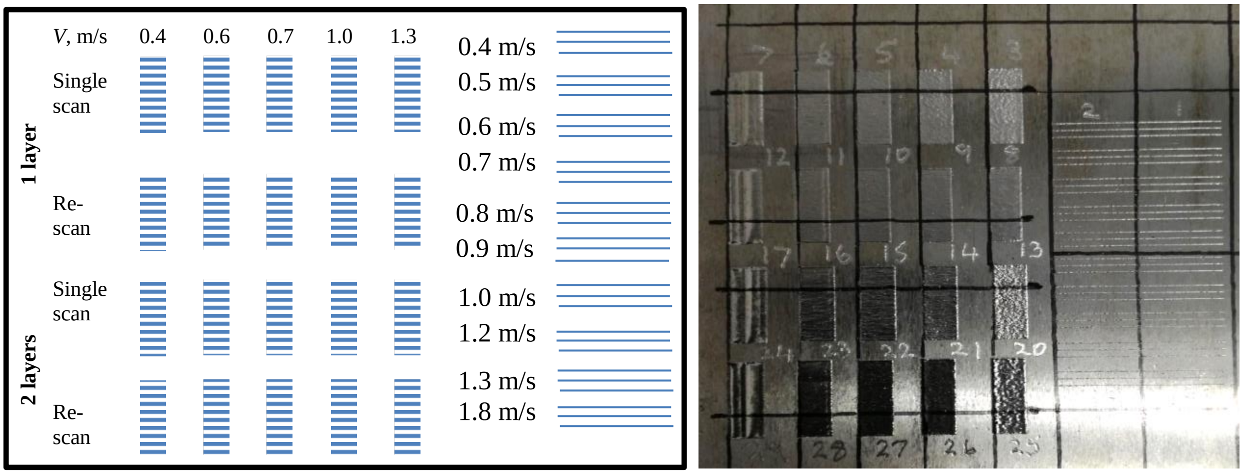

(a) (b)

Figure 53. Schematics for experiments (a) and plate with tracks and layers (b) at Ti6Al4V–1 at.% Cu experiments

3.4.2. Experiments with Ti6Al4V–3 at.% and 5 at.% Cu

To determine optimal laser power and scanning speeds, single tracks with length of 20 mm with space of 1 mm were manufactured. A total of 3 tracks were produced for each set of the following process parameters: 170 W laser power at 0.4–1.4 m/s scanning speeds and 340 W laser power at double the scanning speeds (Figure 54). The powder layer thickness was approximately 50 µm for single tracks and single layers. 10 layers samples of size 5 mm x 5 mm were produced at 30 µm powder layer thickness.

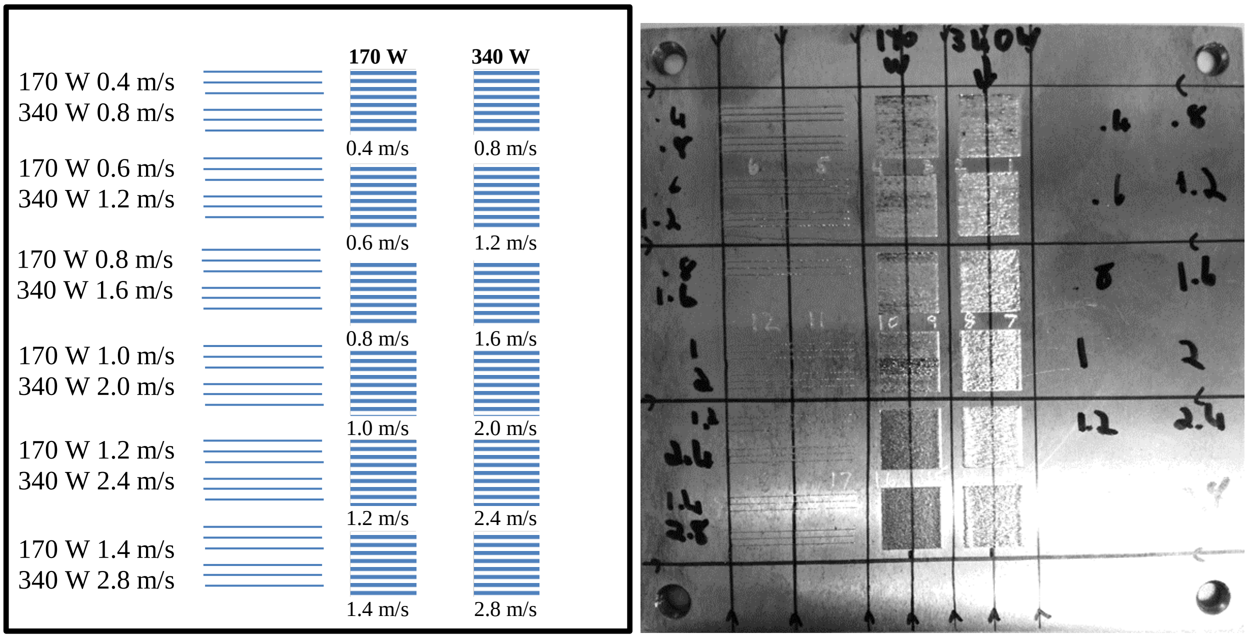

(a) (b)

Figure 54. Schematic for experiments (a) and plate with tracks and single layers (b) Ti6Al4V–3 at.% Cu

For single layer experiments, scanning was done without stripes, only zig-zag scanning as schematically showed in Figure 14. 3D samples have been built with 5 mm stripes and rotational scanning direction of 66.7 degrees from layer to layer to decrease total residual stress and to achieve dense non-porous samples.

Summary

In this chapter, the materials and the framework, outlining the methods employed in the study, were presented. The powder materials used were gas-atomised Ti6Al4V ELI and pure copper supplied by TLS Technik GmbH & Co. Spezialpulver KG. Powder particles had high sphericity that was illustrated with SEM images and had similar sizes. The 10th, 50th and 90th percentiles of equivalent diameter (weighted by volume) were 12.6 µm, 22.9 µm, 37.0 µm for Ti6Al4V (ELI) powder and 9.45 µm, 21.9 µm and 37.5 µm for copper powder, respectively. The EOSINT M280 system, which was used to conduct the experiments, was also described briefly. The equipment used to analyse the results was also shown. This equipment includes the wire cutting machine which was used to section the substrates into templates, an automatic mounting machine used to mount the samples, a semi-automatic grinding and polishing machine, an optical microscope used to reveal the molten pool and measure dimensions, and a roughness meter to measure surface roughness. The design of all the experiments were also described.

Chapter 4. Results and discussion

4.1. Ti6Al4V- 1at.% Cu *in-situ* alloying

4.1.1. Ti6Al4V- 1at.% Cu single tracks

At 170 W laser power and 1% copper, balling effect started at 1.8 m/s scanning speeds and higher. For scanning speeds lower than 1.0 m/s the tracks are fully continuous and stable with no signs of irregularity. At 1.2-1.3 m/s the tracks were also stable, but a humping effect was observed (Yadroitsava *et al.*, 2015). At a higher scanning speed (1.8 m/s), a pronounced humping effect as initiation of balling effect was found (Figure 55).

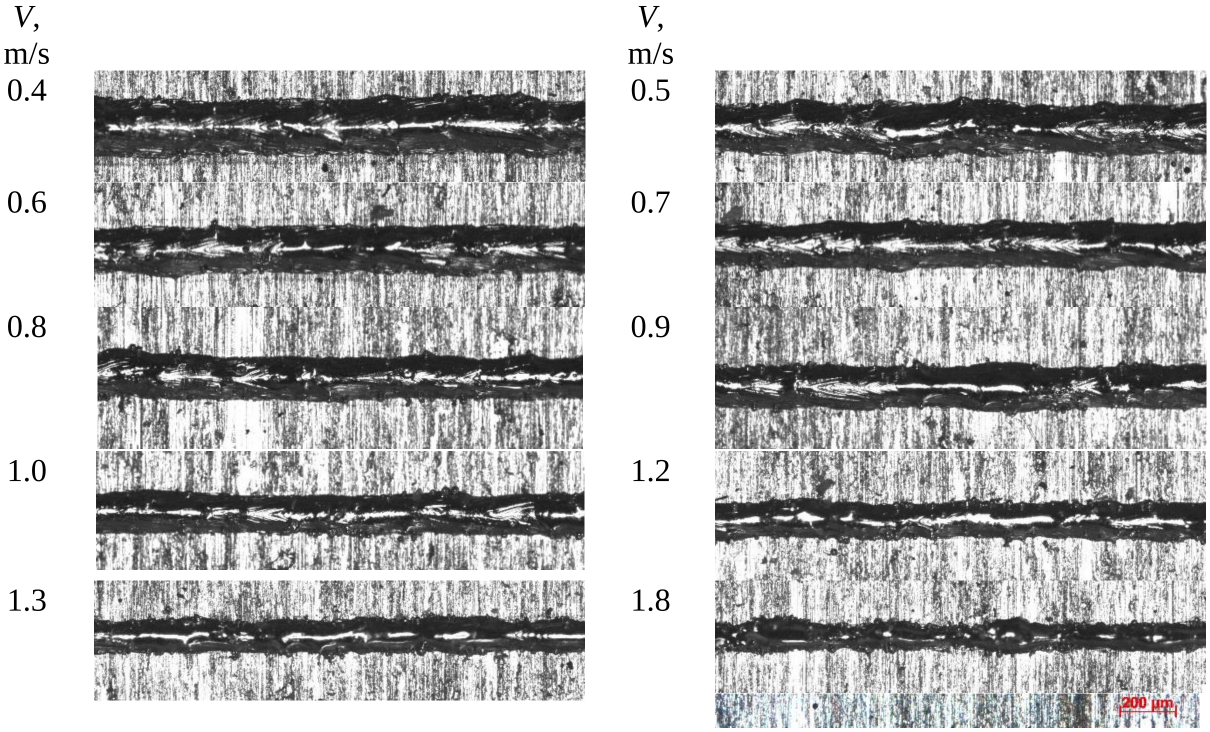

Figure 55. Ti6Al4V- 1at.% Cu single tracks at 170 W laser power at different scanning speeds

Analysis of the width of single tracks shows that addition of 1 at.% Cu did not have an influence on the average width of the tracks (Figure 56). When balling effect started (Tolochko *et al*., 2004), the width of the racks varied greatly. For Ti6Al4V powder, Els (2014) also found that at 45-50 µm layer thickness, irregularities in tracks began from 1.2 m/s. At low scanning speed (0.4 m/s), tracks had satellites (Figure 57) and the width was not stable because excessive energy input caused irregularities of LPBF tracks (Yadroitsev, 2009; Els, 2014; Yadroitsava *et al.*, 2015). Analysis of cross-sections showed keyhole effect at this scanning speed (Figure 58).

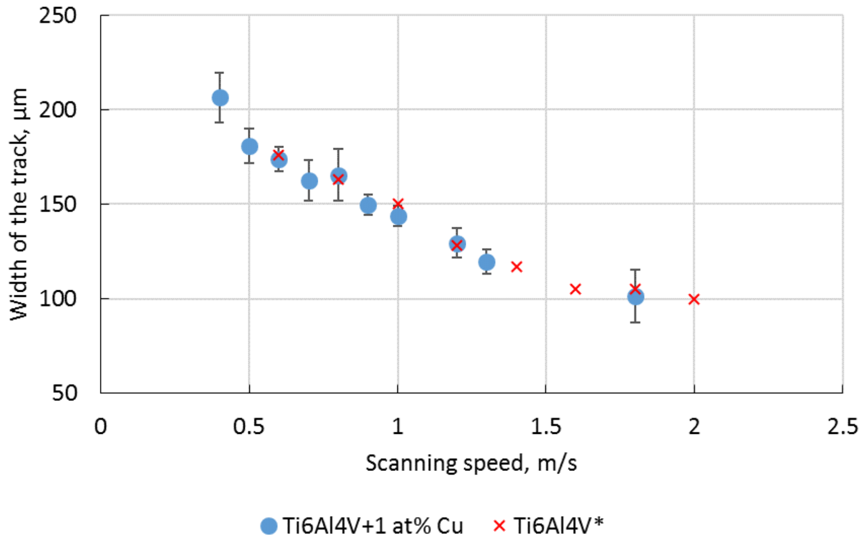

Figure 56. Width of single tracks at 170 W laser power at different scanning speeds for Ti6Al4V- 1a.t%. Cu and Ti6Al4V (Els, 2014)

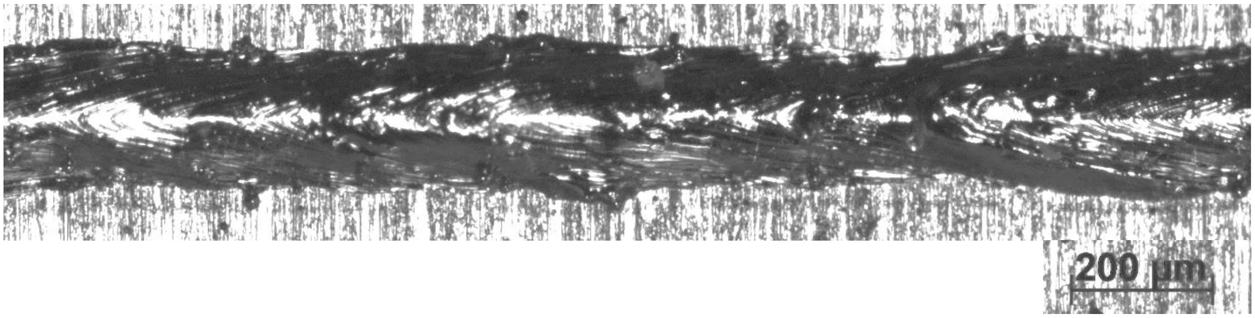

Figure 57. Top view of Ti6Al4V- 1at.% Cu single track at 170 W laser power at 0.4 m/s scanning speed

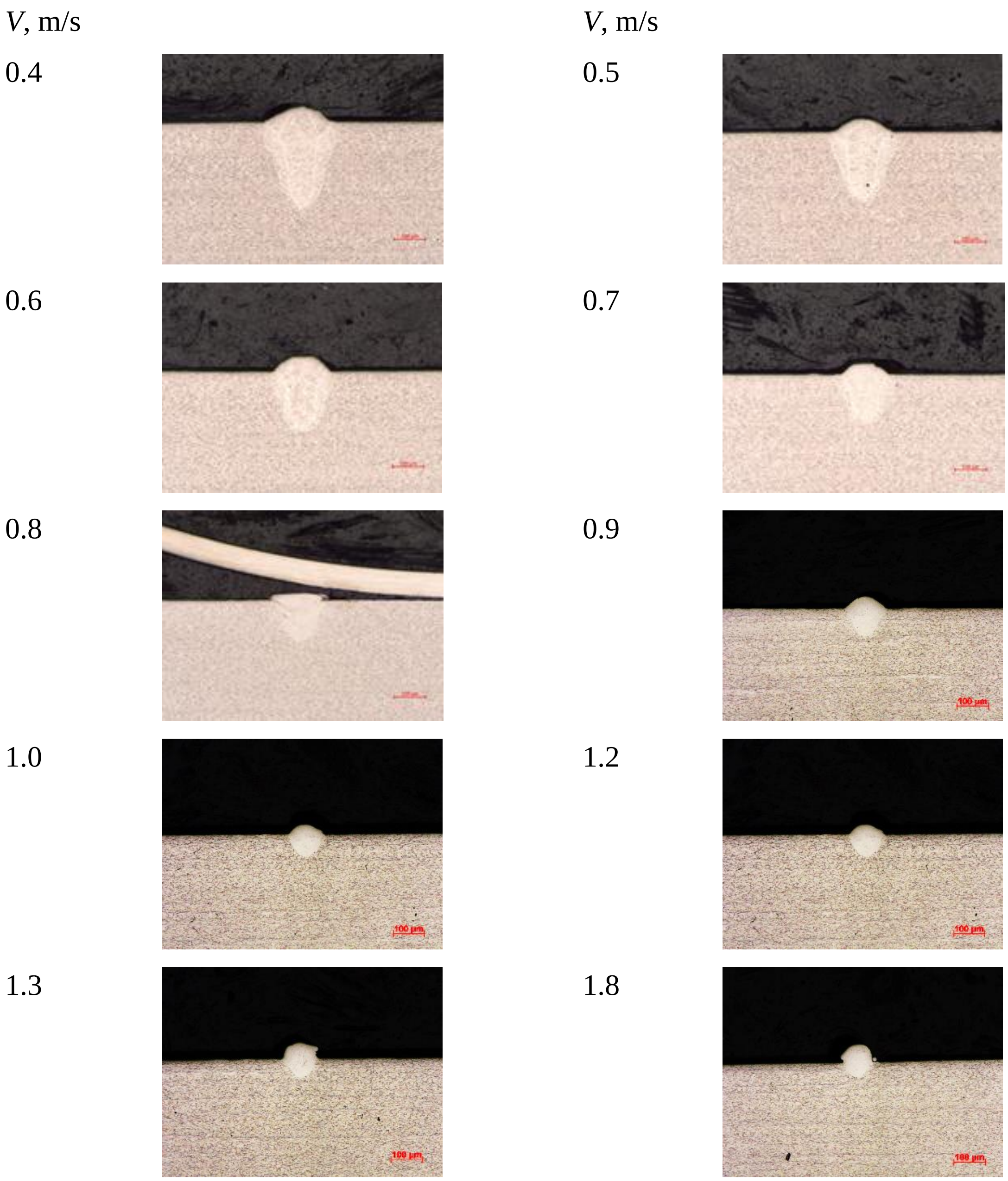

Figure 58. Cross-sections of single tracks at 170 W laser power at different scanning speeds for Ti6Al4V-1at.% Cu

Penetration depth decreased with increasing scanning speed (Figure 59). At higher scanning speed the interaction time of the laser beam radiation and material became shorter. This resulted in fusing only the powder and top surface of the substrate due to the reduction in adsorbed energy. At 1.8 m/s, when humping effect started, the remolten depth was approximately 50 µm. Tracks were irregular, but continuous which supported the theory with regards to the stabilising effect of the penetration into the substrate for LPBF tracks (Yadroitsev *et al.*, 2010).

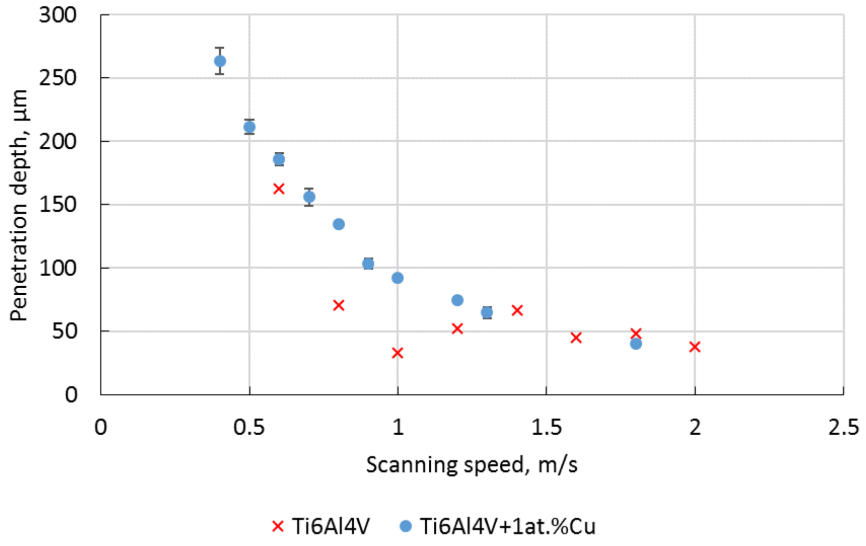

Figure 59. Penetration depth of single tracks at 170 W laser power at different scanning speeds for Ti6Al4V-1at.% Cu and Ti6Al4V (Els, 2014)

4.1.2. First and second layer formation

The average width of the tracks was approximately 160 µm for continuous tracks formed at 0.4-1.3 m/s. Earlier Kinnear *et al.* (2016) showed that Ti6Al4V-*x*Cu single tracks had higher Cu concentration on the edges. It was decided to choose a half-track width (50%) as a hatch distance (for Ti6Al4V it is about 20% of the single track's width) and to use rescanning between the tracks to increase homogeneity of copper distribution.

Solidification lines and grain boundaries were clearly visible at the surface of sintered layers (Figure 60). The *in-situ* alloyed Ti6Al4V–1at.% Cu LPBF surface morphology showed complex behaviour when compared to energy input. Surface morphology depends on the shape of the single tracks and the hatch distance that is shifting between tracks. At chosen hatch distance of 80 µm, the surface roughness increased with scanning speed (Figure 61). Surfaces at higher scanning speeds produced humping effect and more satellites as the molten pool became more pronounced, especially at higher laser power. Layer surface quality dramatically decreased at 2-layer 1% copper samples with a lower energy input (Figure 62). Surface roughness doubled at 2-layer samples when irregular single track effects formed (V = 1.3 m/s). The previous surface with a high surface roughness served as a substrate for the next layer. This high surface roughness resulted in an uneven powder layer for the next surface, which leads to an irregular sintered layer.

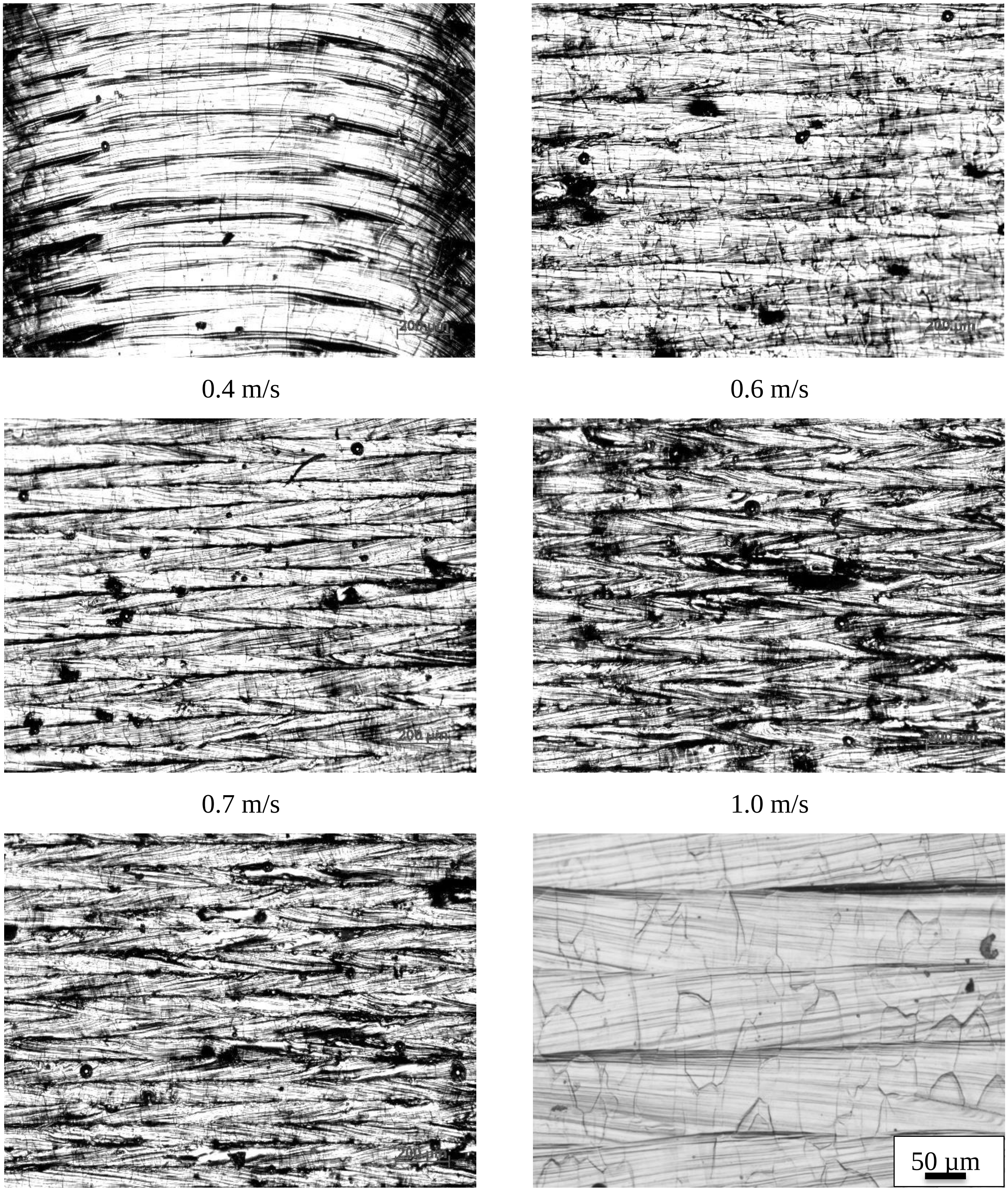

0.4 m/s

0.6 m/s

0.7 m/s

1.0 m/s

1.3 m/s

0.6 m/s

Figure 60. Single layers at 170 W and, 0.4-1.3 m/s in Ti6Al4V- 1at.% Cu samples at hatch distance of 80 µm

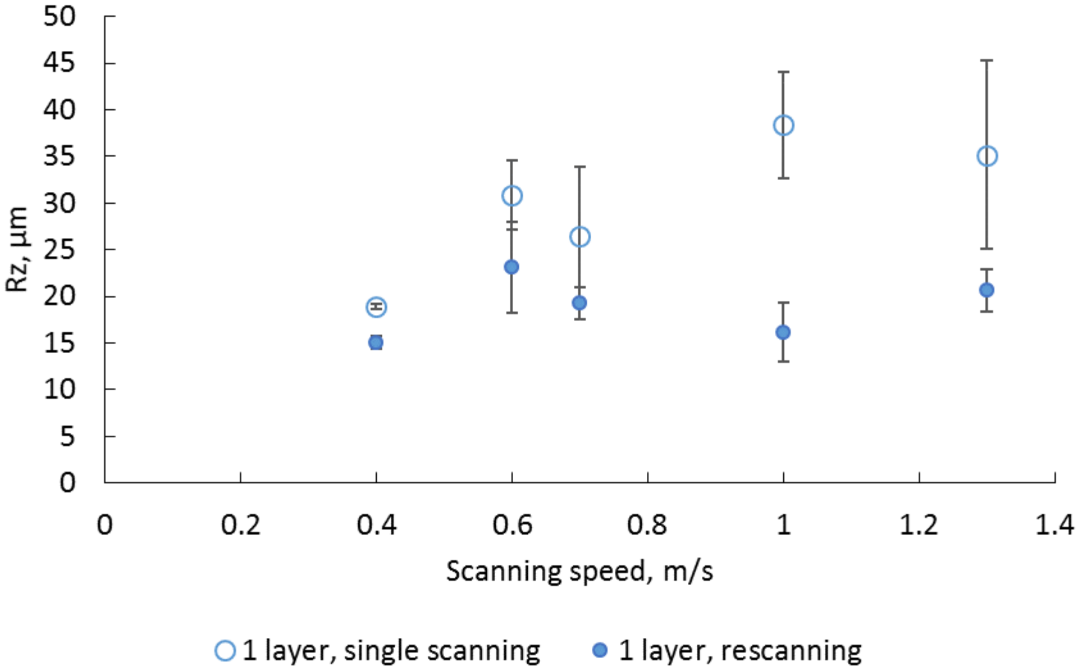

Figure 61. Surface roughness of first layer at 170 W and 0.4-1.3 m/s in Ti6Al4V- 1at.% Cu samples at hatch distance of 80 µm with single scanning and rescanning

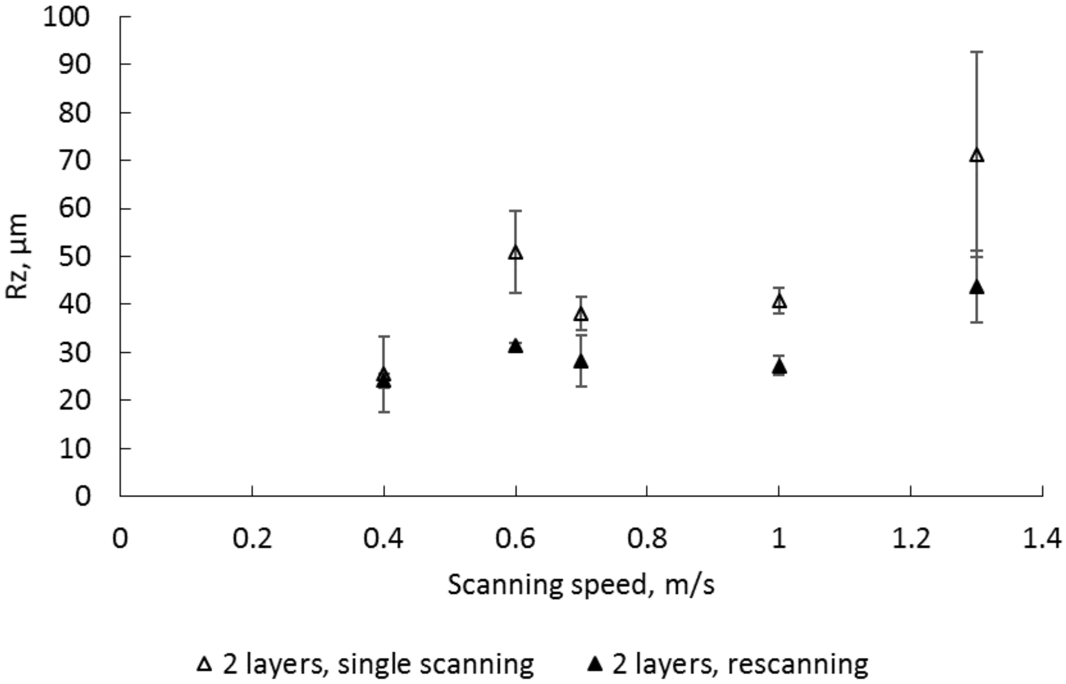

Figure 62. Surface roughness of two-layers samples at 170 W and 0.4-1.3 m/s in Ti6Al4V- 1at.% Cu samples at hatch distance of 80 µm with single scanning and rescanning

Rescanning dramatically changed the surface morphology of the top layer and had a profound effect on the surface homogeneity, as showed by Kinnear *et al.* (2016). The rescanning strategy removed the concentrations of copper that formed at the peripheries of the single tracks. Similarly to single exposure during rescanning, the copper inhomogeneity increased with scanning speed and hatch distance. An increase in input energy has a positive effect on surface homogeneity. A rescanning strategy provides an effective means to improving the surface homogeneity, and causes a stirring effect inside the layer at *in-situ* alloying.

Cross-sectional analysis of the samples showed that when deep penetration depth in single tracks formed, keyhole mode of laser melting led to porosity in 3D samples (Figure 63).

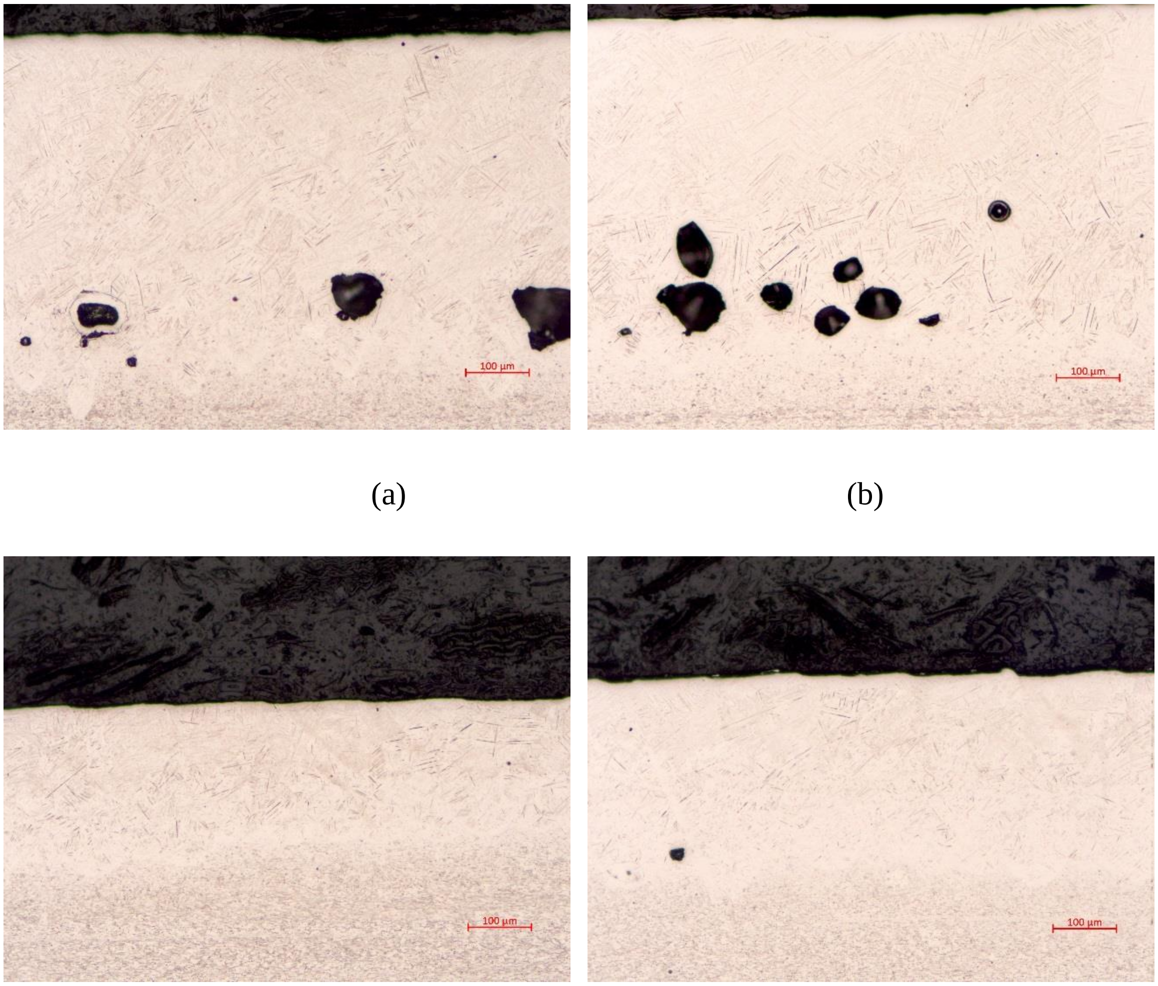

(a) (b)

(c) (d)

Figure 63. Cross-sections of Ti6Al4V-1at.% Cu single layers in at 170 W, 0.4 m/s (a, b) and 0.6 m/s (c, d) at hatch distance of 80 µm: single scanning (a, c) and rescanning (b, d)

At scanning speeds of 0.7-1.3 m/s, samples had no pores inside as analysis of cross-sections illustrated. However, some inhomogeneous areas were found (Figure 64a, top left side).

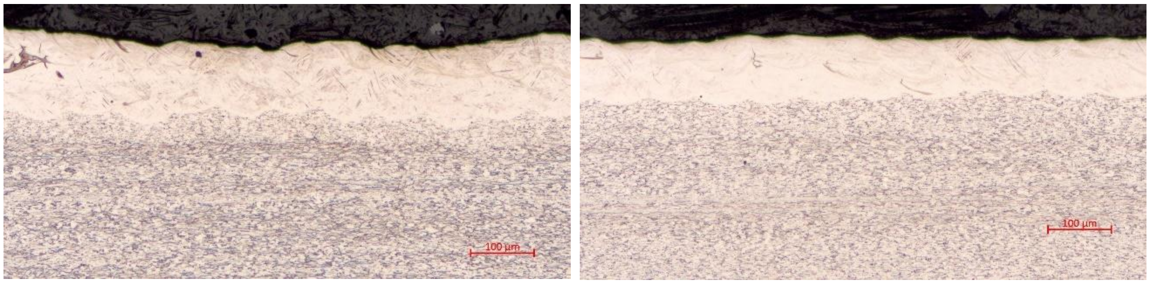

(a) (a)

Figure 64. Cross-sections of Ti6Al4V- 1at.% Cu single layers in at 170 W, 1.3 m/s at hatch distance of 80 µm: single scanning (a) and rescanning (b)

EDS mapping of samples showed homogenous copper distribution at 0.7-1.0 m/s scanning speed after rescanning. At a low scanning speed of 0.7 m/s, the top surface and cross section of the layer were homogenous (Figure 65-Figure 66).

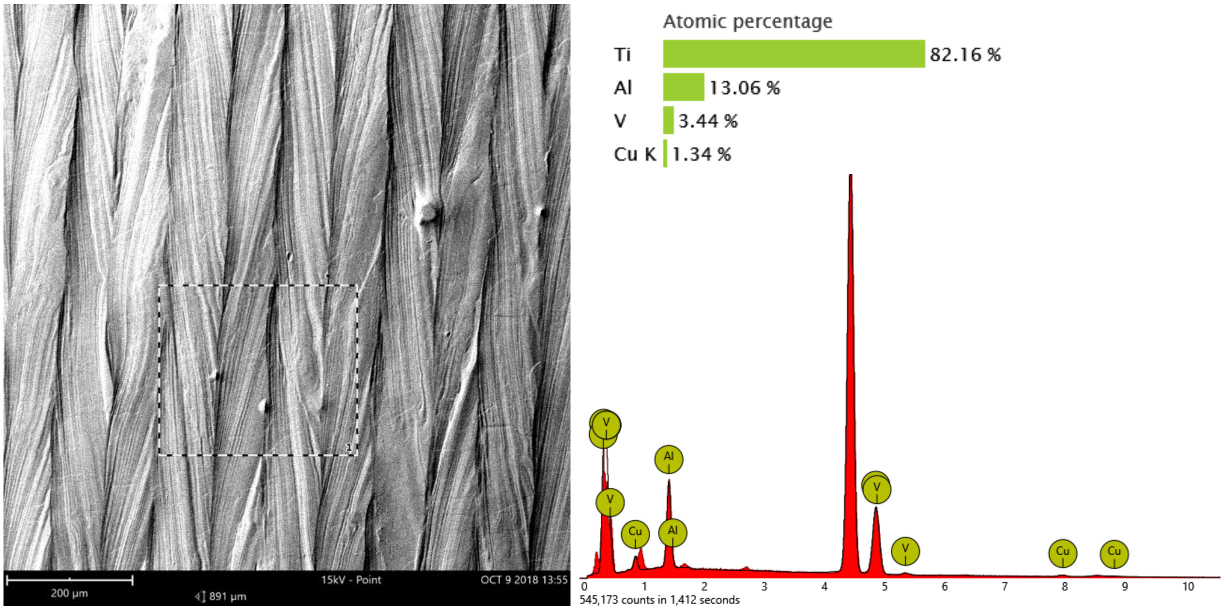

(a) (b)

Figure 65. BSE image (a) and EDS spectrum of the top surface (b) of Ti6Al4V-1 at.% Cu sample at 170 W and 0.7 m/s, 80 µm hatch distance

Quantitative analysis of Ti6Al4V-1at.% Cu samples showed difficulty since the concentration level of copper was very low, especially for the first layer and single tracks because the Ti6Al4V substrate fused by the laser beam with the powder mixture (Figure 66).

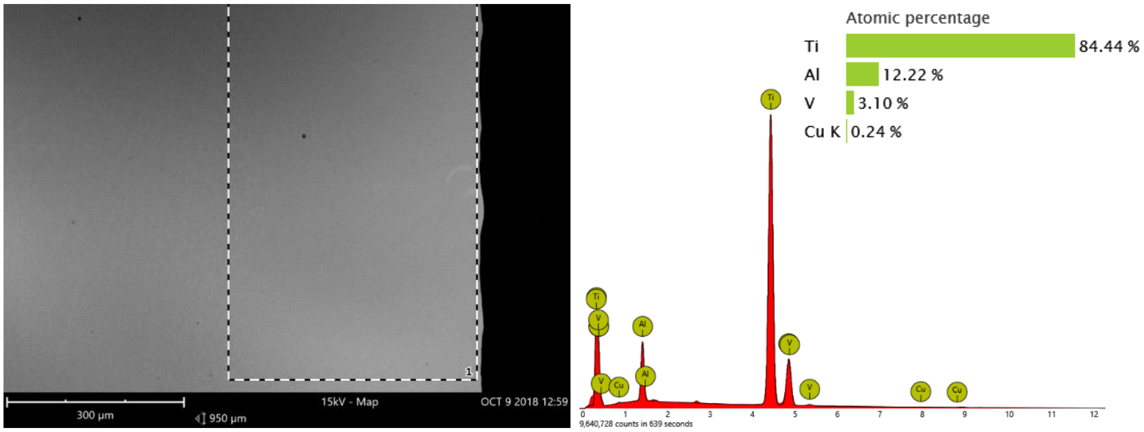

(a) (b)

Figure 66. BSE image (a) and EDS spectrum of the cross-section (b) of Ti6Al4V-1 at.% Cu sample at 170 W and 0.7 m/s, 80 µm hatch distance

It was concluded that non-porous Ti6Al4V-1 at.% Cu samples can be produced at 0.7 m/s with 170 W laser power. When rescanning is applied, scanning speed can be increased up to 1.0 m/s. In industry, rescanning of 3D parts is not cost effective, due to the increase in manufacturing time, therefore only the final (outer) layer is re-scanned to reduce the surface roughness. Further investigations of Ti6Al4V-1at.% Cu 3D samples manufactured at these process parameters, will be done in the future.

4.2. Ti6Al4V -3at.% Cu structures

4.2.1. Single tracks at different process parameters

On the basis of experiments described above, it was decided to increase the percentage of copper powder in the mixture. Since higher laser power lead to increased temperature and higher scanning speed causes strong flows in the molten pool (Makoana *et al.*, 2018), these experiments were done at laser power 170 W and 340 W. The goal was to increase productivity and homogeneity of *in-situ* alloyed 3D samples. Experiments of single tracks were done for 170 W and 340 W laser power and scanning speeds of 0.4-2.8 m/s. Balling effect started at 1.6 m/s scanning speed for 340 W and at 1.4 m/s for 170 W (Figure 67).

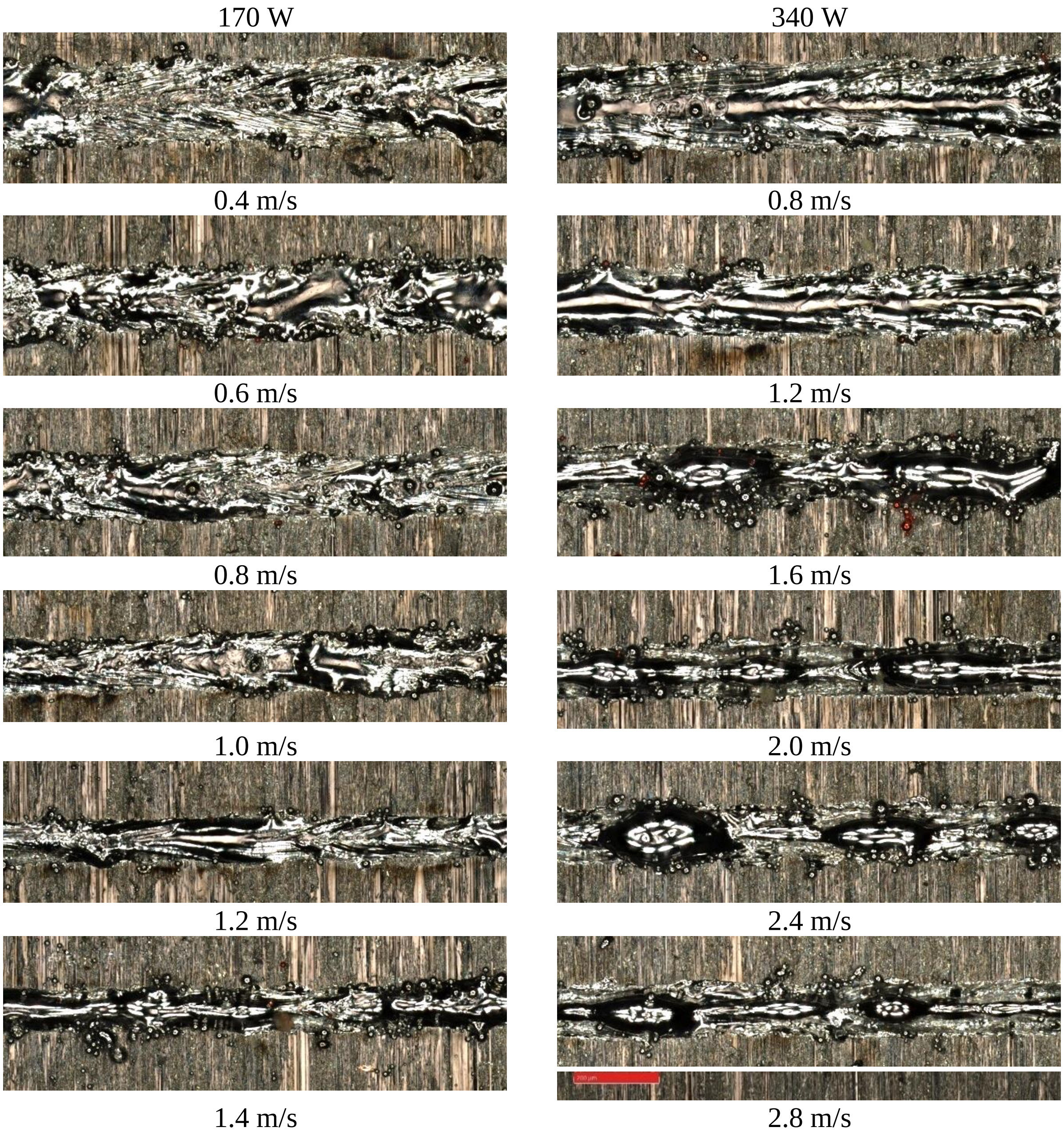

Figure 67. Top view of the Ti6Al4V- 3at.% Cu single tracks at 170 W and 340 W and scanning speeds 0.4-2.8 m/s

Many satellites were observed on and alongside the single tracks. These tracks were also irregularly shaped in comparison with Ti6Al4V tracks without Cu addition, (Figure 68). The high thermal conductivity of copper and a lower melting point resulted in metallurgical contact of particulates from affected areas (Yadroitsev, 2009) and formed a sparking effect (Khairallah, 2016).

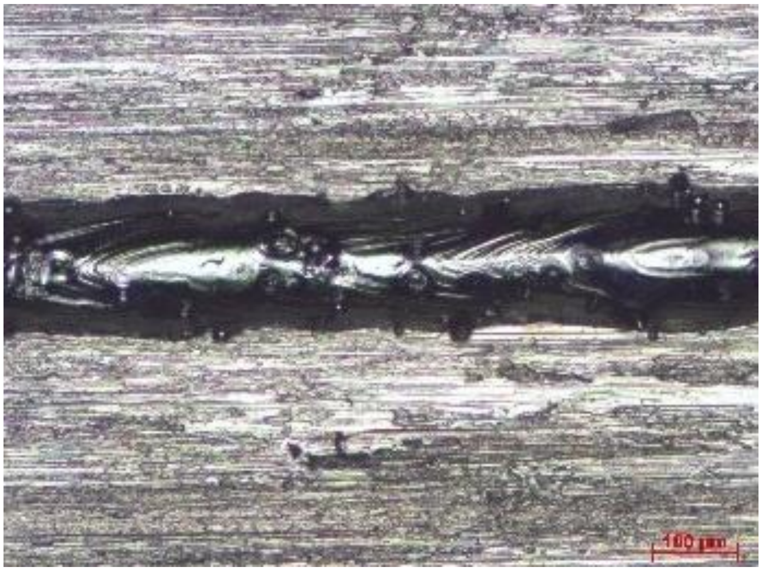

Figure 68. Top view of the Ti6Al4V single track at 200 W and 0.8 m/s scanning speed

Microscopically it was difficult to investigate the profile of the sintered tracks exactly parallel to the scanning direction and along the track centre. Analysis of profiles showed that the minimum height of the tracks was approximately half of the powder layer thickness (60/2=30 µm), which suggests that the apparent density of the powder layer is about 50% (Kinnear, 2016). High deviation started at expressed balling effect at 1.6 m/s. At 170 W, tracks were irregular at a scanning speed of 1.4 m/s (Figure 69-Figure 70).

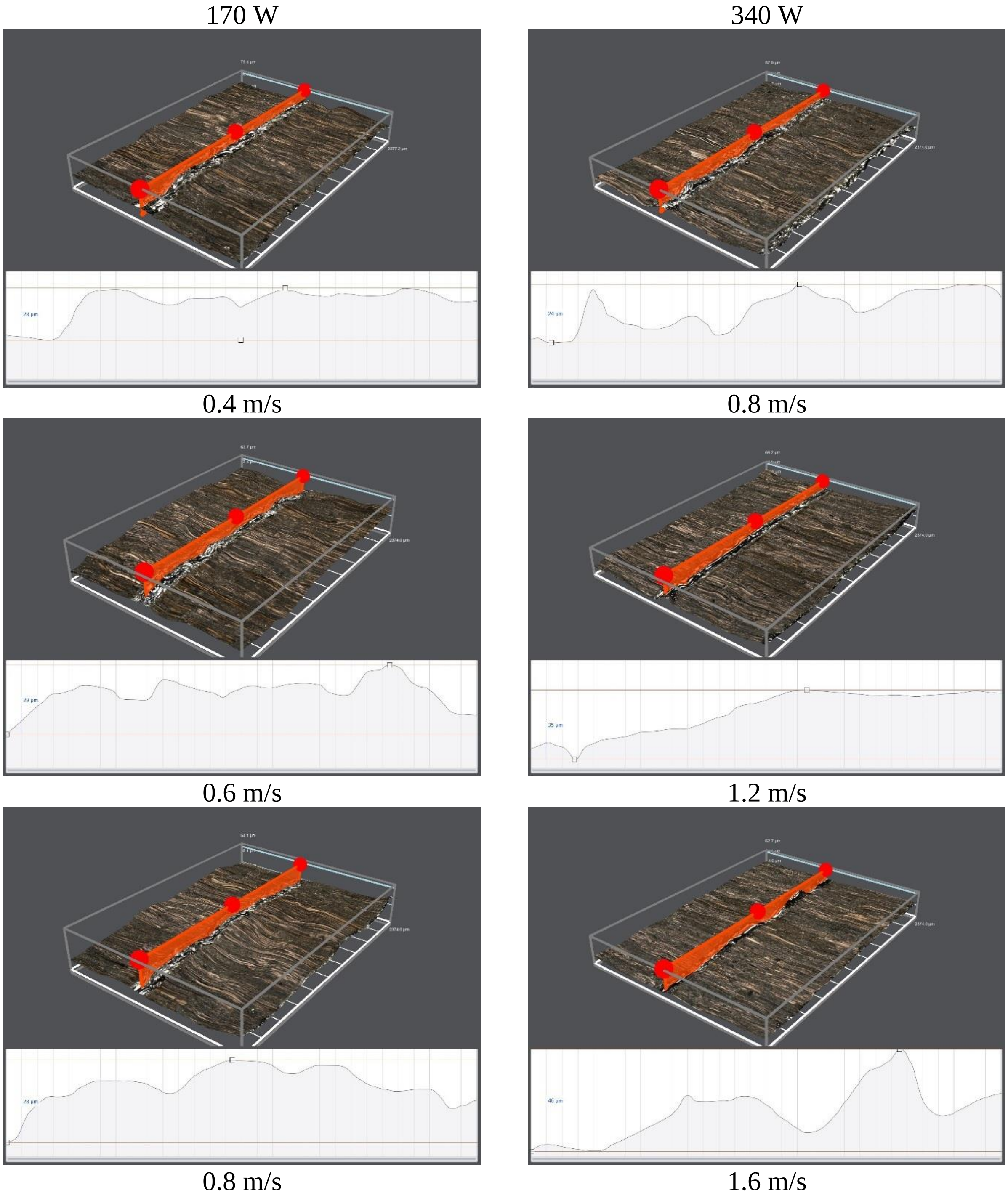

Figure 69. 3D reconstruction and profile of Ti6Al4V- 3at.% Cu single tracks using SmartZoom 5 digital microscope at scanning speeds 0.4-1.6 m/s

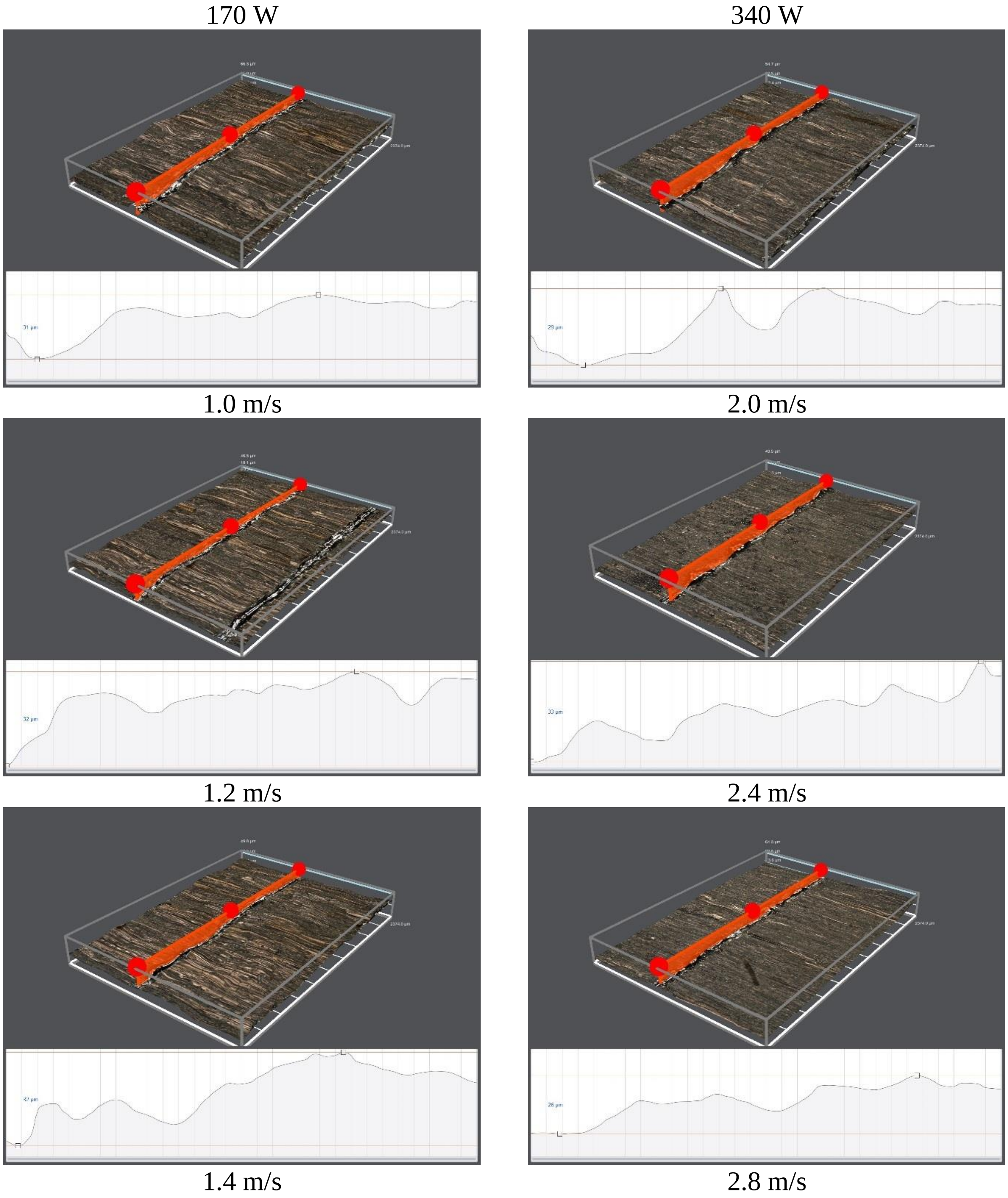

Figure 70. 3D reconstruction and profile of Ti6Al4V- 3at.% Cu single tracks using SmartZoom 5 digital microscope at scanning speeds of 1.0-2.8 m/s

In terms of linear laser energy density (the ratio of laser power to the scanning speed) no significant difference was found in track width for similar energy density. Increasing the laser power by a factor of two leads to a difference in track width of approximately 50 µm. The track width is defined by laser spot size and powder layer thickness (Yadroitsev *et al.*, 2010) which was ~80 µm and ~50 µm, respectively. For 340 W, the width of the tracks varied from 201±21.5 µm at 0.8 m/s scanning speed to 121±12.2 µm at 2.8 m/s. At the lower laser power setting of 170 W, it was 195±8.7 µm to 110±8.8 µm at scanning speeds of 0.4-1.4 m/s (Figure 71).

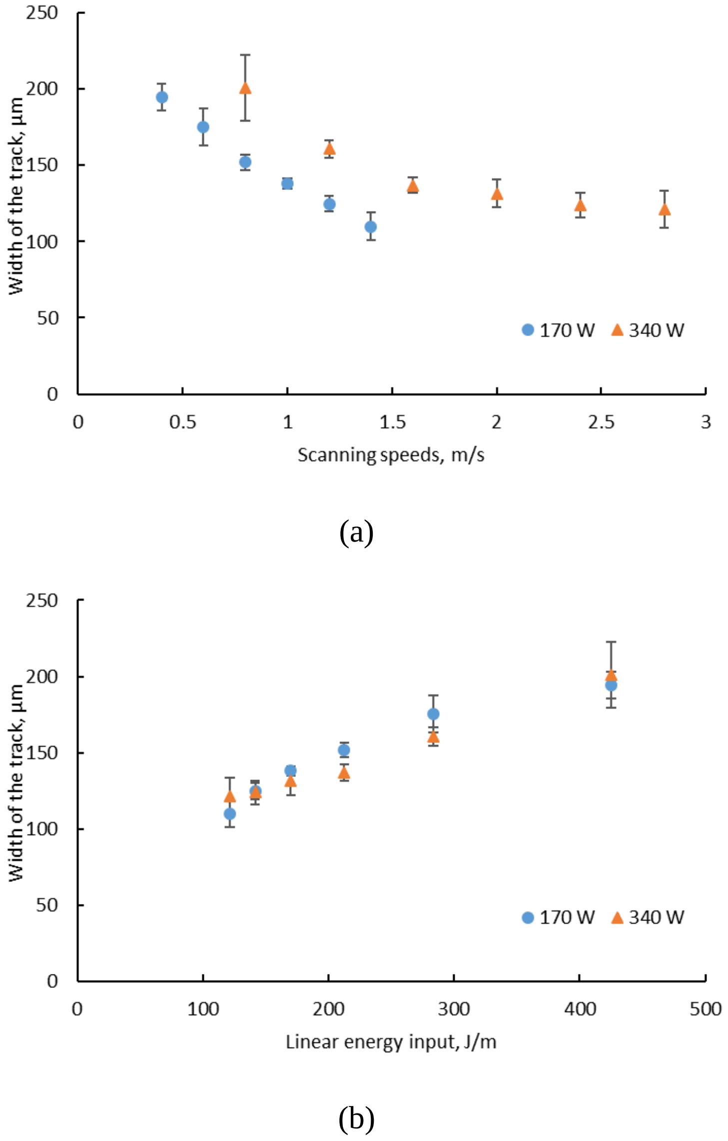

Figure 71. Width of Ti6Al4V- 3at.% Cu single tracks versus scanning speeds (a) and linear energy input (b)

Analysis of cross-sections perpendicular to the scanning direction of single tracks was done to estimate the LPBF melting mode and penetration depth of the molten pool. The molten pool depth increased significantly with an increase in laser power (Figure 72). In terms of linear energy input, at 170 W laser power, the penetration depth was slightly higher because of the laser beam interaction time. At longer interaction time (Figure 73), flows developed in the molten pool and keyhole mode was observed during cross-section analysis.

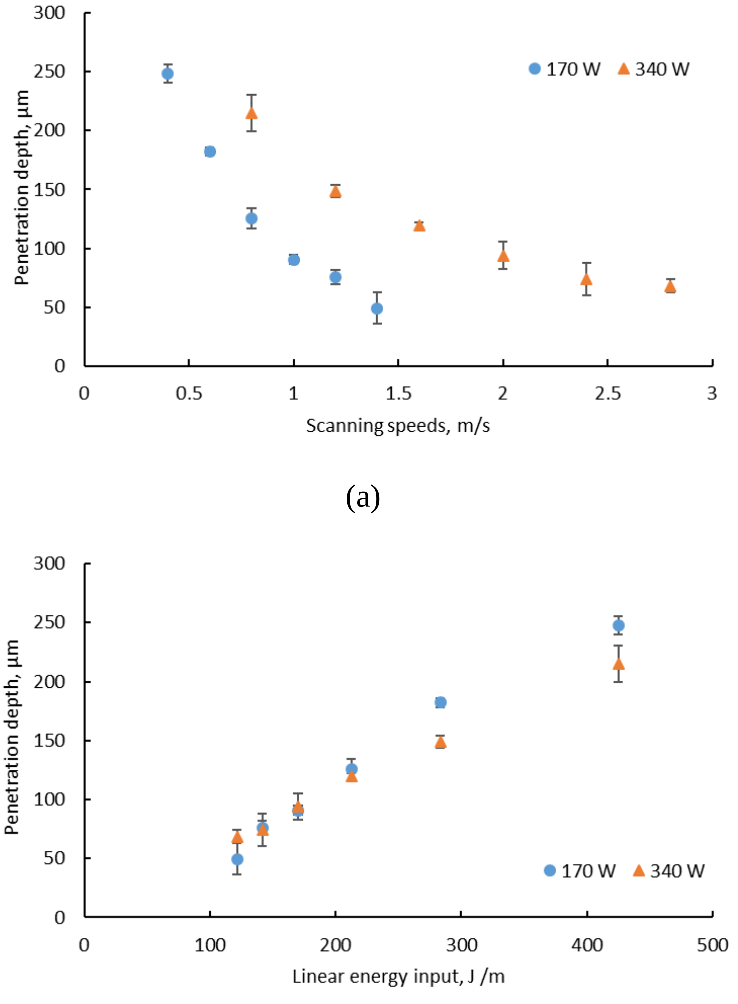

(a)

(b)

Figure 72. Penetration depth of Ti6Al4V- 3at.% Cu single tracks versus scanning speeds (a) and linear energy input (b)

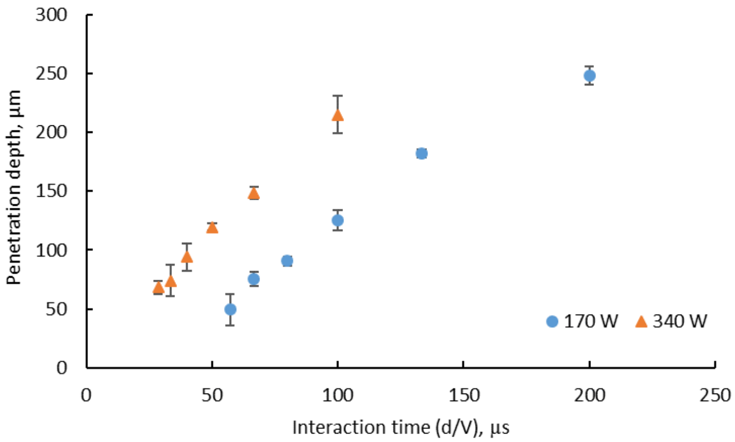

Figure 73. Penetration depth of Ti6Al4V- 3at.% Cu single tracks versus interaction time (ratio of the laser spot diameter to the scanning speed)

Analysis of the cross-sections revealed that keyhole mode of laser melting started at 0.4–0.6 m/s for 170 W and at 0.8 m/s for 340 W laser power (Figure 74), which is similar to 1at.% Cu samples. The data did not show a significant difference (*student t-test*) between 1% and 3% copper addition in the width of the track or in penetration depth. It must be noted that all experiments were conducted on a Ti6Al4V substrates, which contributed to the geometrical characteristics of the single tracks during additions of small amounts of copper powder.

At high penetration depth, instabilities in the molten pool are prominent and cavities are formed as the liquid solidifies. Humping of molten pool and undercuts at high scanning speeds were very prominent at higher laser power (340 W) and the copper penetrated deeper into the substrate. At low scanning speeds tracks appear more homogenous for both 170 W and 340 W power settings. At investigated scanning speeds, liquid flow was very pronounced but it seems solidification was faster and enriched copper areas were clearly visible at cross-sections. Inhomogeneity was found deeper in the tracks for scanning speeds 0.6 m/s and 1.2 m/s for 170 W and 340 W laser power respectively. Analysis of the cross-sections showed that enriched copper areas were prominent near the edges of the tracks. To build single layers, a hatch distance of 80 µm was selected, similar to that of Ti6Al4V-1at% Cu.

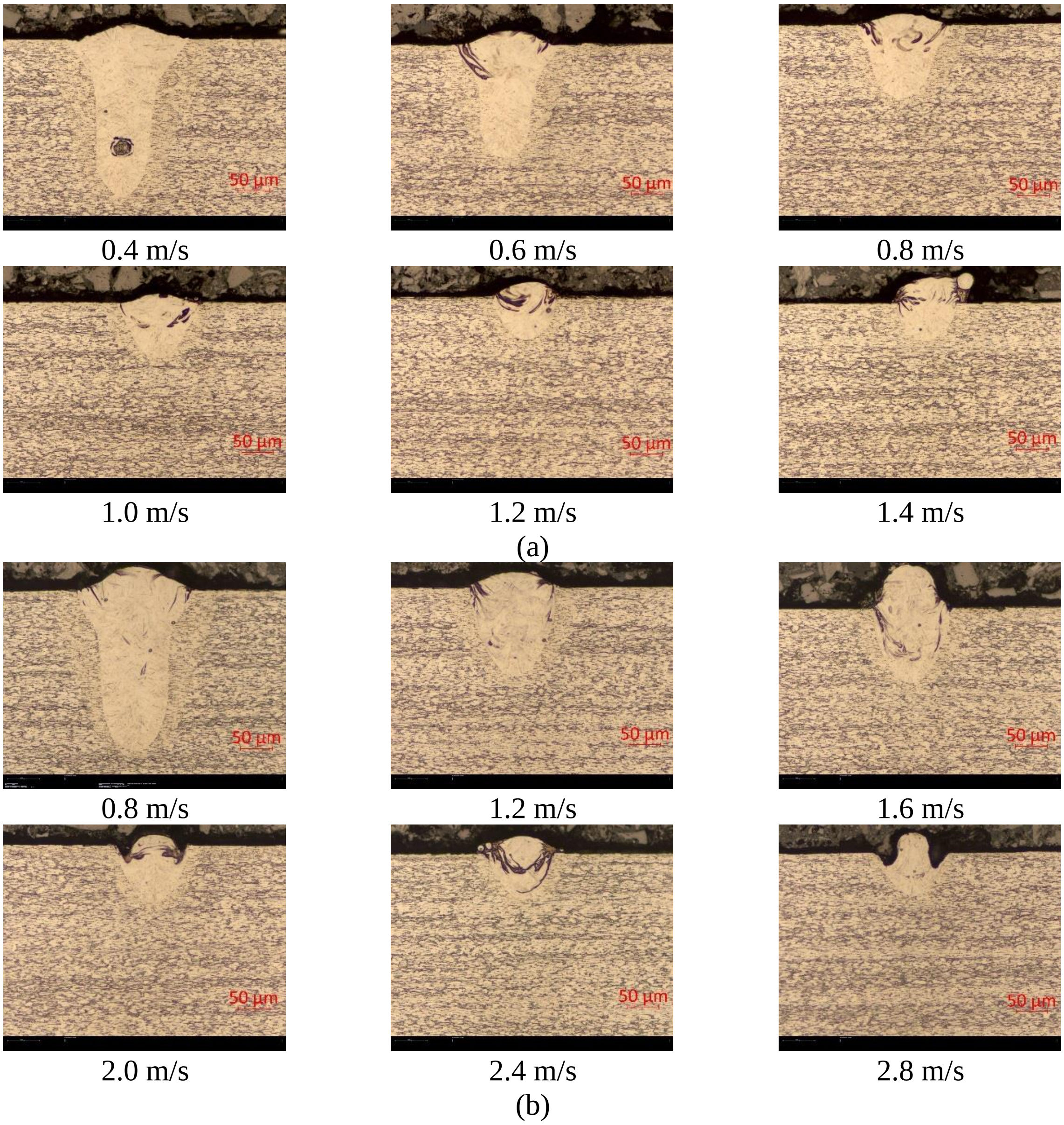

Figure 74. Cross-sections of Ti6Al4V- 3at.% Cu single tracks at 170 W (a) and 340 W (b)

4.2.2. Single layers morphology

Analysis of topology for the surfaces of the first single layer showed that in comparison with 1at.% Cu addition, 3at.% Cu samples were much smoother after laser scanning: at similar laser power *Rz* was about 10-25 µm *versus* 20-50 µm in 1% samples (Figure 75-Figure 78). This can be explained by the low melting point, low viscosity and good wetting behaviour of copper. At 340 W, more expressed balling effect leads to a variation of track width and undercutting (Figure

74), which yielded a higher surface roughness for 340 W samples in comparison to 170 W samples.

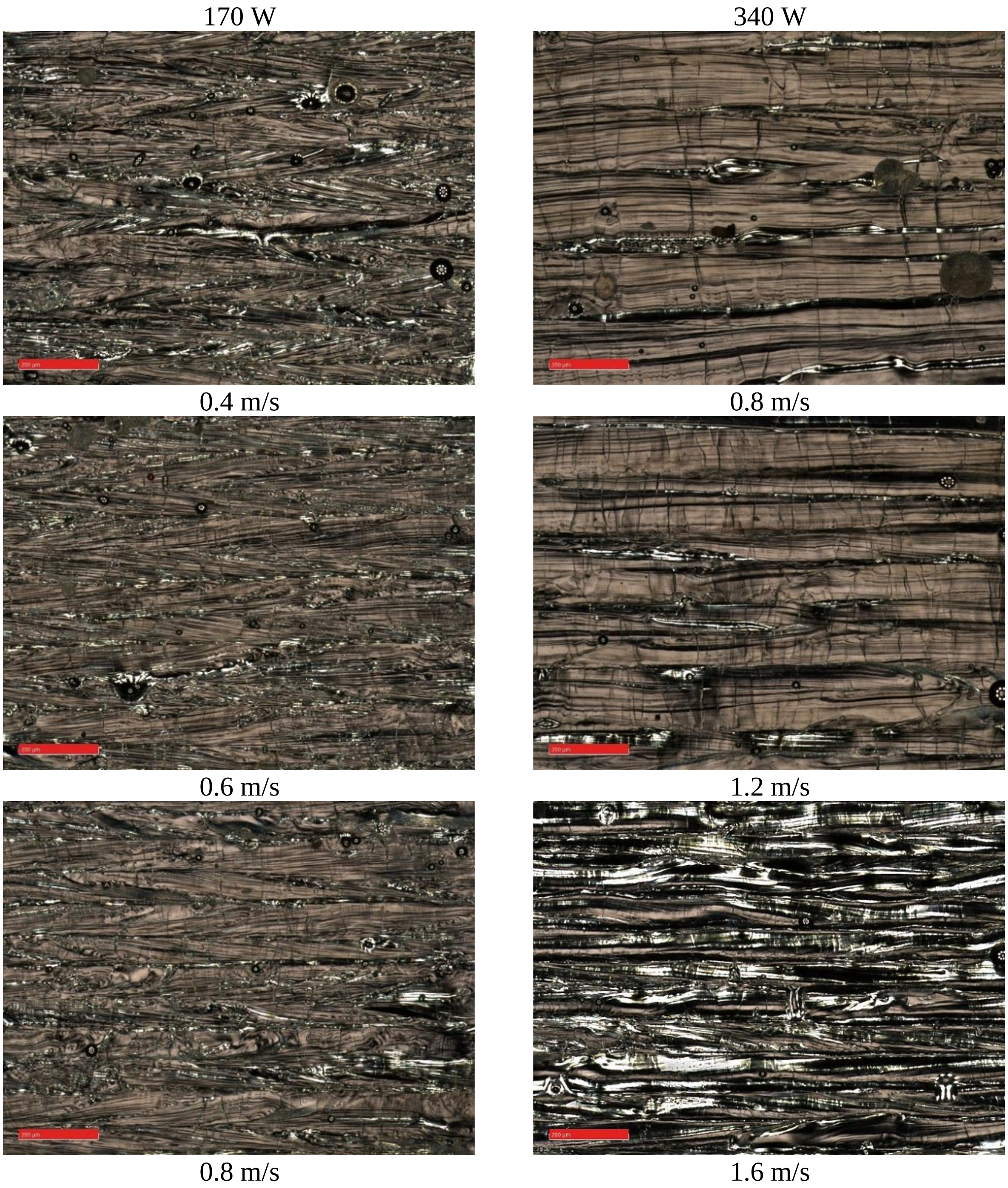

Figure 75. Top surfaces of the first layer at 170 W and 340 W and scanning speeds 0.4-1.6 m/s for Ti6Al4V-3at.% Cu samples

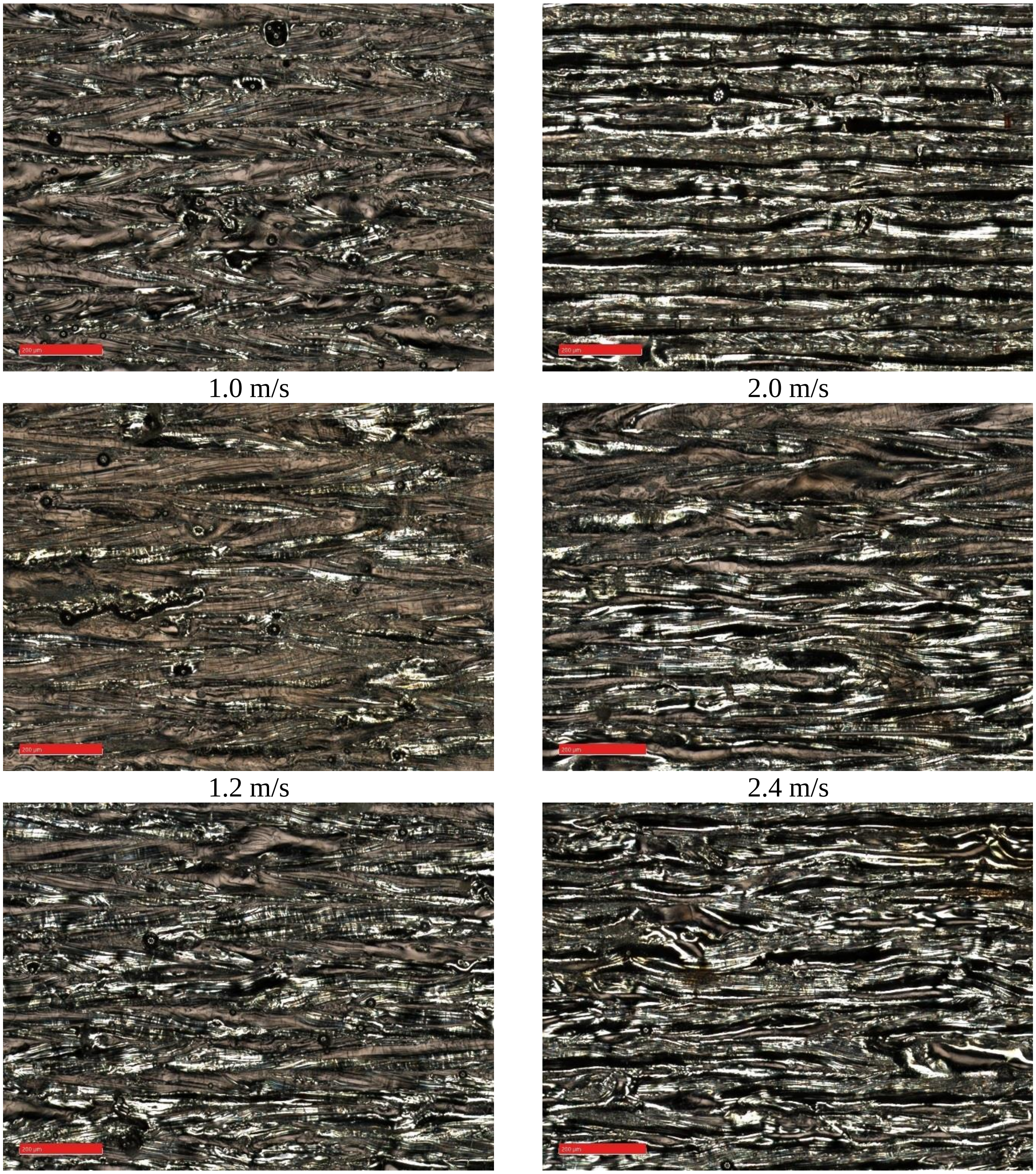

1.0 m/s 2.0 m/s

1.2 m/s 2.4 m/s

1.4 m/s 2.8 m/s

Figure 76. Top surfaces of first layer at 170 W and 340 W and scanning speeds 1.0-2.8 m/s for Ti6Al4V-3at.% Cu samples

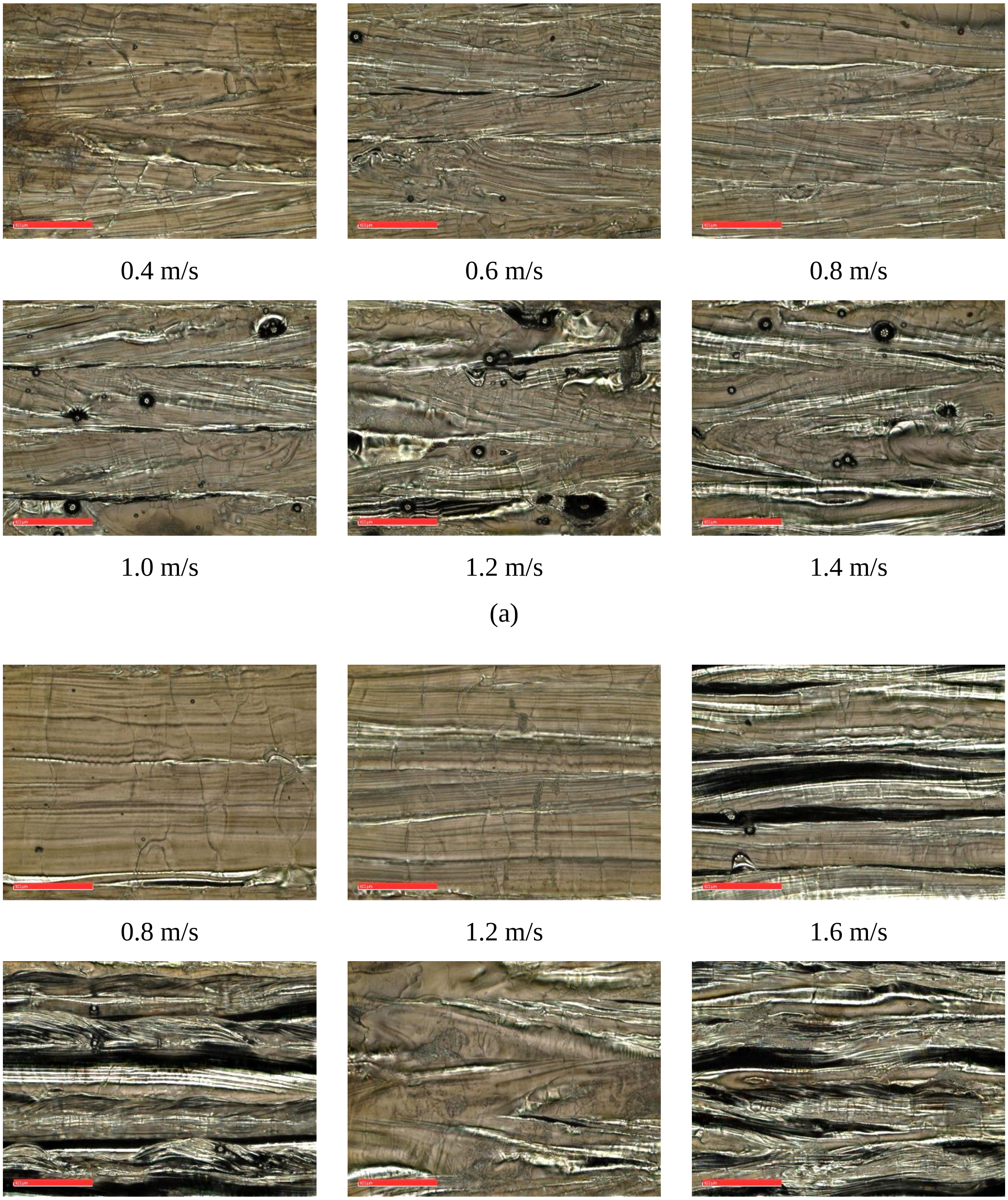

0.4 m/s 0.6 m/s 0.8 m/s

1.0 m/s 1.2 m/s 1.4 m/s

(a)

0.8 m/s 1.2 m/s 1.6 m/s

2.0 m/s 2.4 m/s 2.8 m/s

(b)

Figure 77. Top surfaces single layer at 170 W (a) and 340 W (b), 0.4-2.8 m/s scanning speeds for Ti6Al4V-3at.% Cu samples

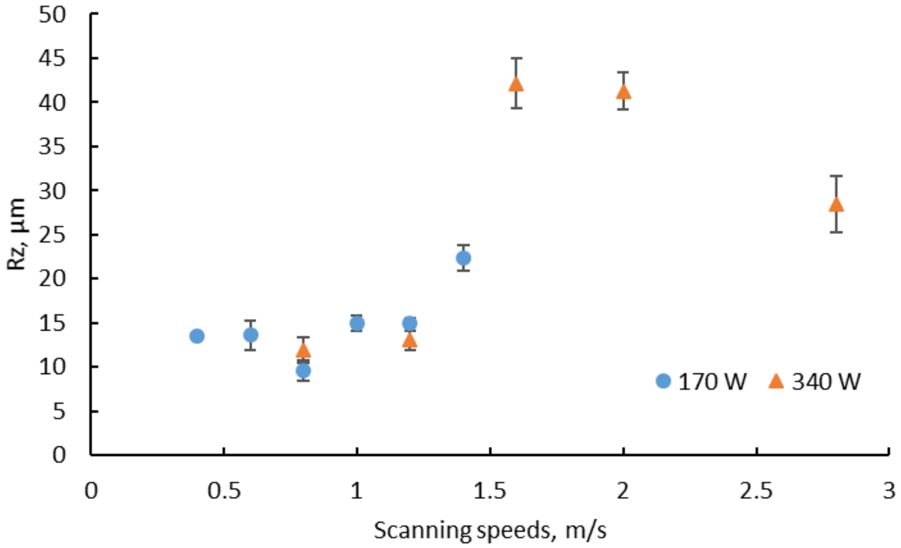

(a)

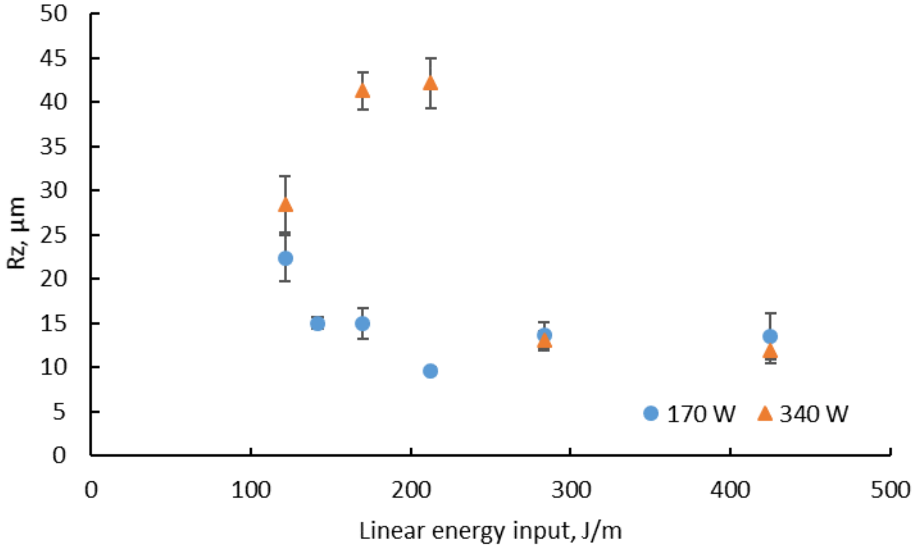

(b)

Figure 78. Surface roughness Rz of single layers at 170 W (a) and 340 W (b) versus scanning speed (a) and linear energy input (b) for Ti6Al4V-3at.% Cu samples

3D reconstruction of the surfaces by digital microscope supported observations that at 340 W laser power topology of the powder layer was more irregular (Figure 79-Figure 80). Under visual monitoring, spatter formation and sparking effect (Lutter-Günther *et al.*, 2018) were more expressed under higher laser power, so it was decided to register it for the next 5% Cu addition experiments by camera.

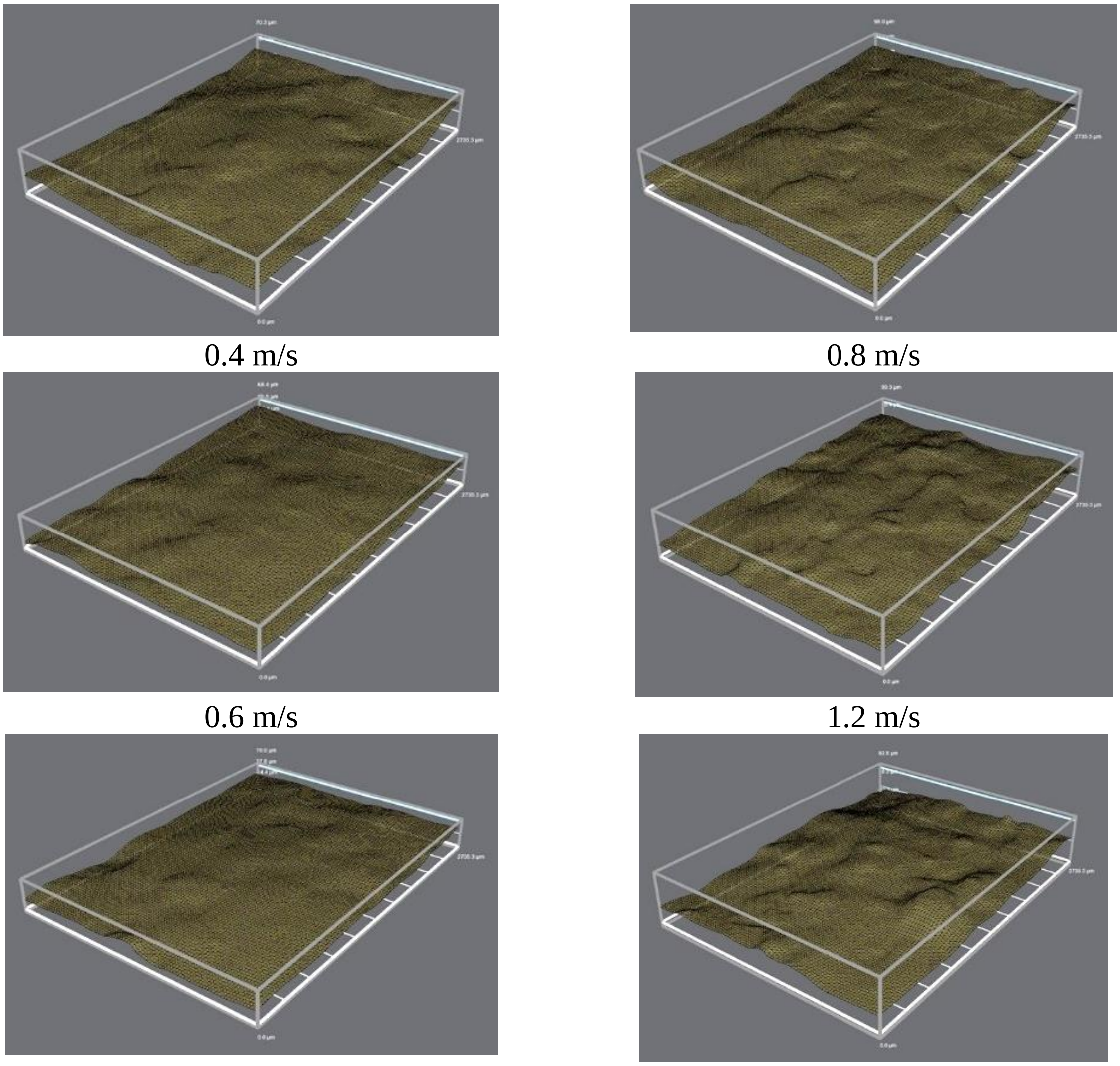

170 W

340 W

0.4 m/s

0.8 m/s

0.6 m/s

1.2 m/s

0.8 m/s

1.6 m/s

Figure 79. 3D reconstruction of single layers at 170 W and V=0.4-0.8 m/s and 340 W and V=0.8-1.6 m/s for Ti6Al4V-3at.% Cu samples

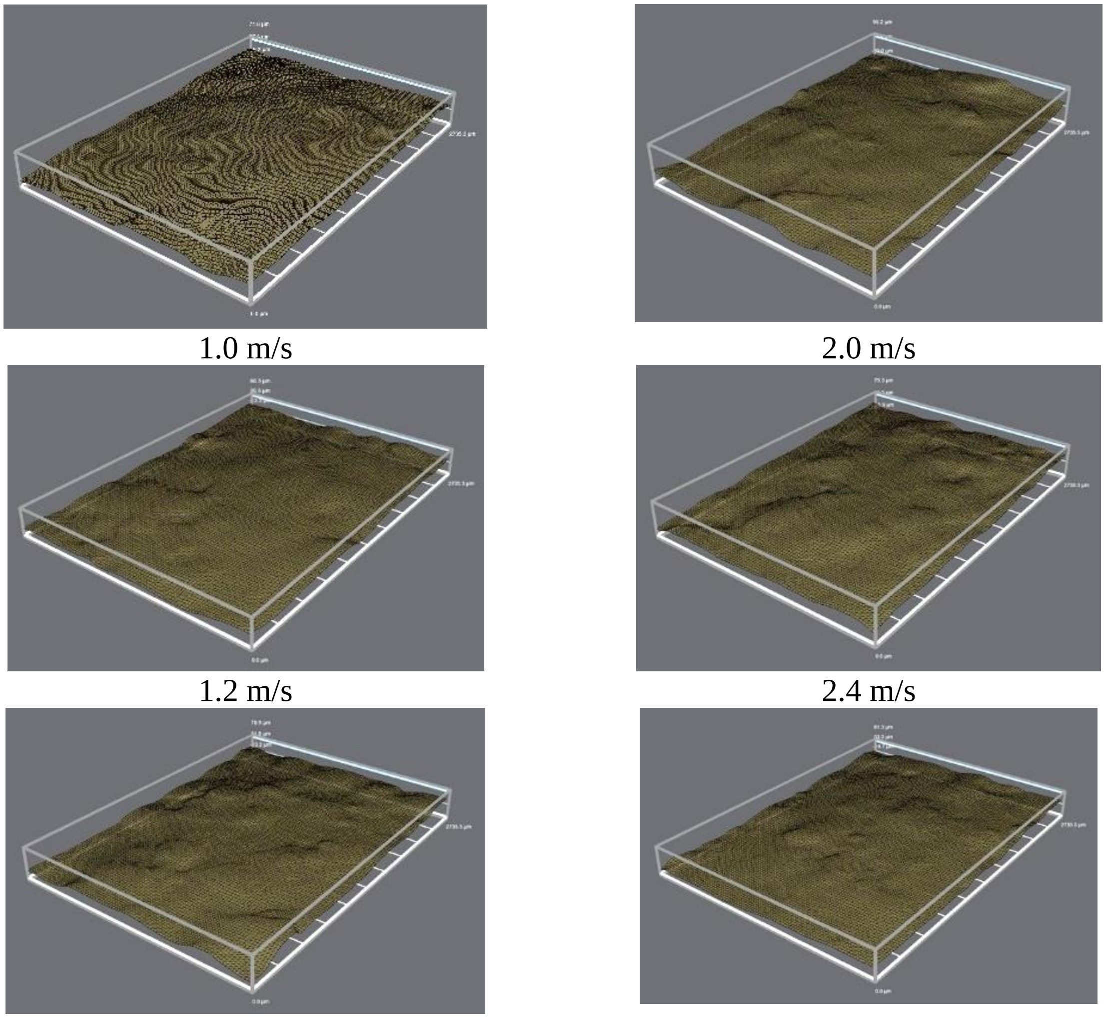

1.0 m/s 2.0 m/s

1.2 m/s 2.4 m/s

1.4 m/s 2.8 m/s

Figure 80. 3D reconstruction of single layers at 170 W and V=1.0-1.4 0.8 m/s and 340 W and V=2.0-2.8 m/s for Ti6Al4V-3at.% Cu samples

Cross-sectioning of the single layers, perpendicular to the scanning directions at scanning speed higher than 1.6 m/s demonstrated a very irregular surface, especially for 340 W laser power when expressed balling started (Figure 81). These irregular surfaces can lead to a high deviation in powder layer thickness for 3D samples and provoke porosity since the single layer sintered previously is the substrate for the subsequent layer.

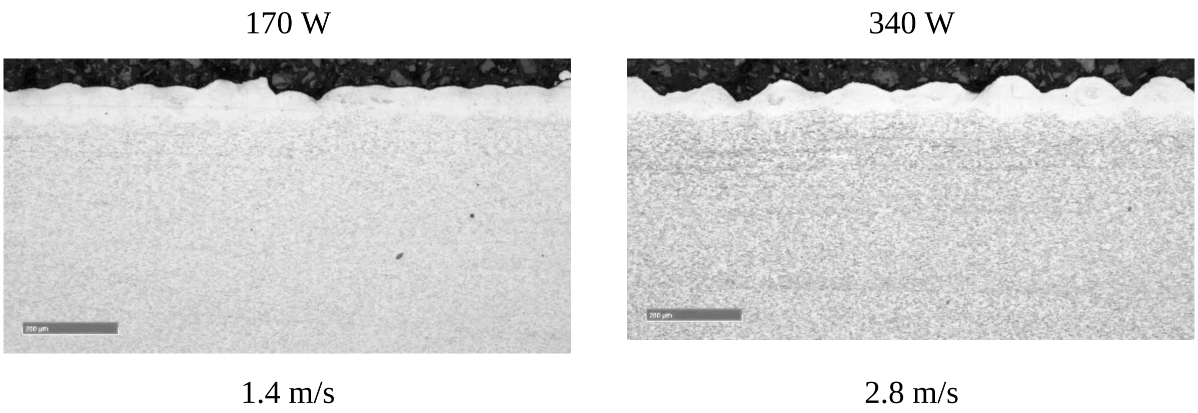

170 W

340 W

1.4 m/s

2.8 m/s

Figure 81. Cross-sections of Ti6Al4V-3at.% Cu single layer at P=170 W, V=1.4 m/s (a) and 340 W and V=2.8 m/s (b)

Small cracks were found at the top of the samples (Figure 82a) during SEM analysis of the cross-sections. These small cracks could have originated from different shrinkages of pure copper and Ti6Al4V. When the sintered layer cools down, high stresses during solidification can provoke crack creation. The linear expansion coefficient of copper is double that of Ti6Al4V and the ultimate tensile strength is very low in comparison with Ti6Al4V (see Table 2 and Table 4). Future analysis has to be done for verification of the critical concentration of Cu when cracks are formed because in some cross-sections cracks were not found (Figure 82b). For 3D samples, the upper part of the layer is the substrate for the consecutive layer that could be re-melted to aid homogeneity. Therefore, it is important to note that inhomogeneous copper distribution can initialise cracks in 3D samples.

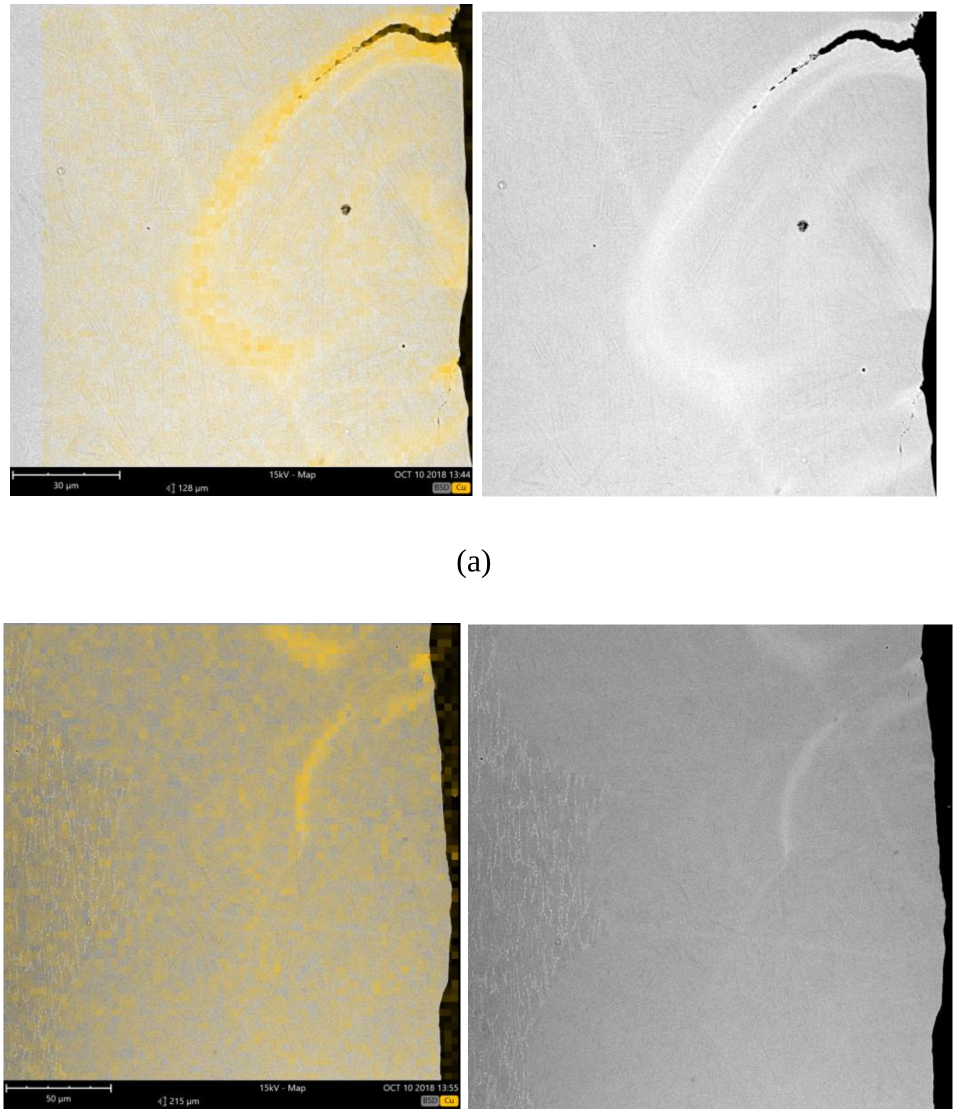

(a)

(b)

Figure 82. EDS map (left) and BSE images (right) for cross-section of Ti6Al4V-3at.% Cu single layer at 170 W and 0.8 m/s scanning speed: (a) cracks presented and (b) without cracks

4.2.3. Ti6Al4V-3at.% Cu 3D samples characterisation

3D samples were built at 170 W laser power and scanning speeds of 0.7-1.2 m/s. The first two samples at 170 W laser power and 1.0 m/s and 1.2 m/s scanning speed were produced without rescanning of the first layer, resulting in inhomogeneity and high residual stress, which lead to high porosity at the bottom part of the samples; these samples were separated from the substrate without difficulty (Figure 83a). For experiments at 0.7-0.9 m/s 170 W and 1.0-1.2 m/s 340 W, the substrate was scanned before the initial powder layer followed by rescanning of the first layer, this eliminated the substrate-sample bonding problem *i.e.* samples had good metallurgical contact with the substrate (Figure 83 b,c). Since the substrate of the next layer is the previous sintered layers, porosity and homogeneity in 3D samples is different from the single layer, especially for *in-situ* alloyed materials. Roughness measured for 170 W samples at 0.4-1.2 m/s and 340 W at $V = 0.8$-1.2 m/s was low (Figure 78), but attached particles from spatter formation can be a reason for higher porosity, which was found at P = 170 W 1.2 m/s samples (Figure 84).

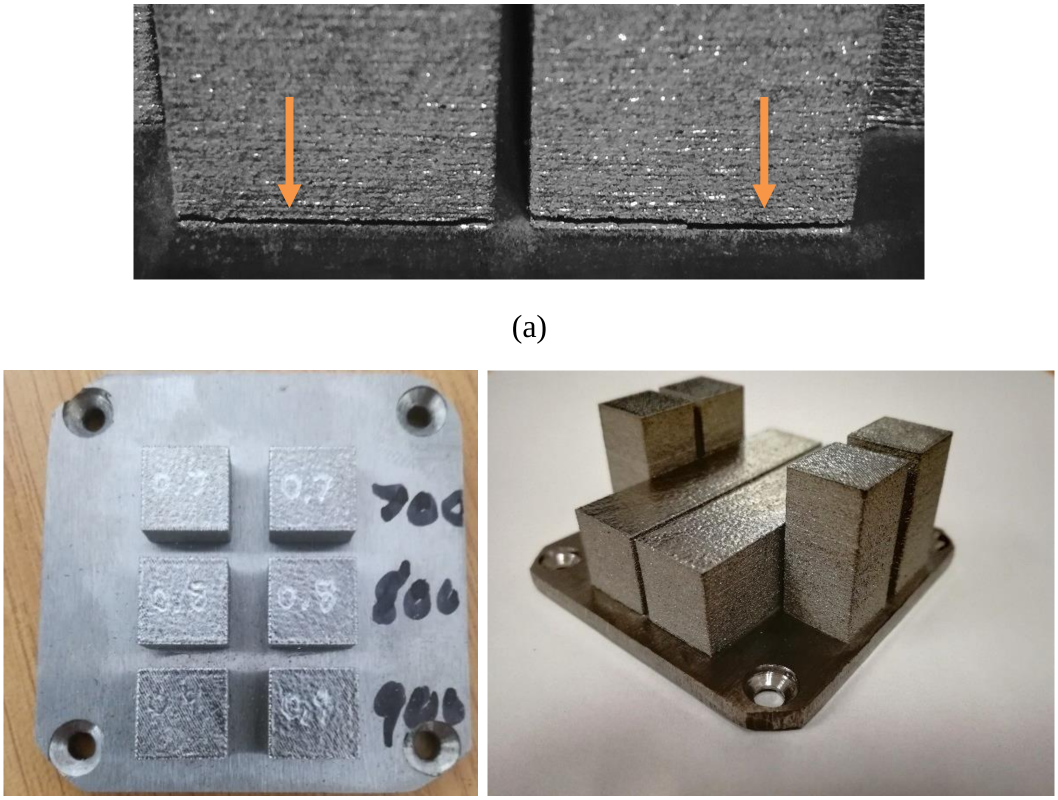

(a)

(b) (c)

Figure 83. Ti6Al4V-3at.% Cu samples produced at 170 W and 1.0-1.2 m/s (a), substrate with samples at V=0.7-0.9 m/s (b) and horizontal and vertical blocks for compression tests produced at 170 W and 0.7 m/s (c)

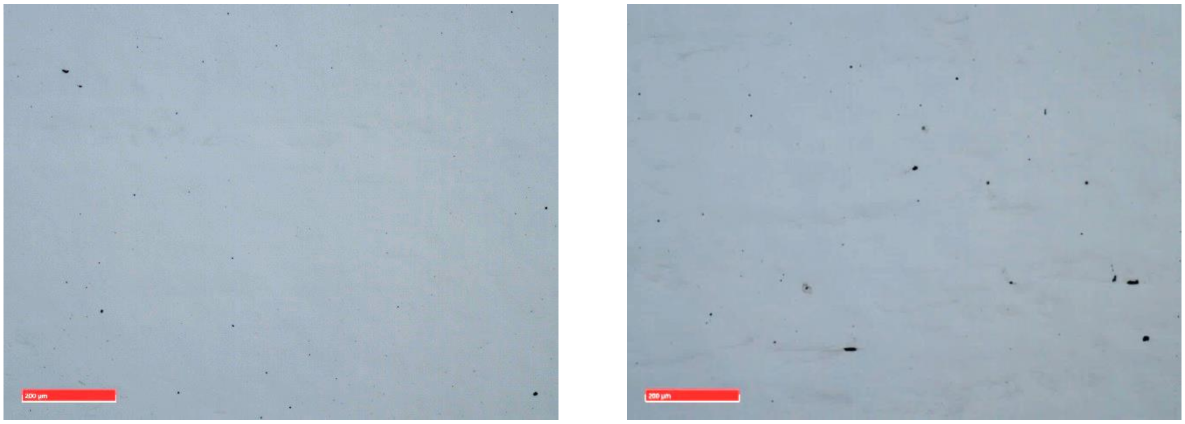

0.7 m/s 0.8 m/s

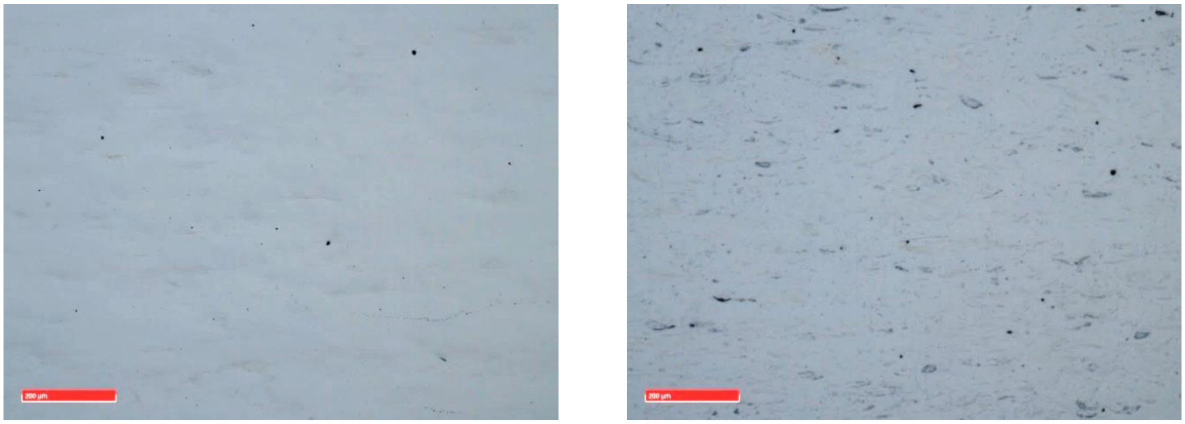

0.9 m/s 1.0 m/s

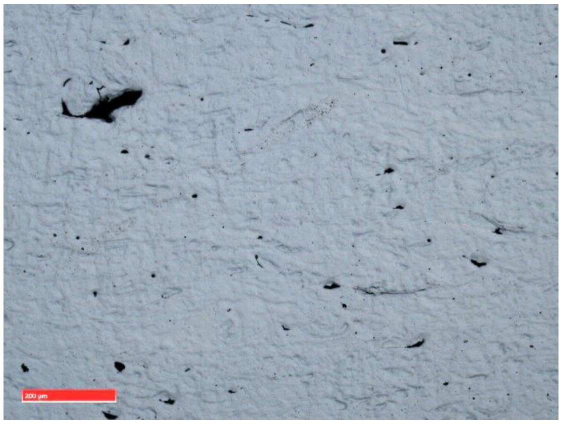

1.2 m/s

Figure 84. Cross-sections of the central part of 3D Ti6Al4V-3at.% Cu samples produced at 170 W. Samples at 0.7-0.9 m/s are shown in non-etched condition; cross-sections of the samples at 1.0 m/s and 1.2 m/s were etched by Kroll's reagent

Samples produced at 340 W also had low porosity (Figure 85). Pores had spherical shape and look like metallurgical pores – in general, they were round and small (du Plessis *et al.*, 2018a).

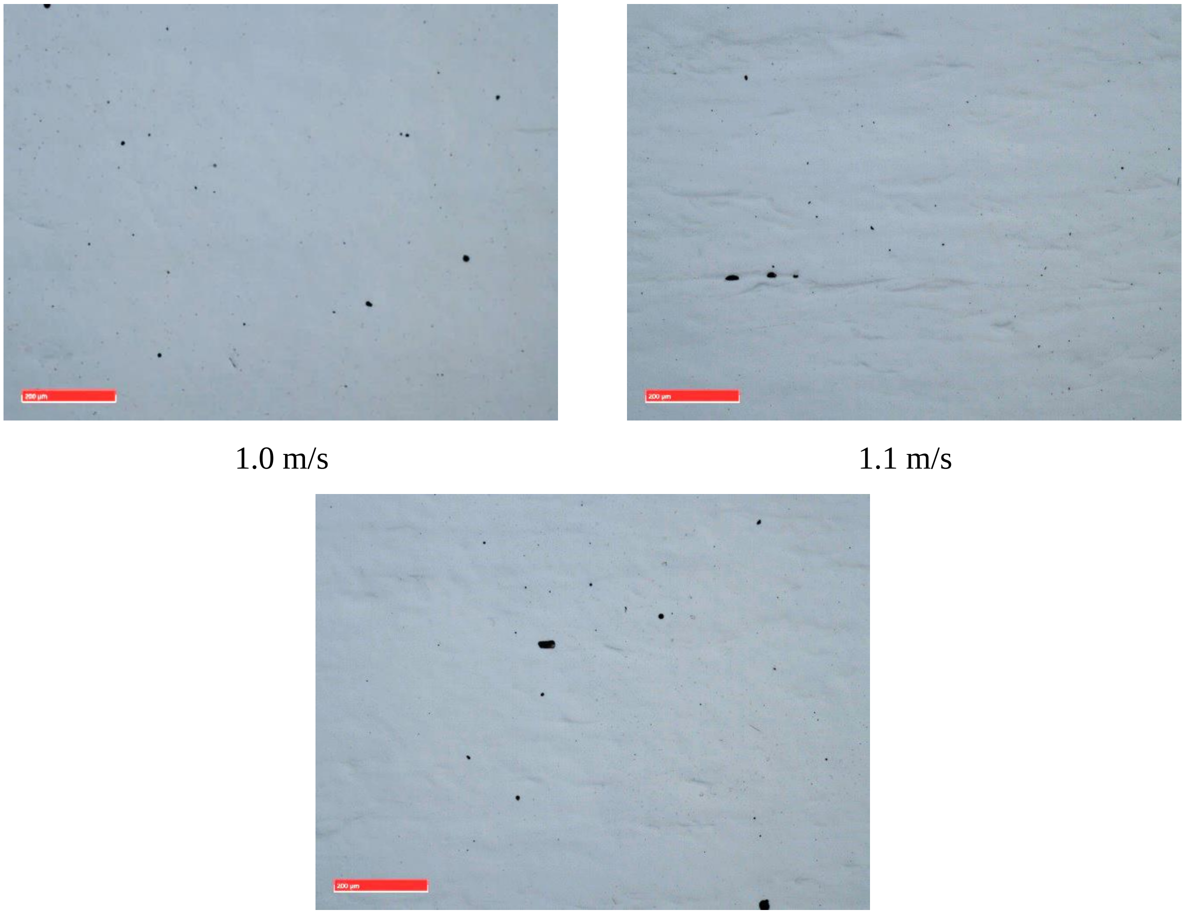

1.0 m/s

1.1 m/s

1.2 m/s

Figure 85. Non-etched cross-sections of the central part of 3D Ti6Al4V-3at.% Cu samples produced at 340 W

The microstructure of dense Ti6Al4V-3at.% Cu samples produced at 170 W, 0.7 m/s and 340 W and scanning speed of 1.0 m/s are shown in Figure 86. One set of the samples was cross-sectioned; the second set of samples were sent to CT scans for porosity analysis.

Typical for LPBF Ti6Al4V prior beta grains and columnar growth was found. In comparison with LPBF Ti6Al4V sample, martensitic structure was less pronounced; layer structure can be recognised easily (Figure 87).

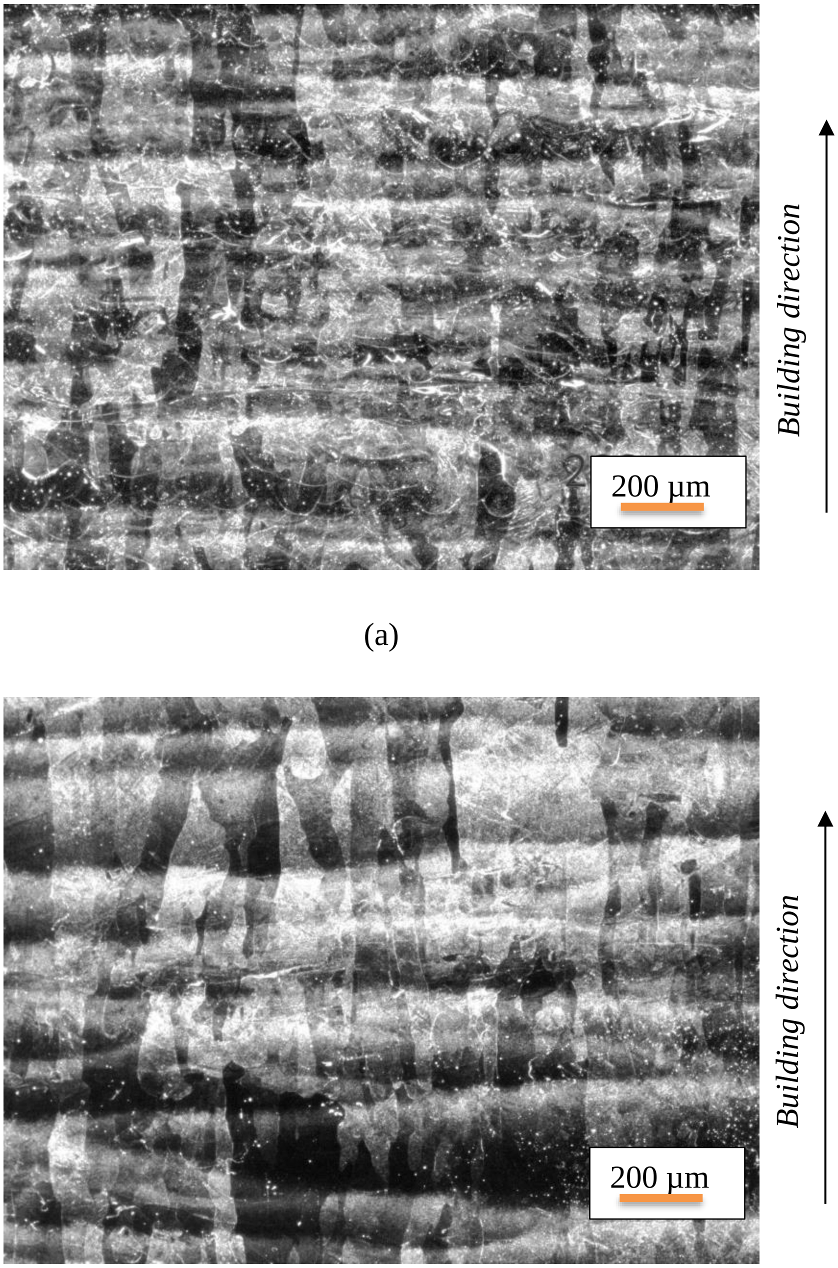

(a)

(b)

Figure 86. Microstructure of Ti6Al4V-3at.% Cu samples produced at 170 W and 0.7 m/s (a); 340 W and 1.0 m/s (b), dark field view

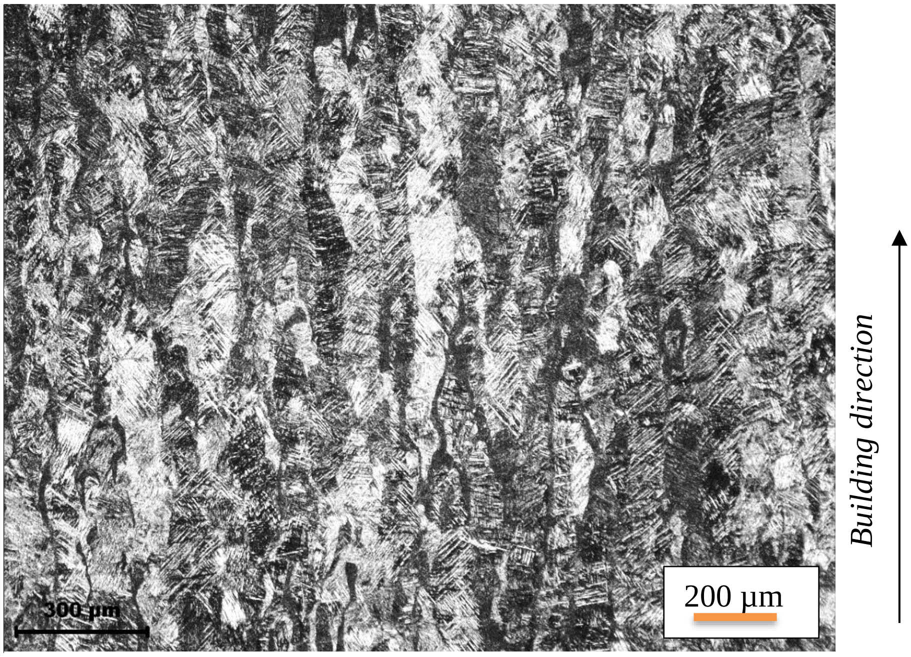

Figure 87. Microstructure of as-built Ti6Al4V ELI sample produced at 170 W and 1.2 m/s (dark field view)

Under higher magnification of etched samples martensitic microstructure specific for LPBF titanium alloys were found. Also the tracks' structure was visible (Figure 88), most likely because the edges of the tracks were enriched with copper, but this assumption has to be confirmed by EDS analysis and comprehensive analysis of the microstructure using SEM technology under higher magnification.

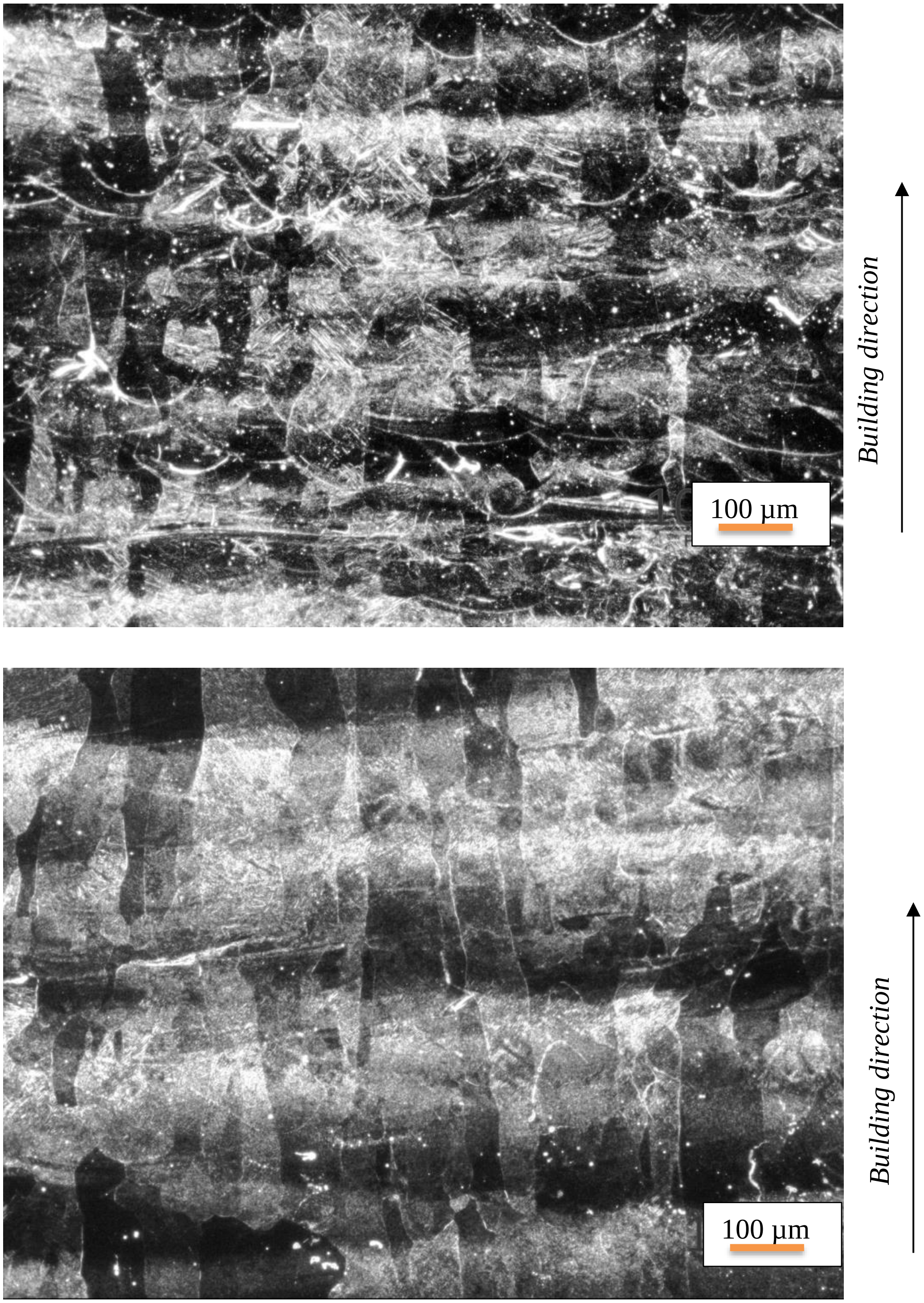

Figure 88. Microstructure of Ti6Al4V-3at.% Cu samples produced at 170 W and 0.7 m/s (a) and 340 W and 1.0 m/s at higher magnification (dark field view)

CT scans were performed at Stellenbosch University by Prof. A. du Plessis using parameters described in du Plessis *et al*. (2018b) modified for Ti-Cu alloy, Figure 89-Figure 90.

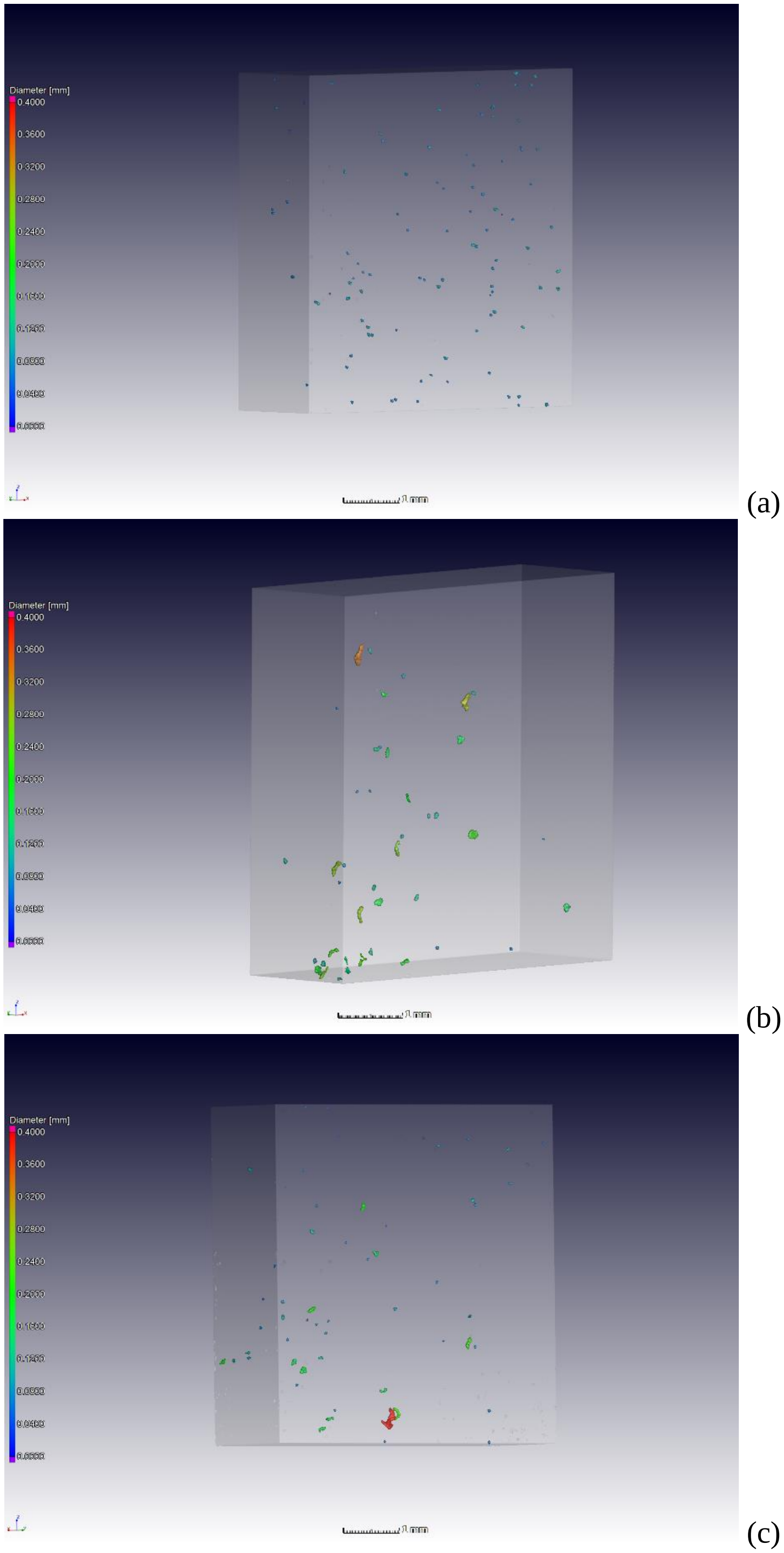

Figure 89. Porosity reconstruction by CT scans of Ti6Al4V-3at.% Cu samples produced at 170 W and 0.7 m/s (a), 0.8 m/s (b) and 0.9 m/s (c). Building direction is Y axis

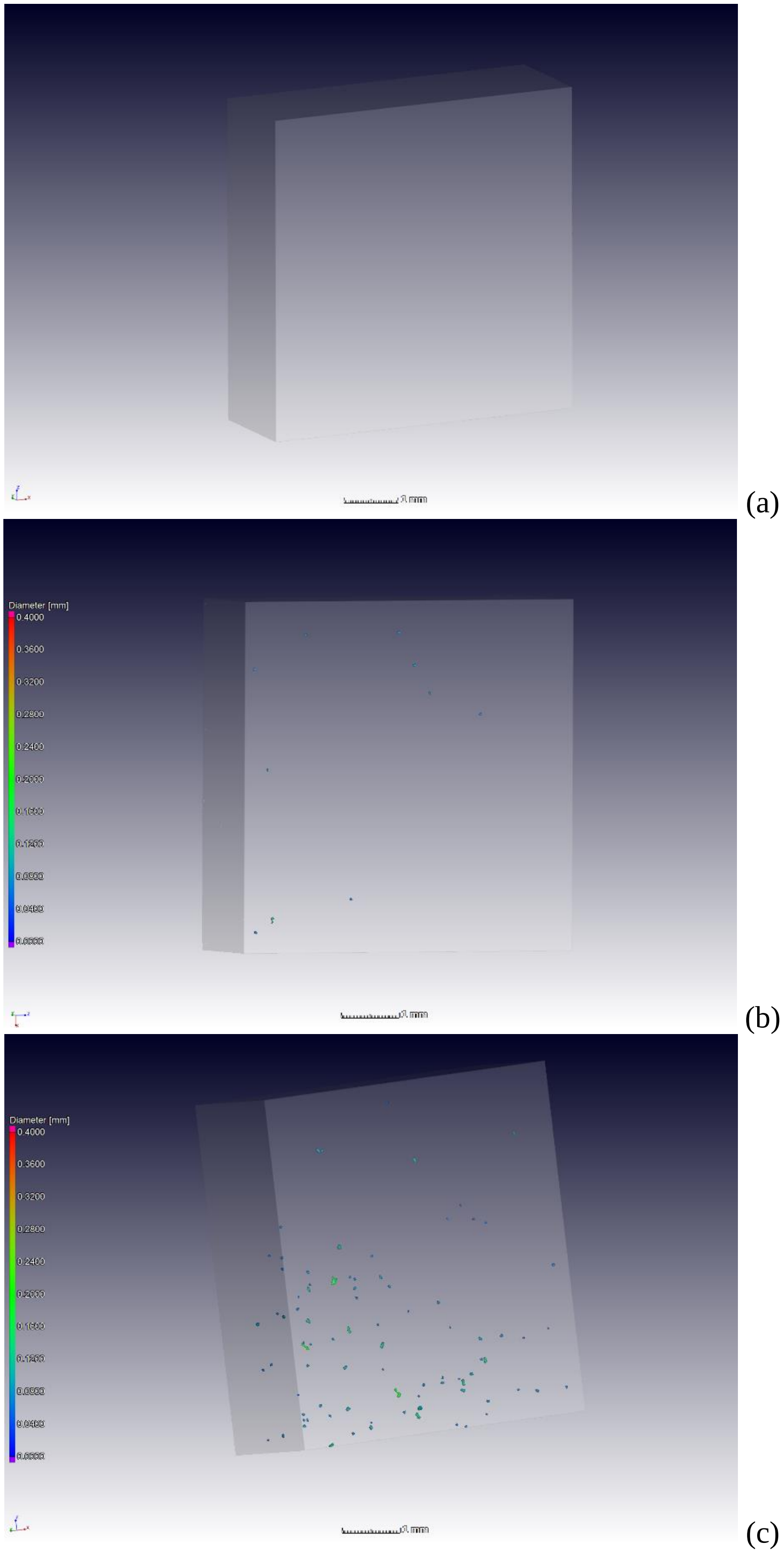

Figure 90. Porosity reconstruction by CT scans of Ti6Al4V-3at.% Cu samples produced at 340 W and 1.0 m/s (a), 1.1 m/s (b) and 1.2 m/s (c). Building direction is Y axis

Maximum pore size of approximately 400 µm was found at the bottom part of the sample that was produced at 170 W and 0.9 m/s. The defect ratio of porosity was less than 0.017% for all samples. There were no pores found in CT scans for samples produced at 340 W and 1.0 m/s. For 170 W laser power, 0.7 m/s scanning speed showed the least number of pores (Table 7).

Table 7. Defect analysis of Ti6Al4V-3at.% samples by CT scans

Sample	Diameter		Porosity statistics		
	Minimum (mm)	Maximum (mm)	Material volume (mm^3)	Defect volume (mms^3)	Defect ratio (%)
Scanning speed	**170 W laser power**				
0.7 m/s	0.0490	0.1061	71.9878	0.0082	0.0114%
0.8 m/s	0.0532	0.3437	71.9879	0.0119	0.0165%
0.9 m/s	0.0490	0.3952	71.9072	0.0089	0.0124%
340 W laser power					
1.0 m/s	0.0000	0.0000	0.0000	0.0000	0.0000%
1.1 m/s	0.0628	0.1122	71.9561	0.0007	0.0010%
1.2 m/s	0.0489	0.2007	71.9900	0.0072	0.0099%

Summary

Continuous single tracks were observed at investigated scanning speeds with 170 W laser power, while expressed balling effect started at laser power 340 W and scanning speed 1.6 m/s. Keyhole mode with pores inside the tracks was observed at 170 W and low scanning speed of 0.4 m/s. Cross-sectioning revealed deep penetration (170-220 µm) without porosity for 170 W at 0.6 m/s, and 340 W at 0.8 m/s. In order to provide better homogeneity of single layers and to eliminate satellites, the hatch distance was chosen at 80 µm which is less than that for Ti6Al4V powder (100 µm). In single layers, lower scanning speeds provoked porosity from keyhole mode and at higher scanning speeds inter-layer porosity from balling effect occurred. Based on data from single tracks and single layers from 3D samples manufactured at a laser power of 170 W and scanning speeds of 0.7 -1.2 m/s; 340 W and 1.0-1.2 m/s, verification of porosity and homogeneity was done. Samples with higher than 99.99% density were produced at laser power 340 W and scanning speeds at 1.0-1.2 m/s; samples produced at 170 W at 0.7-0.9 m/s showed 99.98% density. Samples very close to 100% dense were manufactured at 340 W and 1.0 m/s. Copper distribution and microstructure analysis, as well as mechanical testing will be done at a later stage.

4.3. Ti6Al4V -5at.% Cu samples

4.3.1. Single tracks at different process parameters

Morphology of single tracks depends on the laser power and scanning speed. Balling effect started at 1.2-1.4 m/s for 170 W and at 1.6 m/s for 340 W (Figure 91). Similar results were found for pure Ti6Al4V ELI powder without copper addition; at 45 µm powder layer, balling effect started for 170 W laser powers and spot size of about 100 µm at scanning speeds above 1.4 m/s (Yadroitsava *et al.*, 2015).

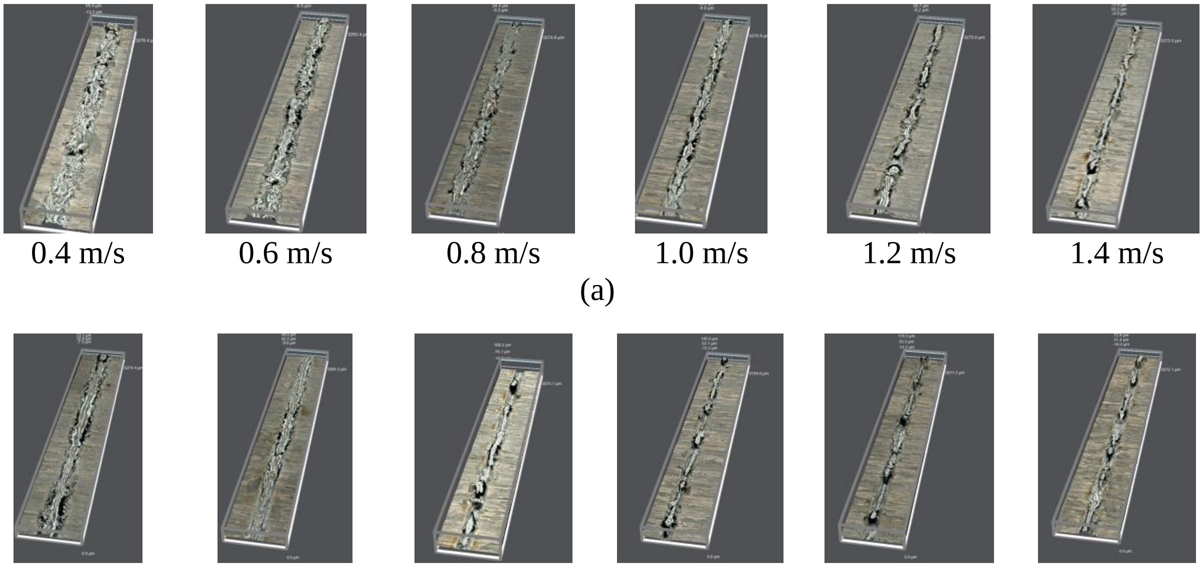

0.4 m/s 0.6 m/s 0.8 m/s 1.0 m/s 1.2 m/s 1.4 m/s

(a)

0.8 m/s 1.2 m/s 1.6 m/s 2.0 m/s 2.4 m/s 2.8 m/s

(b)

Figure 91. 3D reconstruction of Ti6Al4V-5at.% Cu single tracks using SmartZoom 5 digital microscope: at 170 W (a) and 340 W (b)

Top view analysis of single tracks showed that, at a lower scanning speed of 0.4 m/s, satellites occurred at lateral sides of the tracks (Figure 92).

Figure 92. Satellites in Ti6Al4V-5at.% Cu single track at 170 W laser power and 0.4 m/s scanning speed

In terms of linear laser energy density (the ratio of laser power to the scanning speed) no significant difference was found in track width for similar laser power density (Figure 93a) which supports previous results (Yadroitsev, 2009). For 170 W, the width of the tracks varied from 108±7.9 µm at high scanning speeds and shorter interaction time (laser spot diameter divided by the scanning speed); up to 221±11.1 µm at 0.4 m/s. For 340 W laser power, the widths of the tracks were higher and it varied greatly: the standard deviation was higher for investigated scanning speeds (Figure 93b).

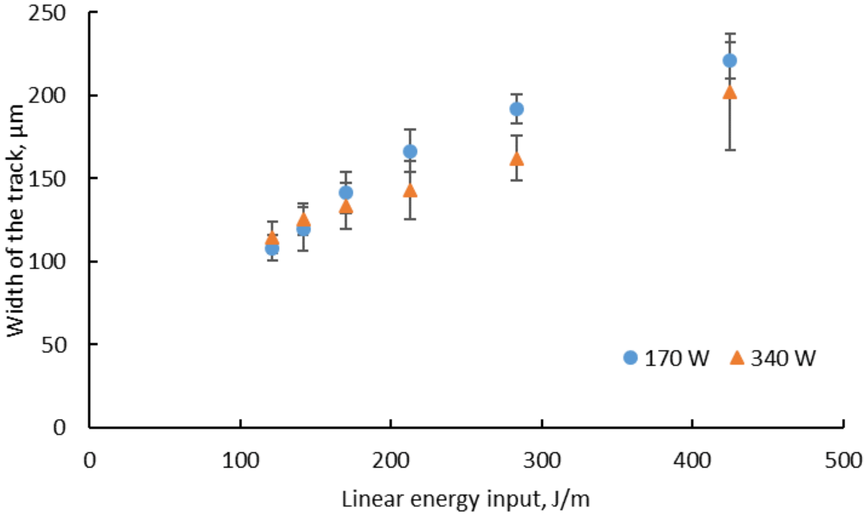

(a)

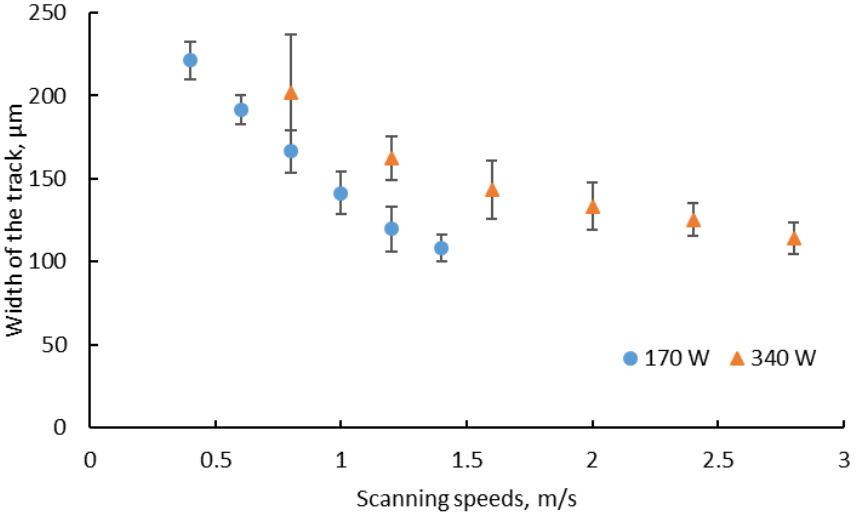

(b)

Figure 93. Width versus linear energy input (a) and scanning speeds (b) of Ti6Al4V-5at.% Cu single tracks

At 0.8 m/s, the widths of the tracks were 202±34.9 µm and 114±9.4 µm at 2.8 m/s scanning speed. The reason for very high deviation may be spattering (sparking) effect (Khairallah *et al*., 2016) and attached particles from adjusted areas trapped into molten copper that have a lower melting point. It is concluded that at higher laser power, temperature increased and spattering (sparking) effect was more prominent (Figure 94).

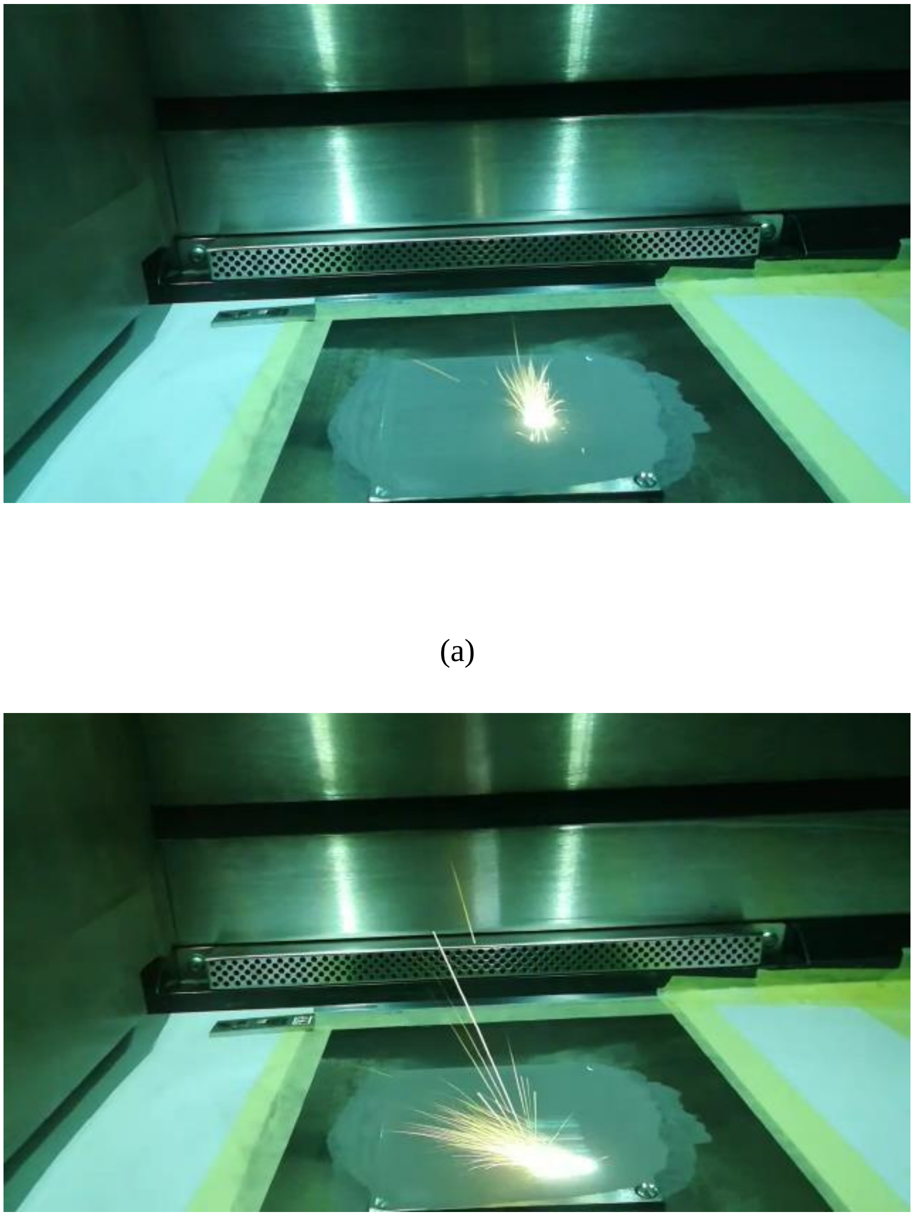

(a)

(b)

Figure 94. Sparking effect at 170 W (a) and 340 W (b) laser power for Ti6Al4V- 5at.% Cu single tracks manufacturing

As Khairallah *et al.* (2016) described, for LPBF high temperature gradients below the laser beam creates a gradient of surface tension that is largely temperature-dependent. That, in turn, creates Marangoni effects and drives the melt flow from the hot laser spot toward the cold areas. The recirculated melt flow (hence cool the location of the laser spot) leads to spattering as liquid metal with low viscosity ejects away from the surface. Liquid build-up (or "bow wave") leads to spattering. The high vapor surface flux (or "gas plume") exerts a pressure force that ejects liquid metal. When the liquid metal elongates, it thins out and breaks up into small droplets due to surface tension tendency to minimize surface energy. The elongation is in the radial direction to the laser spot and pointing away from the melt pool. Thus, sparking and humping effects explain the larger variation track width at higher laser power. Cracks were not found in the tracks when analyzed by SEM (Figure 95). Studying the profile of single tracks showed that 340 W tracks at scanning speeds 0.8-1.2 m/s had a smoother surface and less ripples were found than at the 170 W tracks (Figure 96) similar to 3at.% Cu samples.

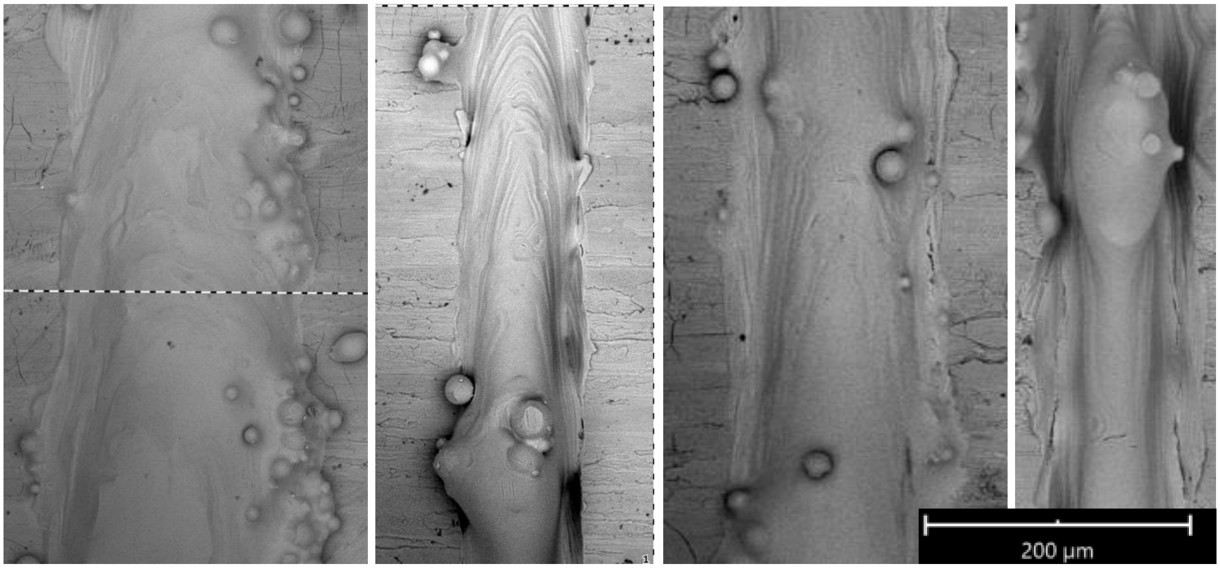

(a) (b) (c) (d)

Figure 95. SEM photos with BSE of tracks Ti6Al4V- 5at.% Cu at 170 W (a, b) and 340 W (c, d) laser power and 0.4 m/s (a), 1.4 m/s (b), 0.8 m/s (c) and 2.8 m/s (d) scanning speeds

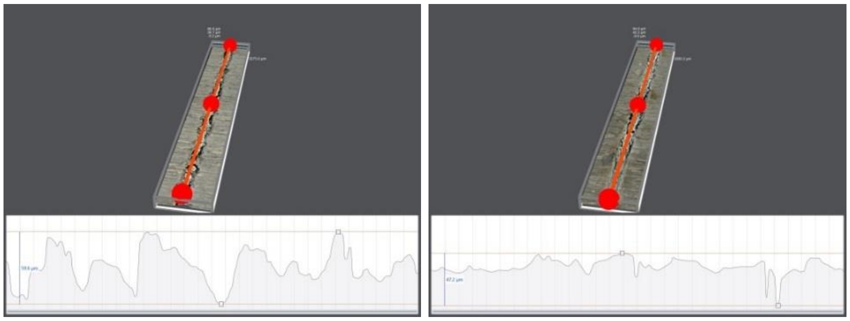

(a) (b)

Figure 96. Profiles in the centre of tracks Ti6Al4V- 5at.% Cu at 1.2 m/s scanning speed, 170 W (a) and 340 W (b)

Analysis of cross-sections perpendicular to the scanning direction of single tracks were done to estimate LPBF melting mode and penetration depth of the molten pool (Figure 97).

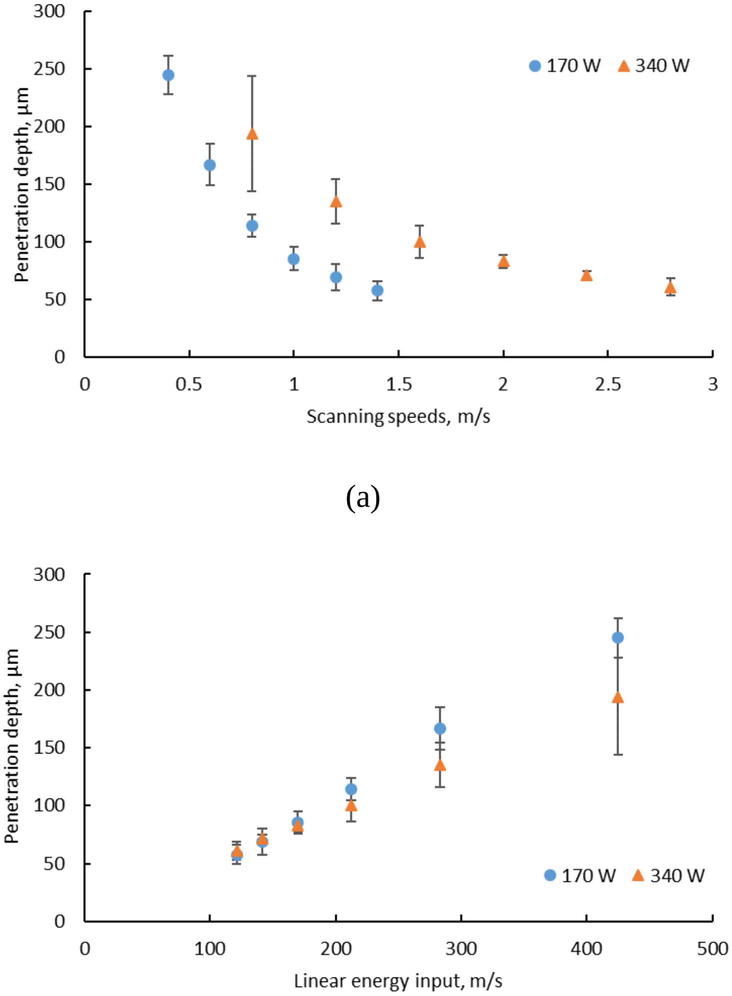

(a)

(b)

Figure 97. Penetration depth of Ti6Al4V- 5at.% Cu tracks versus scanning speeds (a) and linear energy inputs (b)

Analysis of the cross-sections revealed that keyhole mode of laser melting was at 170 W and 0.4-0.6 m/s and for 340 W laser power at 0.8 m/s (Figure 98-Figure 99). High laser power lead to high temperatures and when the absorbed energy was sufficient to cause evaporation of the metal, a vapour cavity enhanced the absorption. The laser beam created a very deep (V-shape) molten pool (Figure 99, *V*=0.4 m/s). For all other cases, transition or U-shape molten pool, was found. Conduction mode, or semi-cylindrical shape of laser melting was not observed.

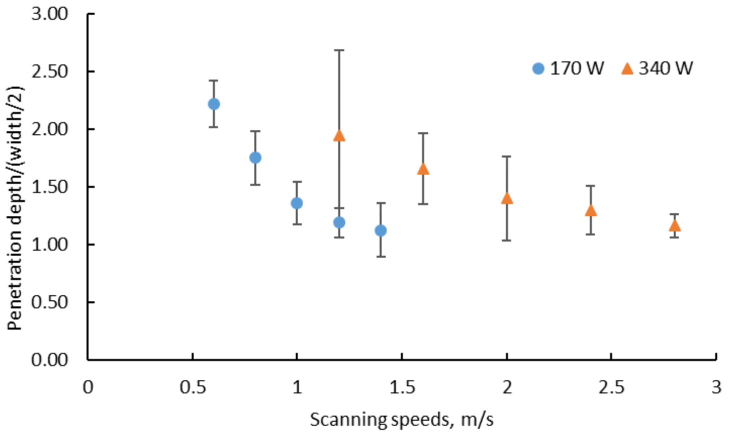

(a)

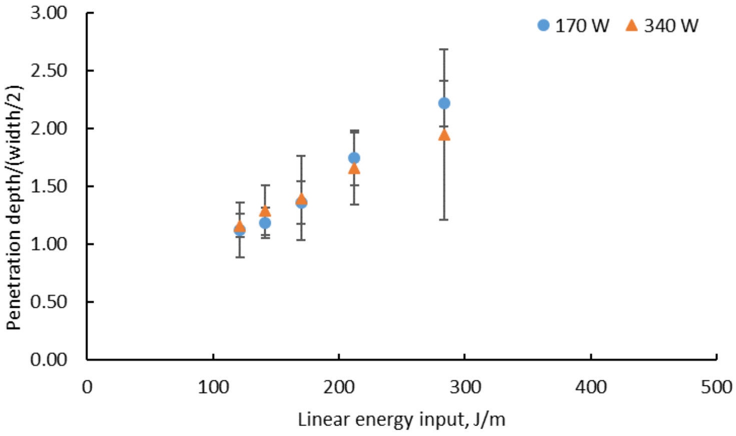

(b)

Figure 98. The ratio of penetration depth to half-width of the single track versus scanning speeds (a) and linear energy inputs (b) for Ti6Al4V-5at.% Cu samples

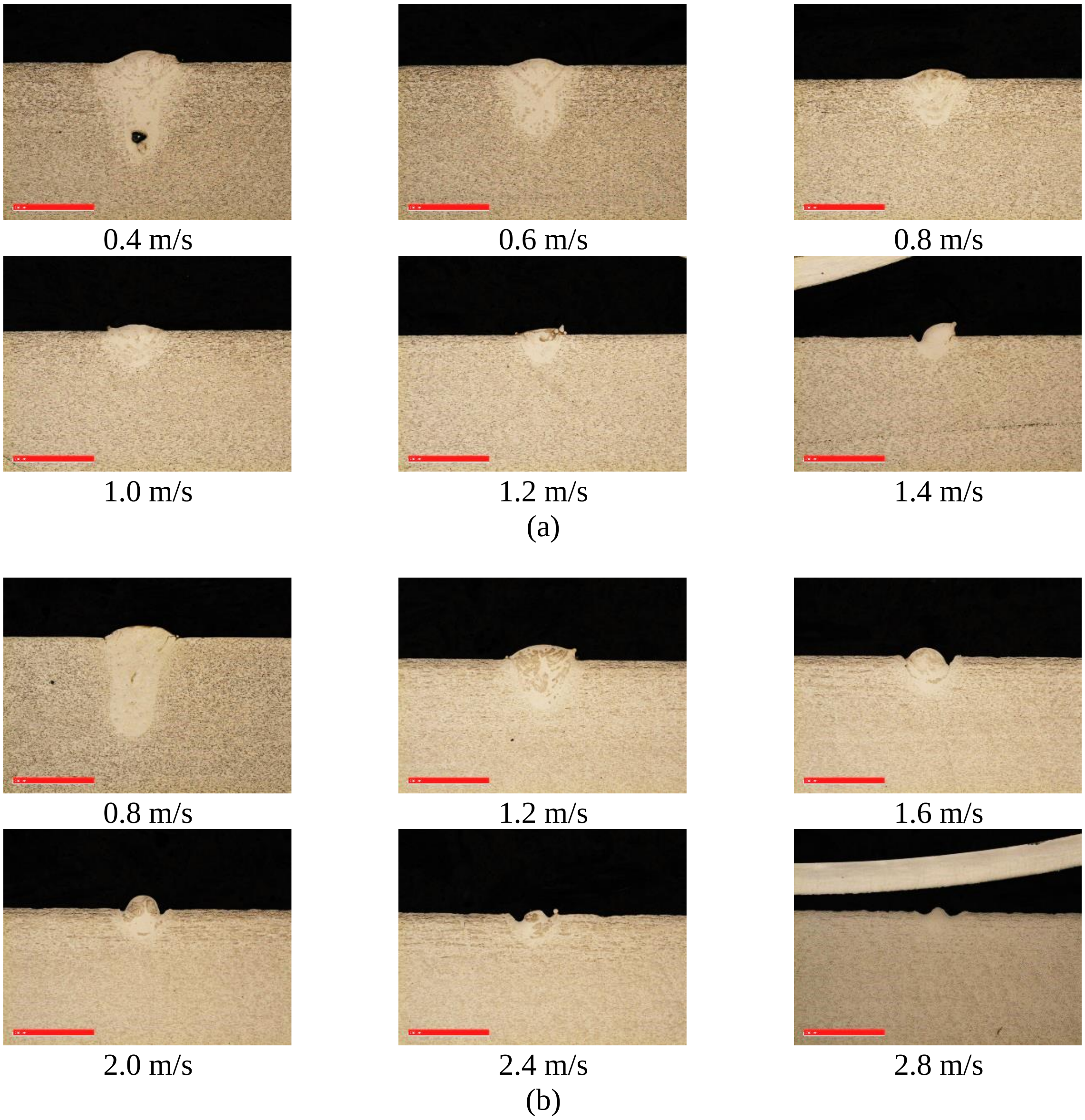

0.4 m/s 0.6 m/s 0.8 m/s

1.0 m/s 1.2 m/s 1.4 m/s

(a)

0.8 m/s 1.2 m/s 1.6 m/s

2.0 m/s 2.4 m/s 2.8 m/s

(b)

Figure 99. Cross-sections of single tracks at 170 W (a) and 340 W (b) of Ti6Al4V-5at.% Cu tracks

When a single track is produced, a denudation zone develops and different amounts of powder material participated in the process (see Chapter 2.1.2). The analysis of morphology and cross-sections of single layers is required to find optimal LPBF process parameters for manufacturing non-porous and homogenous *in-situ* alloyed multi-layered objects.

4.3.2. First layer analysis

Top view images and roughness analysis of single layers revealed that layers at lower scanning speeds were very smooth (Figure 100-Figure 102). The average value of *Rz* obtained was 12±2.7 µm for 170 W and scanning speed 0.4 m/s and for 340 W and 0.8 m/s *Rz* was 14±1.9 µm. Satellites found at the edges in single tracks at 170 W and 0.4 m/s, were melted when the layer was sintered. With scanning speed, morphology of the surfaces changed; increased quality of attached particles from sparking effect and irregularity from balling effect started. After scanning speed of 1.6 m/s, surfaces were very irregular in both cases at 170 W as well as 340 W laser power. Qiu *et al*., (2015) found that the velocity of scattered melt particles generally rises with increased laser scanning speed. Similar effects were found in this study when in process video frames were analysed.

At energy inputs less than 280 J/m, it was found that surfaces were more rough at higher laser power since humping and spattering effects were more prominent at higher laser power (Yadroitsava *et al.*, 2015) (Figure 103). Andani *et al.*, (2017) indicated that the effect of spatter particle creation can deteriorate the properties of LPBF components; large spatter particles are formed and not melted with the next layer. Thus, spatter remains as a non-melted region in the part. Higher recoil pressure above the melting pool can eject a larger amount of metallic material from molten pools.

The viscosity of liquid titanium at temperatures of 1750–2050 K is 4.42 mPa × s. For pure liquid copper, the viscosity changes from 4.03 mPa × s at 1356 K to 1.96 mPa× s at 1950 K (Paradis *et al*., 2002; Assael *et al*., 2010). It can be assumed that the copper concentration can decrease in resulted solidified alloy in comparison with the initial powder mixture. The previous statement must be confirmed by analysis of a lower copper concentration in 3D sintered samples.

170 W 340 W

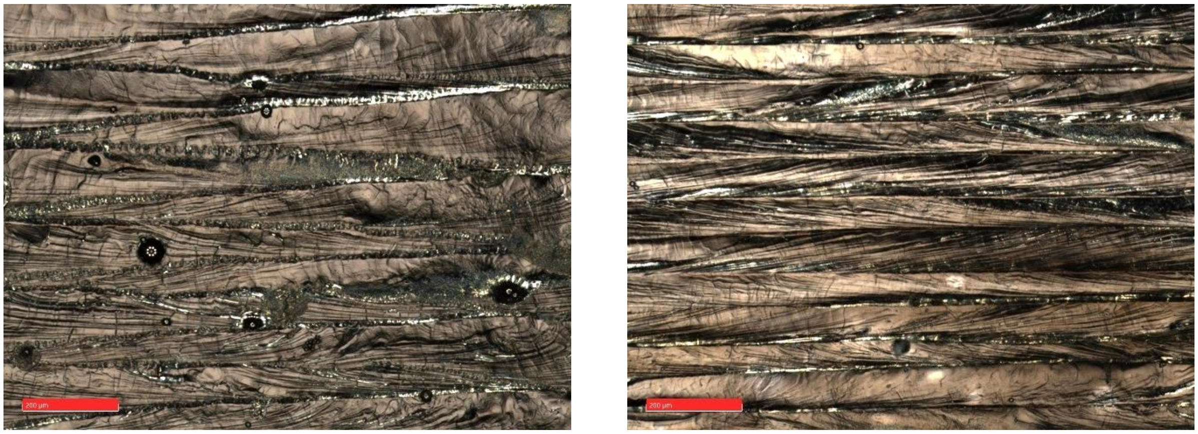

0.4 m/s 0.8 m/s

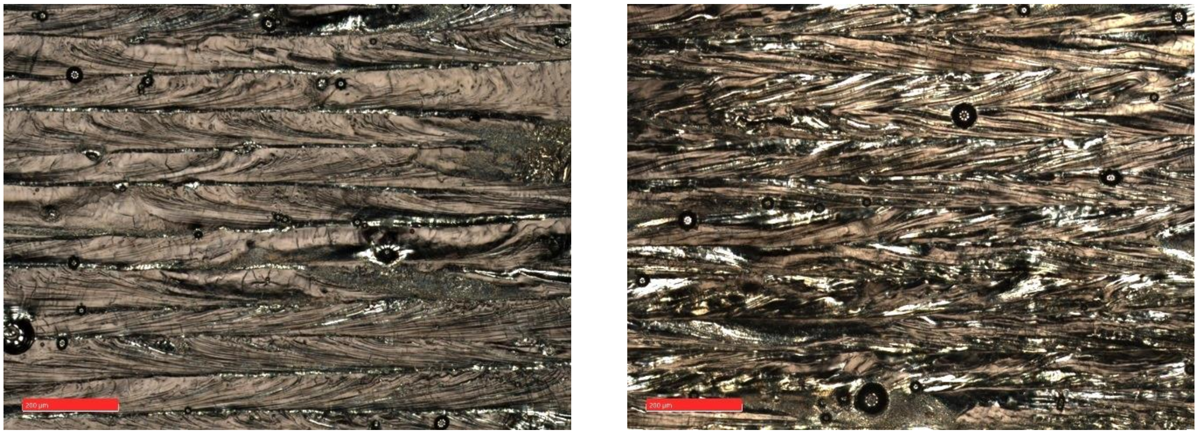

0.6 m/s 1.2 m/s

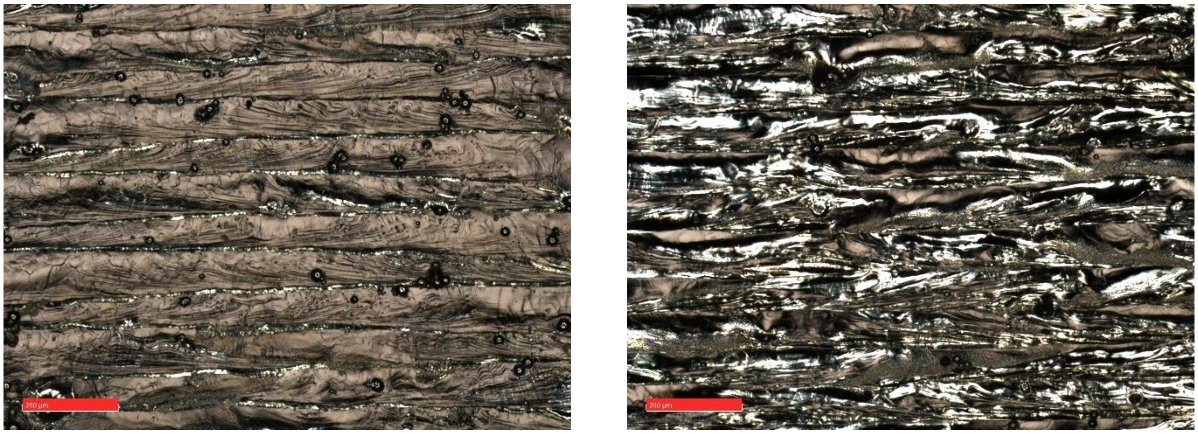

0.8 m/s 1.6 m/s

Figure 100. Top surfaces of the first layer at 170 W and 340 W and scanning speeds 0.4-1.6 m/s of Ti6Al4V-5at.% Cu samples

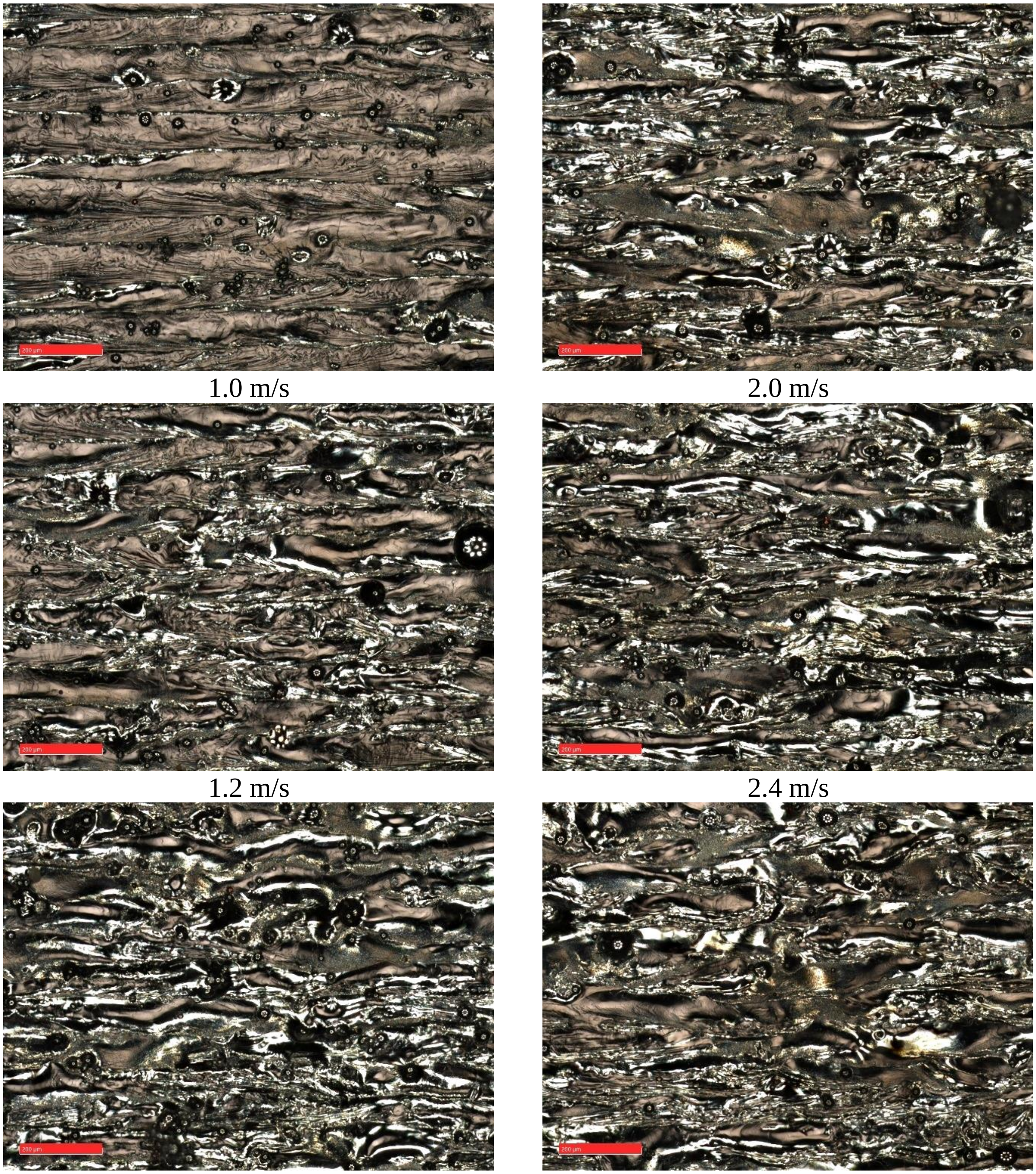

1.0 m/s

2.0 m/s

1.2 m/s

2.4 m/s

1.4 m/s

2.8 m/s

Figure 101. Top surfaces of first layer at 170 W and 340 W and scanning speeds 1.0-2.8 m/s of Ti6Al4V-5at.% Cu samples

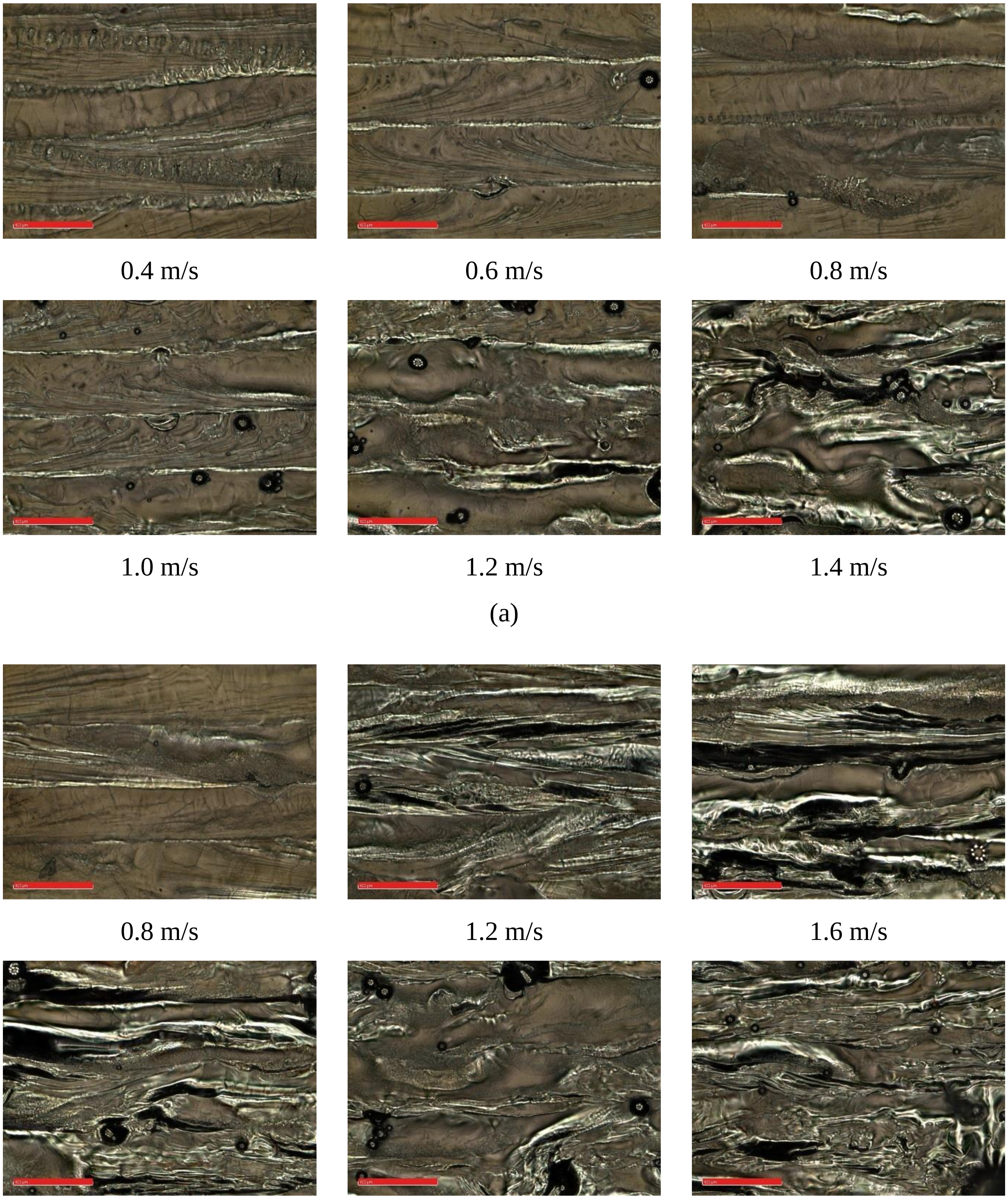

0.4 m/s

0.6 m/s

0.8 m/s

1.0 m/s

1.2 m/s

1.4 m/s

(a)

0.8 m/s

1.2 m/s

1.6 m/s

2.0 m/s

2.4 m/s

2.8 m/s

(b)

Figure 102. Top surfaces single layer at 170 W (a) and 340 W (b), 0.4-2.8 m/s scanning speeds of Ti6Al4V-5at.% Cu samples

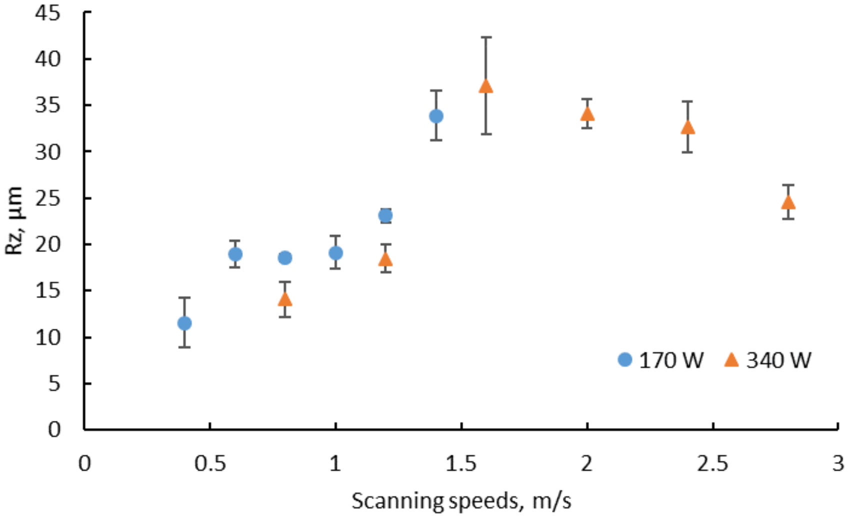

(a)

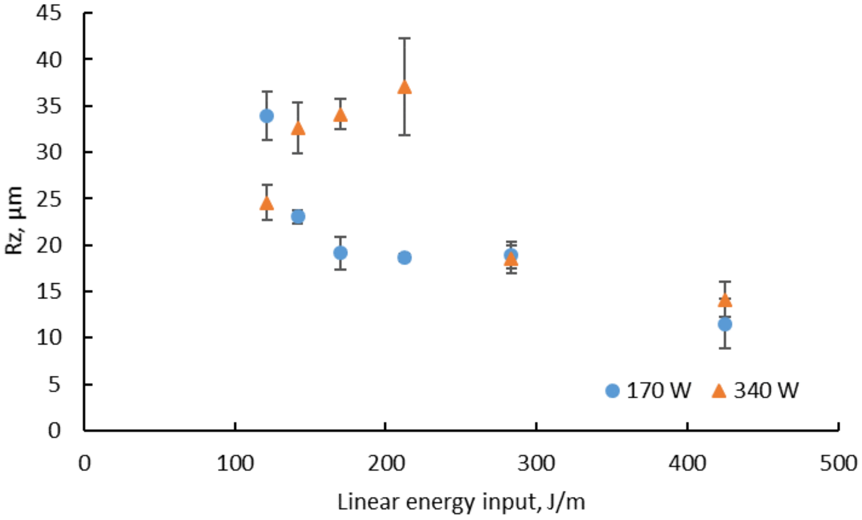

(b)

Figure 103. Surface roughness Rz of single layers at 170 W (a) and 340 W (b) versus scanning speed (a) and linear energy input (b) for Ti6Al4V-5at.% Cu samples. Roughness measured tangential to scanning direction

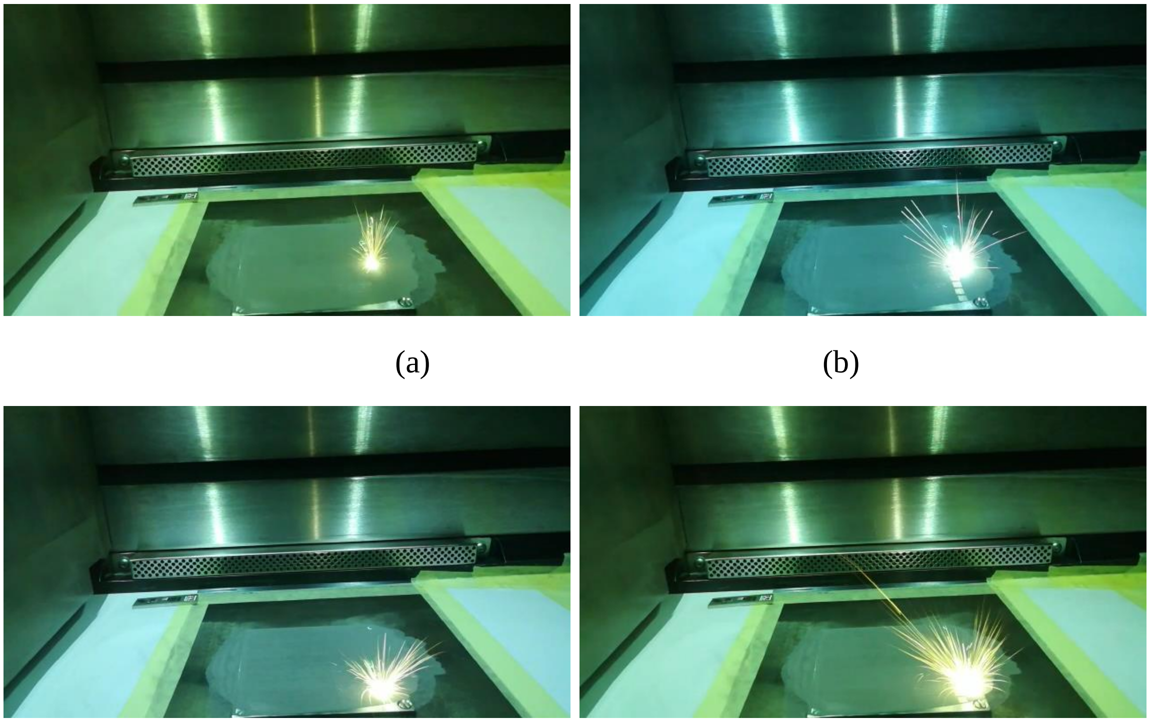

(a) (b)

(c) (d)

Figure 104. Frames from video at scanning single layer Ti6Al4V- 5at.% Cu samples at 170 W (a, c) and 340 W (b, d) at low and high scanning speeds (see chapter 3.2)

4.3.3. Characterisation of 3D Ti6Al4V-5at.% Cu samples

Taking into account the results from 3% Cu samples, a hatch distance of 80 μm was chosen for overlapping of the single tracks in 3D samples. The collapsing of the created cavity in keyhole mode can leave voids in the solidified material which were clearly visible in cross sectioned analysis of 3D samples (Figure 105). It must be noted that large pores were produced in the 170 W samples (Figure 105a). At lower laser power the collapse of the keyhole happened quicker and created bubbles which did not have enough time to reach the melt pool surface before solidification. Higher laser power led to a higher temperature and, respectively, lower viscosity of the molten pool which facilitates gas bubbles to escape to the surface of the molten pool. The walls of the capillary are unstable and oscillating in keyhole mode during laser welding and the formation of porosity is very sensitive to the shape of the molten pool at the laser end position (Courtois, 2014). In LPBF, similar phenomena were found (Yadroitsava *et al*., 2015). Since small perturbations in the process can cause porosity from LPBF samples during keyhole mode, process parameters such as 0.4–0.6 m/s, 170 W and 0.8 m/s at 340 W with a powder layer thickness about 50 µm cannot be considered as optimal process parameters for this *in-situ* alloyed material.

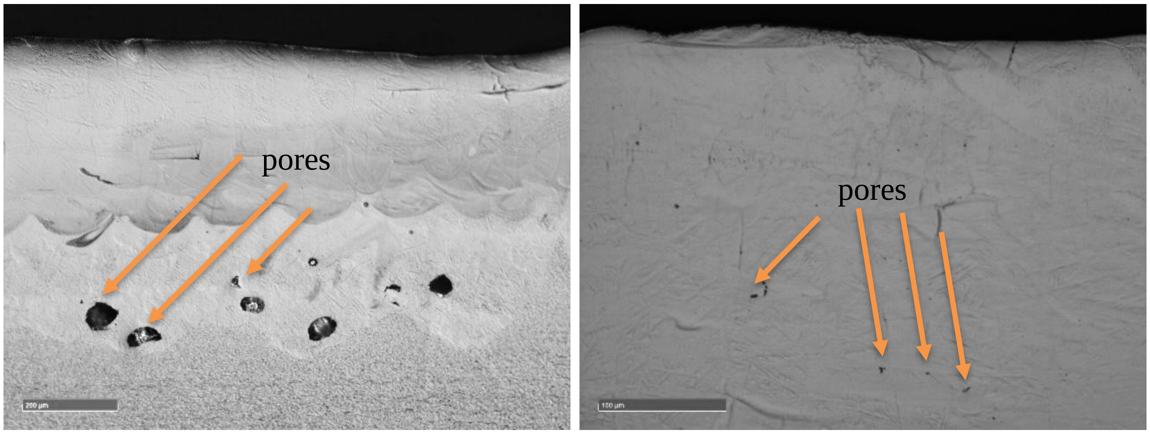

(a) (b)

Figure 105. Etched by Kroll's reagent cross-sections of 10 layer Ti6Al4V- 5at.% Cu samples at 170 W, 0.4 m/s (a) and 340 W at 0.8 m/s (b)

As it has been shown earlier by Yadroitsev (2009) and Tucho (2018), balling effect provoked porosity in 3D samples. Large pores were found in 3D samples processed at 170 W and 1.4 m/s. Unfused powder particles are clearly visible in the cross-section (Figure 106a). Interlayer pores were also found at 340 W laser power when scanning speeds were above 1.6 m/s and balling effect occurred (Figure 106b).

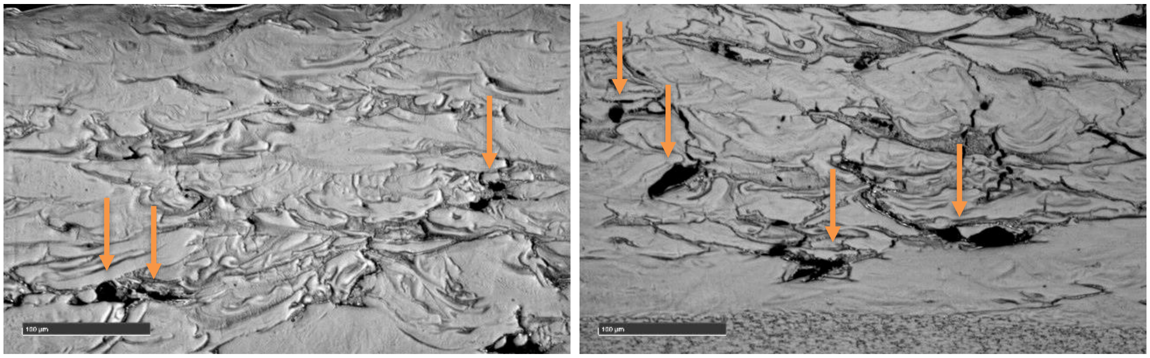

(a) (b)

Figure 106. Etched by Kroll' reagent cross-sections of 10 layer Ti6Al4V- 5at.% Cu samples at 170 W, 1.4 m/s (a) and 340 W and 2.4 m/s (b)

At a hatch distance of 80 µm and laser power 170 W with scanning speed 0.8-1.0 m/s as well as 340 W and scanning speed of 1.2 m/s, non-porous 10 layer samples were formed (Figure 107).

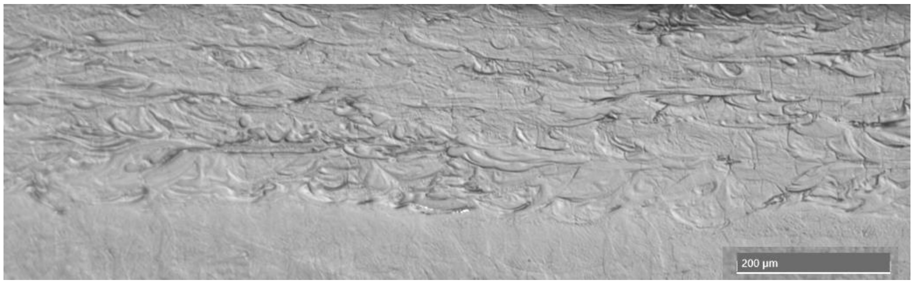

(a)

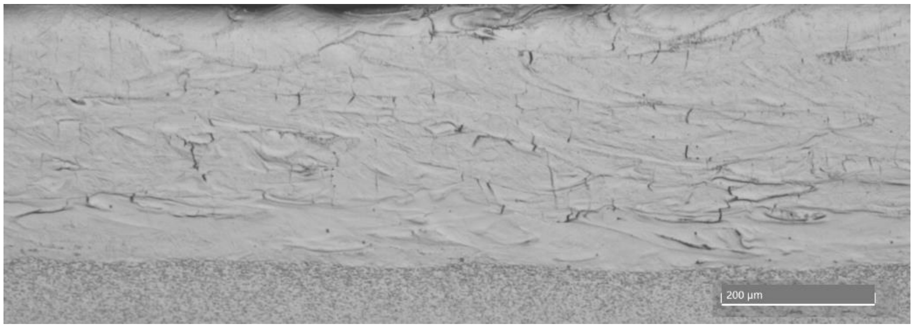

(b)

Figure 107. Cross-sections of 10 layer Ti6Al4V- 5at.% Cu samples (etched by Kroll's reagent) at 170 W and 0.8 m/s (a) and 340 W and 1.2 m/s (b). Images by optical microscope.

Distribution of elements in the 10-layer samples were not always perfectly homogeneous (Figure 108). According to SEM EDS, a gradient zone, where the substrate contributed in the chemical composition of the coatings started at 200-250 µm in depth (Figure 109). Point chemical analysis showed that variations of copper are present within the layer. For example, areas with about 25 wt.% Cu and 15 wt.% Cu were observed in specimens manufactured at 170 W and 1.0 m/s, and 340 W and 2.0 m/s respectively.

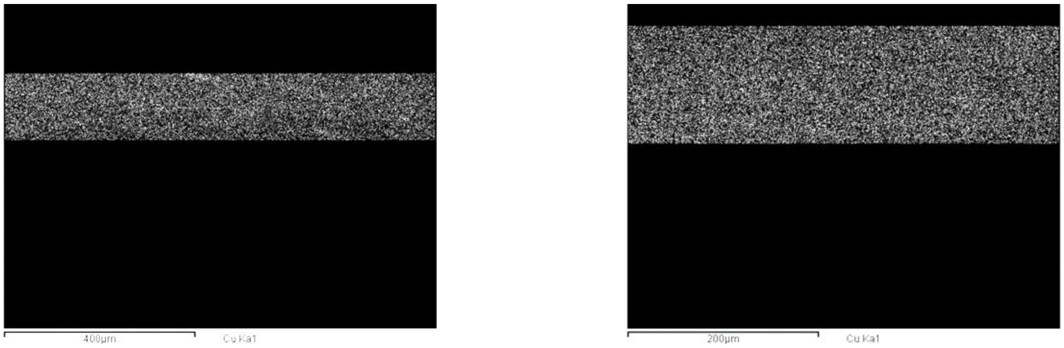

170 W, 0.4 m/s

340 W, 0.8 m/s

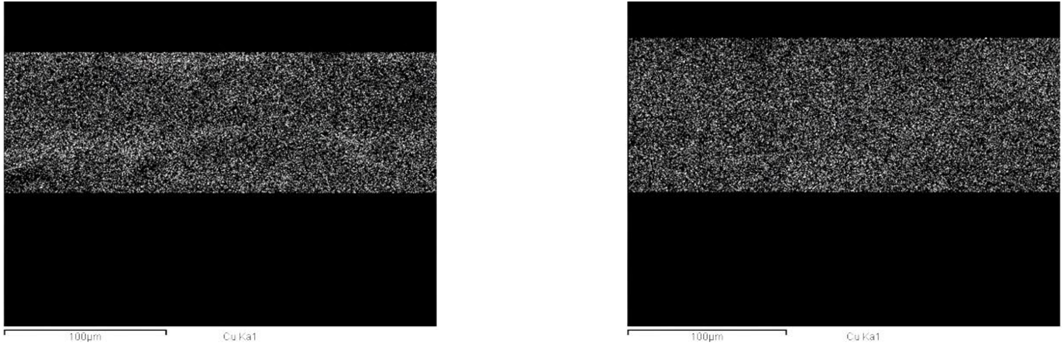

170 W, 0.8 m/s

340 W, 1.6 m/s

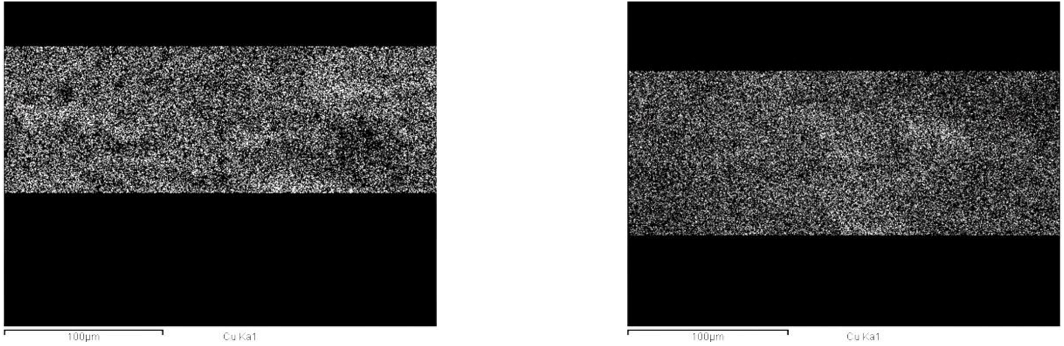

170 W, 1.0 m/s

340 W, 2.0 m/s

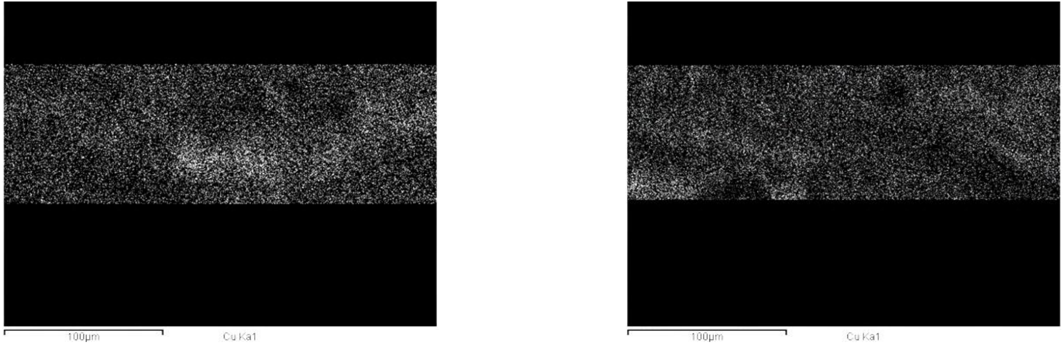

170 W, 1.4 m/s

340 W, 2.4 m/s

Figure 108. SEM–EDS elemental mapping of Cu at different process parameters in Ti6Al4V- 5at.% Cu samples

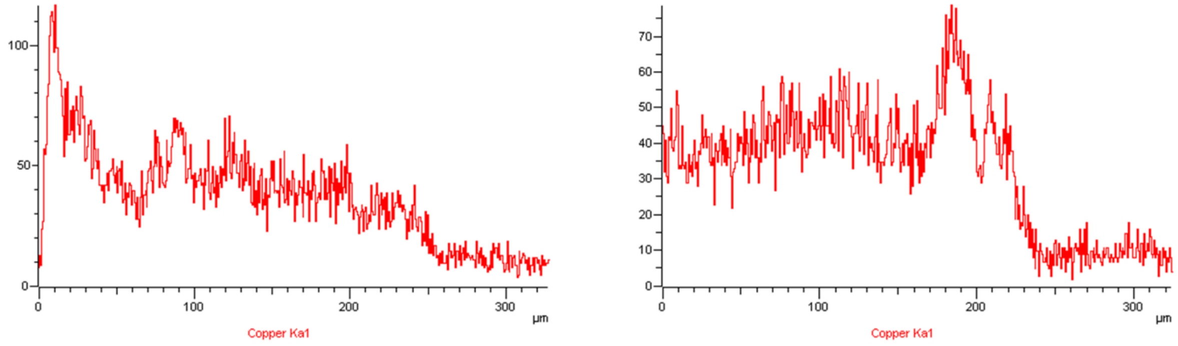

170 W, 0.8 m/s

340 W, 1.6 m/s

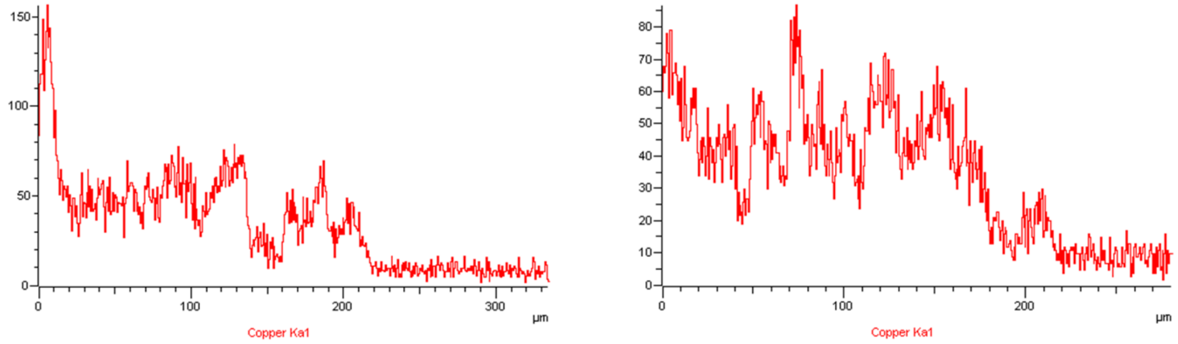

170 W, 1.0 m/s

340 W, 2.0 m/s

Figure 109. EDS spectrum of Cu at the different laser powers (X axis – distance from the top surface, Y axis – a.u.), Ti6Al4V- 5at.% Cu samples

The most homogeneous specimens were manufactured at 170 W and 0.4 m/s and 340 W and 0.8 m/s (Figure 110). However, those specimens contained porosity and were manufactured in a keyhole regime. Higher energy input has positive effect on the homogeneity of the elements; this could be ascribed to fluid flow caused by higher temperature gradients and the remelting of previous layers due to the large penetration depth (approximately 4 times powder layer thickness).

No unmolten copper particles were observed in any specimens. Some round particles observed on etched cross sections were, according to the EDS observations, unmolten particles of Ti6Al4V alloy as shown in Figure 111.

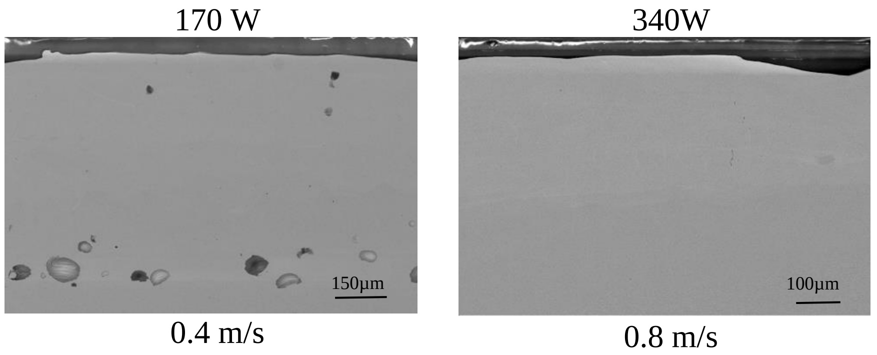

Linear energy input (P/V) 425 J/m

(a)

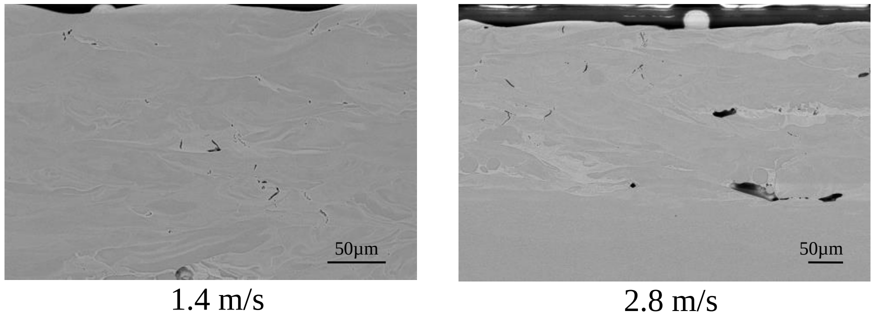

Linear energy input (P/V) 121 J/m

(b)

Figure 110. Comparison between maximum and minimum energy input at the different laser powers. BSE images from SEM of Ti6Al4V- 5at.% Cu samples

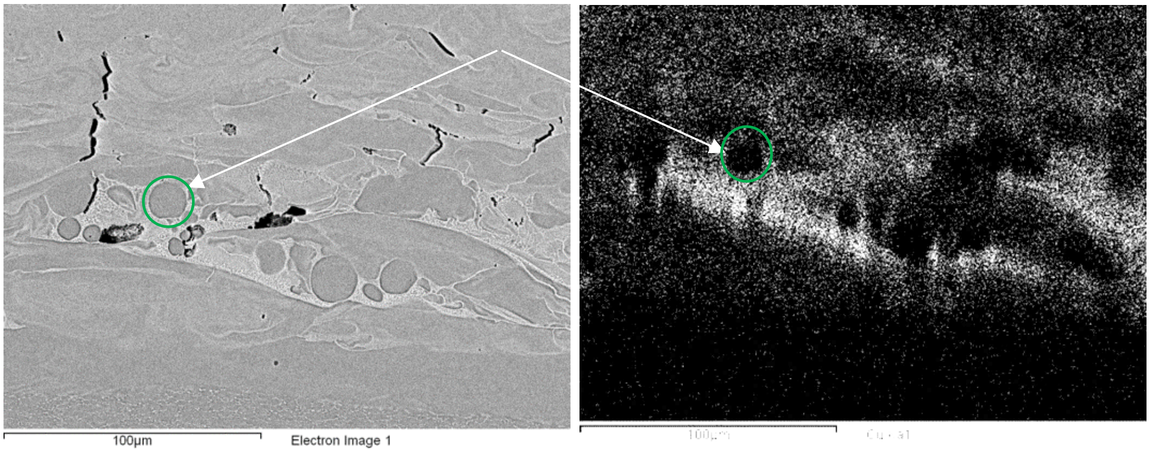

(a) (b)

Figure 111. EDS observations of unmolten Ti6Al4V alloy particles at 340 W and 2.8 m/s (indicated by arrows). SEM image (a) and inhomogeneous copper distribution in white (b), Ti6Al4V- 5at.% Cu samples

Copper has a lower melting point and higher thermal conductivity, so at shorter laser-beam interaction time (high scanning speed) larger Ti6Al4V particles were partially melted; copper was completely fused and distributed at the bottom of the molten pool because it is twice as heavy as the titanium alloy. Possibly due to volatilization, the concentration of copper, compared to the nominal values (wt.%) of the feedstock in the specimens, was slightly lower.

Summary

Further recommended work includes investigation of the distribution of the elements in the single tracks and the effect of differing layer thickness with similar parameters (Table 8).

Table 8. Summary of findings for all parameters for Ti6Al4V-5 at.% Cu samples

170 W		340 W	
0.4 m/s	Porosity, elements homogeneous	0.8 m/s	Small porosity, elements homogeneous
0.6 m/s	Small porosity, elements homogeneous	1.2 m/s	Non-porous, elements homogeneous
0.8 m/s	Non-porous, elements slightly inhomogeneous	1.6 m/s	Small pores, elements inhomogeneous
1.0 m/s	Non-porous, elements slightly inhomogeneous	2.0 m/s	Pores, elements inhomogeneous
1.2 m/s	Unmolten Ti6Al4V, pores, elements inhomogeneous	2.4 m/s	Unmolten Ti6Al4V, pores, elements inhomogeneous
1.4 m/s	Unmolten Ti6Al4V, pores, elements inhomogeneous	2.8 m/s	Unmolten Ti6Al4V, pores, elements inhomogeneous

Chapter 5. Conclusions and future work

Ti6Al4V Extra Low Interstitial (ELI) alloy is commonly used for medical implants because of its biocompatibility and suitable mechanical- and corrosion resistant properties. Manufacturing implants from materials with antibacterial properties such as copper-bearing alloys is a promising approach to prevent infection. Copper additions at the bone–implant interface reduce the risk of bacterial infection and subsequent implant failure. The formation of *in-situ* sintered grade 23 titanium alloy (Ti6Al4V ELI) with copper by laser powder bed fusion for application in medical implants was investigated. Ti6Al4V (ELI) powder was mixed with pure copper powder of similar particle size distribution. Optimal process parameters were investigated for *in-situ* alloying of Ti6Al4V-1,3 and 5 at.% Cu to form dense parts with suitable microstructural and surface quality. The relationship between homogeneity, porosity and process parameters were studied. Overall, it was illustrated that better homogeneity is achieved at higher energy input. Addition of 1-5at.% Cu to Ti6Al4V in comparison with "pure" Ti6Al4V powder did not have a significant influence on the width of single tracks, and a slightly increased penetration depth (maximum 10%) was observed. Spatter formation and involvement of powder from adjusted areas by fused copper particles with low-melting point greatly enhanced with increasing copper content. This resulted in the appearance of satellites; enriched copper regions found near the edges of the LPBF tracks. When layers were sintered, it was shown for 1at.% Cu addition to Ti6Al4V ELI powder that rescanning improved morphology and homogeneity of LPBF layers, resulting in a doubling of the manufacturing time. During manufacturing of Ti6Al4V -3 and 5at.% Cu samples at 170 W and 340 W laser power, higher energy input resulted in improved homogeneity of the *in-situ* alloyed samples.

Recommended future work includes investigation of the distribution of the elements at higher layer thickness with similar parameters, and further fine tuning of optimal parameters. The current study showed that the process window is narrow and homogeneity of copper within this zone needs further refinement. Other approach to solve this problem is to use finer copper powder, for example with sub-micron size. Antimicrobial activity, mechanical properties and microstructure of *in-situ* alloyed Ti6Al4V-1,3,5 at.% Cu require further investigation.

References

Andani, M.T., Dehghani, R., Karamooz-Ravari, M.R., Mirzaeifar, R., Ni, J., 2017. Spatter formation in selective laser melting process using multi-laser technology. *Materials & Design*, 131, pp. 460-469.

Andrade, P.R., Contieri, R.J., Coelho, A.A., Afonso, C.R.M., Ferrandini, P.L., Caram, R., 2005. Microstructure of Ti-Cu and Ti-Nb Cast alloys for medical and dental implants. Proceeding of the *18th International Congress of Mechanical Engineering*, November 6-11, 2005, Ouro Preto.

Andreini, C., Bertini, I., Cavallaro, G., Holliday, G.L., Thornton, J.M., 2008. Metal ions in biological catalysis: from enzyme databases to general principles. *JBIC Journal of Biological Inorganic Chemistry*, *13*(8), pp. 1205-1218.

ASM Aerospace, 2015. *Ti technical data sheet.* Available at: http://www.aerospacemetals.com/ [Accessed May, 2015].

Assael, M.J., Kalyva, A.E., Antoniadis, K.E., Banish, R.M., Egry, I., Quested, P.N., Wu, J., Kaschnitz, E.; Wakeham W.A., 2010. Reference data for the density and viscosity of liquid copper and liquid tin. *Journal of Physical and Chemical Reference Data*, 39, pp. 033105:1-9.

ASTM F1108-14. *Standard Specification for Titanium-6Aluminum-4Vanadium Alloy Castings for Surgical Implants (UNS R56406)*. ASTM International, West Conshohocken, PA, 2014

ASTM F136-13. *Standard Specification for Wrought Titanium-6Aluminum-4Vanadium ELI (Extra Low Interstitial) Alloy for Surgical Implant Applications* (UNS R56401). ASTM International, West Conshohocken, PA, 2013.

ASTM F1472-08. *Standard Specification for Wrought Titanium-6Aluminum-4Vanadium Alloy for Surgical Implant Applications* (UNS R56400). ASTM International, West Conshohocken, PA, 2008.

ASTM F2792-12a. *Standard Terminology for Additive Manufacturing Technologies*, (Withdrawn 2015), ASTM International, West Conshohocken, PA, 2012, pp. 10-12.

ASTM F2924-14. *Standard Specification for Additive Manufacturing Titanium-6 Aluminum-4 Vanadium with Powder Bed Fusion*. ASTM International, West Conshohocken, PA, 2014.

ASTM F3001-14. *Standard Specification for Additive Manufacturing Titanium-6 Aluminum-4 Vanadium ELI (Extra Low Interstitial) with Powder Bed Fusion*. ASTM International, West Conshohocken, PA, 2014

ASTM F620-11. *Standard Specification for Titanium Alloy Forgings for Surgical Implants in the Alpha Plus Beta Condition*. ASTM International, West Conshohocken, PA, 2011.ISO 20160:2006. Implants for surgery. Metallic materials – Classification of microstructures for alpha+beta titanium alloy bars.

Bahmani-Oskooee, M., Hossein Nedjad, S., Samadi A., Kozeschnik, E., 2017. Cu-bearing, martensitic stainless steels for applications in biological environments. *Materials & Design*, 130, pp. 442–451.

Becker, T.H., Beck, M., Scheffer, C., 2015. Microstructure and mechanical properties of direct metal laser sintered Ti-6Al-4V. *South African Journal of Industrial Engineering*, 26(1), pp. 1-10.

Bergmann, C., Stumpf, A., 2013. D*ental Ceramics. Microstructure, Properties and Degradation*, Springer, Berlin, Heidelberg, 83 p.

Bertol, L.S., Kindlein, J.W., da Silva, F.P., Aumund-Kopp, C., 2010. Medical design: Direct metal laser sintering of Ti–6Al–4V, *Materials & Design*, 31 (8), pp. 3982–3988.

Bhadeshia, H. K. D. H., 2017. *Metallurgy of Titanium and its Alloys*. http://www.phase-trans.msm.cam.ac.uk/2004/titanium/titanium.html

Campoccia, D., Montanaro, L., Arciola, C.R., 2006. The significance of infection related to orthopedic devices and issues of antibiotic resistance. *Biomaterials*, 27 (11), pp. 2331-2339.

Casalino, G., Campanelli, S.L., Contuzzi, N., Ludovico, A.D., 2015. Experimental investigation and statistical optimization of the selective laser melting process of a maraging steel. *Optics & Laser Technology*, 65, pp. 151–158.

Chai, H.W., Guo, L., Wang, X.T., Fu, Y.P., Guan, J.L., Tan, L.L., 2011. Antibacterial effect of 317L stainless steel contained copper in prevention of implant-related infection in vitro and in vivo. Jo*urnal of Materials Science: Materials in Medicine*, 22, pp. 2525–2535.

ConceptLaser, 2018.Concept Laser. (Online) Available from: http://www.concept-laser.de/en/technology.html (Accessed February 3, 2018).

Courtois, M., 2014. A complete model of keyhole and melt pool dynamics to analyze instabilities and collapse during laser welding. *Journal of Laser Applications*. 26 (4), pp. 04200-9.

Darouiche, R. O., 2004. Treatment of Infections Associated with Surgical Implants. *New England Journal of Medicine*, 350, pp.1422-1429.

Davis, J.R., 2001. *Alloying: Understanding the Basics*, ASM International, 350 p.

DebRoy, T., Wei, H.L., Zuback, J.S., Mukherjee, T., Elmer, J.W., Milewski, J.O., Beese, A.M., Wilson-Heid, A., Ded A., Zhang, W., 2018. Additive manufacturing of metallic components – Process, structure and properties. *Progress in Materials Science*, 92, pp. 112-224.

Digilov, R.M., 2003. Prediction of surface properties of metals from the law of corresponding states. *Journal of Crystal Growth*, 249(1), pp.363-371.

Donachie Jr, M.J., 2000. *Titanium: A Technical Guide*, 2nd Edition. ASM International, 368 p.

du Plessis, A. and le Roux, S.G., 2018. Standardized X-ray tomography testing of additively manufactured parts: a round robin test. *Additive Manufacturing*, 24, pp. 125-136.

du Plessis, A. Yadroitsev, I. Yadroitsava, I. Le Roux, S.G., 2018a. X-Ray Microcomputed Tomography in Additive Manufacturing: A Review of the Current Technology and Applications, 3D Print. *Additive Manufacturing*, 5, 3dp.2018.0060. doi:10.1089/3dp.2018.0060.

du Plessis, A., le Roux, S.G. Guelpa, A., 2016. The CT Scanner Facility at Stellenbosch University: An open access X-ray computed tomography laboratory. *Section B of Nuclear Instruments and Methods in Physics Research, Section B*. 384, pp. 42–49.

du Plessis, A., Sperling, P., Beerlink, A., Kruger, O., Tshabalala, L., Hoosain, S., Mathe, N., le Roux, S.G., 2018b. Standard method for microCT-based additive manufacturing quality control 1: Porosity analysis. *MethodsX* 5, pp. 1102–1110.

Dumbleton, J.H., 1977. Elements of hip joint prosthesis reliability. *Journal of Medical Engineering & Technology*, 1, pp. 341–346.

Dzogbewu, T., 2017. *Direct metal laser sintering of titanium alloys for biomedical applications, DEng thesis*, Central University of Technology, Free State, SA, 197 p.

Eagar, T. W., Tsai, N. S., 1983. Temperature fields produced by traveling distributed heat sources. *Welding Journ*al, 62(12), pp. 346-355.

Elmer, J.W., Palmer, T.A., Babu, S.S. and Specht, E.D., 2005. *In situ* observations of lattice expansion and transformation rates of α and β phases in Ti–6Al–4V. *Materials Science and Engineering: A*, 391(1), pp. 104-113.

Els., J. *Optimal process parameters for the direct metal laser sintering process of Ti64 for the production of medical implants.* MTech. Thesis, Central University of Technology, Free State, Bloemfontein, 2014.

Erinosho, M. F., Akinlabi, E.T., Pityana, S., Owolabi, G., 2017. Laser surface modification of Ti6Al4V-Cu for improved microhardness and wear resistance properties. *Materials Research*, 20(4), pp. 1143-1152.

Everhart, J.L., 1975. *Copper and copper alloy powder metallurgy: Properties and applications. Metal Powder Industries Federation*. Available at: www.copper.org, [Accessed May, 2015].

Facchini, L., Magalini, E., Robotti, P., Molinari, A., Hoges, S. and Wissenbach, K., 2010. Ductility of a Ti-6Al-4V alloy produced by selective laser melting of prealloyed powders. *Rapid Prototyping Journal*, 16(6), pp. 450–459.

Fernandes, D.J., Elias, C.N., Valiev, R.Z., 2015. Properties and Performance of Ultrafine Grained Titanium for Biomedical Applications, *Materials Research*, 18(6), pp. 1163-1175.

Frey, M., Shellabear, M., Thorsson, L., 2009. Mechanical testing of DMLS parts. *EOS whitepaper*, EOS GmbH, Munich.

Gad, G.F.M., Aziz, A.A.A., AlyIbrahem, R., 2012. In-vitro adhesion of Staphylococcus spp. to certain orthopedic biomaterials and expression of adhesion genes. *Journal of Applied Pharmaceutical Science*, 2(6), p.145.

Gepreel, A.-H., Niinomi, M., 2013 Biocompatibility of Ti-alloys for long-term implantation. *Journal of the Mechanical Behavior of Biomedical Materials*, 20, pp. 407-415.

Guo, S., Lu, Y., Wu, S., Liu, L., He, M., Zhao, C., Gan, Y., Lin, J., Luo, J., Xu, X., Lin, J., 2017. Preliminary study on the corrosion resistance, antibacterial activity and cytotoxicity of selective-laser-melted Ti6Al4V-xCu alloys. *Materials Science and Engineering: C*, 72, pp. 631-640.

Habijan, T., Haberland, C., Meier, H., Frenzel, J., Wittsiepe, J., Wuwer, C., Greulich, C., Schildhauer, T.A., Köller, M., 2013. The biocompatibility of dense and porous Nickel-Titanium produced by selective laser melting. *Materials Science and Engineering*, 33(1), pp. 419–426.

Imam, M.A. and Fraker, A.C., 1996. Titanium alloys as implant materials. In *Medical applications of titanium and its alloys: The material and biological issues*. ASTM International.

Javaid, M., Haleem, A., 2017. Additive manufacturing applications in medical cases: A literature based review. *Alexandria Journal of Medicine*, https://doi.org/10.1016/j.ajme.2017.09.003

Khairallah, S.A., Anderson, A.T., Rubenchik, A., King, W.E., 2016. Laser powder-bed fusion additive manufacturing: Physics of complex melt flow and formation mechanisms of pores, spatter, and denudation zones. *Acta Materialia*, 108, pp. 36-45.

Kinnear, A. Dzogbewu, T. C., Krakhmalev, P. Yadroitsava I., Yadroitsev, I., 2017. Manufacturing, microstructure and mechanical properties of selective laser melted Ti6Al4V-Cu. *In: Lasers in Manufacturing Conference*, Munich, June 26-29, 2017.

Kinnear, A., 2016. *Direct metal laser sintering of multiple material structures for biomedical applications*. Master thesis, Central University of Technology, Free State, Bloemfontein, March 2016, 106 p.

Kinnear, A., Dzogbewu, T. C., Yadroitsava, I., Yadroitsev I., 2016. *In-situ* alloying process of Ti6Al4V-xCu structures by direct metal laser sintering. *17th International conference RAPDASA*, 2-4 November 2016, Vaal University of Technology Vanderbijlpark, South Africa.

Krakhmalev, P., Fredriksson, G., Yadroitsava I., Kazantseva N., du Plessis, A., Yadroitsev, I., 2016. Deformation behavior and microstructure of Ti6Al4V manufactured by SLM. *Physics Procedia*, 83, pp. 778 – 788.

Krakhmalev, P., Yadroitsev, I., Yadroitsava, I., de Schmidt, O., 2017. Functionalization of biomedical Ti6Al4V via *in situ* alloying by Cu during Laser Powder Bed Fusion manufacturing. *Materials*, 10, pp. 1154-1169.

Kurtz, S.M., Lau, E., Ong, K., Zhao, K., Kelly, M., Bozic, K.J., 2009. Future young patient demand for primary and revision joint replacement: National projections from 2010 to 2030. *Clinical orthopaedics and related research*, 467, pp. 2606–2612.

Leyens, Ch. and Peters, M., 2003. *Titanium and Titanium Alloys: Fundamentals and Applications*, Wiley-VCH, 532 p.

Li M., Ma Z., Zhu Y., Xia H., Yao M., Chu X., Wang X., Yang K., Yang M., Zhang Y., Mao C., 2016. Towards a molecular understanding of the antibacterial mechanism of Copper-bearing Titanium alloys against Staphylococcus aureus. *Advanced Healthcare Materials*, 5(5), pp. 557–566.

Li, M., Nan, L., Xu, D., Ren, G., Yang, K., 2015. Antibacterial performance of a Cu-bearing stainless steel against microorganisms in tap water. *Journal of Materials Science & Technology*, 31, pp. 243-251.

Liu, J., Li F., Liu, C., Wang H., Ren, B., Yang K., Zhang E., 2014. Effect of Cu content on the antibacterial activity of titanium–copper sintered alloys, *Materials Science and Engineering. C.*, 35, pp. 392–400.

Liu, R., Memarzadeh, K., Chang, B., Zhang, Y., Ma, Z., Allaker, R.P., Ren, L., YangR., 2016. Antibacterial effect of copper-bearing titanium alloy (Ti-Cu) against Streptococcus mutans and Porphyromonas gingivalis. *Scientific Reports*, 6, pp. 29985.

Lodererova, M., Rybnicek, J., Steidl, J., Richter, J., Boivie, K., Karlsen, R., Åsebø, O., 2009. Biocompatibility of metal sintered materials in dependence on multi-material graded structure. *Proc. 13th International Conference on Biomedical Engineering*, Heidelberg, Berlin.

Lütjering, G. and Williams, J.C., 2017. *Titanium*, Berlin Heidelberg. Berlin, 442 p.

Lutter-Günther, M., Bröker, M., Mayer, T., Lizak, S., Seidel, C., Reinhart, G., 2018. Spatter formation during laser beam melting of AlSi10Mg and effects on powder quality. *Procedia CIRP*, 74, pp. 33-38.

Ma, Z., Ren, L., Liu, R., Yang, K., Zhang, Y., Liao, Z., Liu, W., Qi, M. Misra, R.D.K., 2015. Effect of heat treatment on Cu distribution, antibacterial performance and cytotoxicity of Ti–6Al–4V–5Cu Alloy. *Journal of Materials Science & Technology*, 31 (7), pp. 723–732.

Ma, Z., Ren, L., Shahzad, M.B., Liu, R., Zhao, Y., Yang, K., 2018. Hot deformation behavior of Cu-bearing antibacterial titanium alloy. *Journal of Materials Science & Technology*, https://doi.org/10.1016/j.jmst.2017.12.015.

Makoana N.V., Yadroitsava I., Möller H. and Yadroitsev I., 2018. Characterisation of 17-4PH single tracks produced at different parametric conditions towards increased productivity of LPBF Systems—The effect of laser power and spot size upscaling. *Metals*, 8(7), pp. 475.

Manfredi, D., Calignano, F., Krishnan, M., Canali, R., Ambrosio, E.P., Biamino, S., Ugues, D., Pavese, M. and Fino, P., 2014. Additive manufacturing of al alloys and aluminium matrix composites (AMCs). *Light Metal Alloys Applications*, 11, pp. 3-34.

Matthews M. J., Guss, G., Khairallah, S. A., Rubenchik, A. M., Depond, P. J., King, W. E., 2016. Denudation of metal powder layers in laser powder bed fusion, processes. *Acta Materialia*, 114, pp. 33–42.

Matweb, 2017. www.matweb.com. *Database of material properties.*

Meier, H., Haberland, C., 2008. Experimental studies on selective laser melting of metallic parts. *Materials Science and Engineering Technology. Werkstofftech*., 39, pp. 665–670.

Mercelis, P., Kruth, J.-P., 2006. Residual stresses in selective laser sintering and selective laser melting. *Rapid Prototyping Journal*, 12 (5), pp. 254 – 265.

Mertens, A., Reginster, S., Paydas, H., Contrepois, Q., Dormal, T., Lemaire, O., Lecomte-Beckers, J., 2014. Mechanical properties of alloy Ti–6Al–4V and of stainless steel 316L processed by selective laser melting: Influence of out-of-equilibrium microstructures. *Powder Metallurgy*, 57(3), pp. 184-189.

Moletsane, M. G., Krakhmalev, P., Kazantseva, N., du Plessis, A., Yadroitsava, I., Yadroitsev, I., 2016. Tensile properties and microstructure of direct metal laser-sintered Ti6Al4V (ELI) alloy. *The South African Journal of Industrial Engineering*, 27 (3), pp. 110-121.

Montanaro L, Testoni F, Poggi A, Visai L, Speziale P, Arciola CR., 2011. Emerging pathogenetic mechanisms of the implant-related osteomyelitis by Staphylococcus aureus. *The International Journal of Artificial Organs*, 34 (9), pp. 781-788.

Murr, L.E. *et al*., 2009. Microstructure and mechanical behaviour of Ti–6Al–4V produced by rapid-layer manufacturing, for biomedical applications. *Journal of the Mechanical Behavior of Biomedical Materials*, 2, pp 20–32.

National Institutes of Health Consensus Development Conference Statement, Clinical Applications of Biomaterials, 1982. *National Institutes of Health Consensus Development Conference Statement*, 1-3; 4(5), pp. 1-19.

Niinomi, M., 2003. Recent research and development in titanium alloys for biomedical applications and healthcare goods. *Science and Technology of Advanced Materials*, 4 (5), pp. 445-454.

Paradis, P.-F.; Ishikawa, T.; Yoda, S., 2002. Non-contact measurements of surface tension and viscosity of Niobium, Zirconium, and Titanium using an electrostatic levitation furnace. *International Journal of Thermophysics*, 23(3), pp. 825–842.

Qiu, C., Panwisawas, P. Ward, M., Basoalto, H.C., Brooks, J.W. Attallah, M.M., 2015. On the role of melt flow into the surface structure and porosity development during selective laser melting, *Acta Materialia*, 96, pp. 72-79

Rafi, H., Karthik, N.V., Gong, H., Starr, T.L. and Stucker, B.E., 2013. Microstructures and mechanical properties of Ti6Al4V parts fabricated by selective laser melting and electron beam melting. *Journal of Materials Engineering and Performance*, 22(12), pp. 3872–3883.

Realizer, 2018. http://www.realizer.com

Ren, L., Memarzadeh, K., Zhang, S., Sun, Z., Yang, C., Ren, G. Allaker, R.P. Yang, K., 2016. A novel coping metal material CoCrCu alloy fabricated by selective laser melting with antimicrobial and antibiofilm properties. *Materials Science and Engineering C*, 67, pp. 461–467.

Ren, L., Nan, L., Yang, K., 2011. Study of copper precipitation behavior in a Cu-bearing austenitic antibacterial stainless steel. *Materials & Design*, 32, pp. 2374–2379.

Ren, L., Yang, K., 2017. Antibacterial design for metal implants. In: *Metallic Foam Bone Processing, Modification and Characterisation and Properties*. Eds. T. Matsushita, S. Fujibayashi, T. Kokubo, Elsevier, pp. 203–216.

Renishow, 2018. http://www.renishaw.com/en/metal-additive-manufacturing-3d-printing--15240

Ridge, P.G., Zhang, Y. and Gladyshev, V.N., 2008. Comparative genomic analyses of copper transporters and cuproproteomes reveal evolutionary dynamics of copper utilization and its link to oxygen. *PLoS One*, *3*(1), p. e1378.

Shifeng, W., Shuai, L., Qingsong, W., Yan, C., Sheng, Z., Yusheng, S., 2014. Effect of molten pool boundaries on the mechanical properties of selective laser melting parts. *Journal of Materials Processing Technology*, 214(11), pp.2660-2667.

Sistiaga, M.L.M., Mertens, R., Vrancken, B., Wang, X., Van Hooreweder, B., Kruth, J.-P., Van Humbeeck, J., 2016. Changing the alloy composition of Al7075 for better processability by selective laser melting, *Journal of Materials Processing Technology*, 238, pp. 437-445.

Sun, J., Yang, Y., Wang, D., 2013. Parametric optimization of selective laser melting for forming Ti6Al4V samples by Taguchi method. *Optics & Laser Technology*, 49, pp. 118–24.

Taylor, B., Weidmann, E., 2016. *Metallographic preparation of titanium*. Application notes. http://www.struers.com.

The University of Texas, 2017. Accessed from http://www.me.utexas.edu 12/5/2017

Thijs, L., Kempen, K., Kruth, J.P., Van Humbeeck, J., 2013. Fine-structured aluminium products with controllable texture by selective laser melting of pre-alloyed AlSi10Mg powder. *Acta Materialia*, 61(5), pp. 1809-1819.

Tolochko, N.K., Mozzharov, S.E., Yadroitsev, I.A., Laoui, T., Froyen, L., Titov, V.I., Ignatiev, M.B., 2004. Balling processes during selective laser treatment of powders. *Rapid Prototyping Journal*, 10 (2), pp. 78–87.

Tsai, D.M. Caterson, E.J., 2014. Current preventive measures for health-care associated surgical site infections: a review. *Patient Safety in Surgery*, 8, p. 42

Tucho, M., *et al*., 2018. Investigation of effects of process parameters on microstructure and hardness of SLM manufactured SS316L. *Journal of Alloys and Compounds*, 740, pp. 910-925.

Van Zyl I., Yadroitsava I., Yadroitsev I., 2016. Residual stress in Ti6Al4V objects produced by direct metal laser sintering. *The South African Journal of Industrial Engineering*, 27 (4), pp. 134-141.

Vilaro, T., Colin, C., Bartout, J.D., 2011. As-fabricated and heat-treated micro-structures of the Ti-6Al-4V alloy processed by selective laser melting, *Metallurgical and Materials Transactions A*, 42 (10), pp. 3190-3199.

Vora, P., Mumtaz, K., Todd, I., Hopkinson, N., 2015. AlSi12 in-situ alloy formation and residual stress reduction using anchorless selective laser melting. *Additive Manufacturing*, 7, pp. 12-19.

Vrancken, B., Cain, V., Knutsen, R., Van Humbeeck, J., 2014. Residual stress *via* the contour method in compact tension specimens produced via selective laser melting. *Scripta Materialia*, 87, pp. 29–32.

Vrancken, B., Thijs, L., Kruth, J.P., Van Humbeeck, J., 2012. Heat treatment of Ti6Al4V produced by selective laser melting: Microstructure and mechanical properties. *Journal of Alloys and Compounds*, 541, pp. 177–185.

Vrancken, B., Thijs, L., Kruth, J.P., Van Humbeeck, J., 2014a. Microstructure and mechanical properties of a novel β titanium metallic composite by selective laser melting. *Acta Materialia*, 68, pp. 150-158.

Vrancken, B., Wauthle, J., Kruth, J.P., Van Humbeeck, J., 2013. Study of the influence of material properties in selective laser melting. *LayerWise*, NV, pp.131–139.

Wang, D., Yang, Y., Liu, R., Xiao, D., Sun, J., 2013. Study on the designing rules and process ability of porous structure based on selective laser melting (SLM). *Journal of Materials Processing Technology*, 213, pp. 1734–42.

Wang, G., Yang, J., Jiao, X., 2016. Microstructure and mechanical properties of Ti-22Al-25Nb alloy fabricated by elemental powder metallurgy. *Materials Science and Engineering A*, 654, pp. 69-76.

Wang, K., 1996. The use of titanium for medical applications in the USA. *Materials Science and Engineering: A*, 213(1-2), pp. 134-137.

Wang, S., Yang, C., Ren, L., Shen, M., Yang, K., 2014. Study on antibacterial performance of Cu-bearing cobalt-based alloy. *Materials Letters*, 129, pp. 88-90.

Watari, F., Yokoyama, A., Saso, F., Uo, M., Kawasaki, T., 1997. Fabrication and properties of functionally graded dental implant. *Composites Part B: Engineering*, 28(96), pp. 5–11.

Wehmöller, M., Warnke, P.H., Zilian, C., Eufinger, H., 2005. Implant design and production-a new approach by selective laser melting. *Proc. International Congress Series*, 1281, pp. 690–695.

Wohlers, T., 2015. *Wohlers report 2015: 3D Printing and Additive Manufacturing state in the industry*. Wohlers Associates Inc., Fort Collins, 315 p.

Xi, T., Shahzad, M.B., Xu, D., Sun, Z., Zhao, J., Yang, C., Qi, M., Yang, K., 2017. Effect of copper addition on mechanical properties, corrosion resistance and antibacterial property of 316L stainless steel. *Materials Science and Engineering: C*, 71, pp. 1079-1085.

Yadroitsava I., Els J., Booysen G., Yadroitsev I., 2015a. Peculiarities of single track formation from TI6AL4V alloy at different laser power densities by SLM. *The South African Journal of Industrial Engineering*, 26 (3), pp. 86-95.

Yadroitsava I., Grewar S., Hattingh D., Yadroitsev I., 2015b. Residual stress in SLM Ti6Al4V alloy specimens. *Materials Science Forum*, 828-829, pp. 305-310.

Yadroitsev, I., Krakhmalev, P., Yadroitsava, I., 2014. Selective laser melting ofTi6Al4V alloy for biomedical applications: temperature monitoring and microstructural evolution. *Journal of Alloys and Compounds*, 583, pp. 404–9.

Yadroitsev, I., 2009. *Selective laser melting: direct manufacturing of 3D-objectsby selective laser melting of metal powders*. Saarbrucken: LAP Lambert Academic Publishing AG & Co. KG, 307 p.

Yadroitsev, I., Bertrand, P., Smurov, I., 2007. Parametric analysis of the selective laser melting process. *Applied Surface Science*, 253, pp. 8064–8069.

Yadroitsev, I., Gusarov, A., Yadroitsava, I., Smurov, I., 2010. Single track formation in selective laser melting of metal powders. *Journal of Materials Processing Technology*, 210 (12), pp.1624-1631.

Yadroitsev, I., Krakhmalev, P., Yadroitsava, I., 2015. Hierarchical design principles of selective laser melting for high quality metallic objects. *Additive Manufacturing*, 7, pp.45-56.

Yadroitsev, I., Krakhmalev, P., Yadroitsava I., du Plessis, A., 2018. Qualification of Ti6Al4V ELI alloy produced by laser powder bed fusion for biomedical applications. *The Journal of The Minerals, Metals & Materials Society* (TMS), 70 (3), pp. 372–377.

Yang, J., Han, J., Yu, H., Yin, J., Gao, M., Wang, Z., Zeng, X., 2016. Role of molten pool mode on formability, microstructure and mechanical properties of selective laser melted Ti-6Al-4V alloy. *Materials & Design*, 110, pp. 558-570.

Yao, X., Sun, Q. Y., Xiao, L., Sun, J., 2009. Effect of Ti2Cu precipitates on mechanical behavior of Ti–2.5 Cu alloy subjected to different heat treatments. *Journal of Alloys and Compounds*, 484 (1), pp. 196-202.

Yasa, E., Deckers, J., Kruth J-P., 2011. The investigation of the influence of laser remelting on density, surface quality and microstructure of selective laser melting parts. *Rapid Prototyping Journal*, 17, pp.312–27.

Zhao, J., Ren, L., Zhang, B., Cao, Zh., Yang, K., 2017. In vitro study on infectious ureteral encrustation resistance of Cu-bearing stainless steel. *Journal of Materials Science and Technology*, 33, pp. 1604–1609.

Zygo Corp., 2018. *Surface texture parameters.* Accessed from www.zygo.com 1.10.2017.